Spring 5-10-2014

Tri-Octahedral Domains and Crystallinity in Synthetic Clays: Implications for Lacustrine Paleoenvironmental Reconstruction

Rebecca Pickering

TRI-OCTAHEDRAL DOMAINS AND CRYSTALLINITY IN SYNTHETIC CLAYS: IMPLICATIONS FOR LACUSTRINE PALEOENVIRONMENTAL RECONSTRUCTION

by

REBECCA ANN PICKERING

Under the Direction of Dr. Daniel M. Deocampo

ABSTRACT

The proportion of authigenic to detrital clay minerals in terrestrial sediments is variable. It has previously been hypothesized that pure Mg-silicates in regions such as Amboseli Basin in Kenya occur due to the absence of Al-rich detritus. We tested this by replicating two Mg-silicate synthesis experiments while adding Al-rich smectite. The first study produced an X-ray amorphous Mg-silicate gel, with little response to addition of Al-rich smectite. The second experiment shifted the 060 peak associated with clay octahedral sheets, suggesting we synthesized trioctahedral domains in a smectite structure. Peak height increased linearly with more heating, indicating crystallinity changes. These results confirm that Al-rich detritus can influence the mineralogy of authigenic clays in saline, alkaline settings. By examining how clay neoformation is affected by silica saturation, we can better understand how the clays found in Neogene lacustrine environments are formed and the climate and of that time.

INDEX WORDS: Clay synthesis, Sepiolite, Smectite, Octahedral domains, Mg-Silicate, Kenya, Amboseli basin, XRD, XRF, SEM, EDS

TRI-OCTAHEDRAL DOMAINS AND CRYSTALLINITY IN SYNTHETIC CLAYS: IMPLICATIONS FOR LACUSTRINE PALEOENVIRONMENTAL RECONSTRUCTION

by

REBECCA ANN PICKERING

A Thesis Submitted in Partial Fulfillment of the Requirements for the Degree of

Master of Science

in the College of Arts and Sciences

Georgia State University

2014

TRI-OCTAHEDRAL DOMAINS AND CRYSTALLINITY IN SYNTHETIC CLAYS: IMPLICATIONS FOR LACUSTRINE PALEOENVIRONMENTAL RECONSTRUCTION

by

REBECCA ANN PICKERING

Committee Chair: Daniel M. Deocampo

Committee: W. Crawford Elliott

Nadine Kabengi

Electronic Version Approved:

Office of Graduate Studies

College of Arts and Sciences

Georgia State University

May 2014

DEDICATION

To my Family: thank you for putting up with me through this journey over these last few years and always reminding me to keep my goal in sight. I cannot thank you enough for pushing me and being there every time I faced a new challenge. Mom and Dad I truly could not be who I am today without each one of you.

ACKNOWLEDGEMENTS

First I would like to thank all the students, staff and faculty of the Geosciences Department at Georgia State University. I have become close to many of you over the last few years and your conversations and words of encouragement, guidance and never-ending support helped me cross the finish line. Secondly, I would like to acknowledge Georgia State University for providing funding through a teaching assistantship and grant #50759-UR2 from the American Chemical Society Petroleum Research Fund and grant # 1029020 from the National Science Foundation for giving me the opportunity to conduct this research. Next I must thank my extraordinary advisor, Dr. Dan Deocampo for all of his help and guidance along the way. You solved every problem I had, offered new learning experiences and kept me on track. I cannot thank you enough for believing in me and allowing me to pursue so many different things over the last few years. I must also show great appreciation to my committee members, Dr. W. Crawford Elliott and Dr. Nadine Kabengi for their guidance and inspiring conversations.

I must also thank: Ms. Basirat Lawal and Ms. Tia Williams, I truly cannot thank either one of you enough for solving every problem I ever had and always doing it with a smile; Dr. Robert Simmons for showing me the wonders of biological imaging and the SEM; Dr. Jeffery E. Post for his helpful insight; Dr. Christy Vissagi for countless pep talks and encouraging words; Lucy Taylor for being not only a lab mate and friend but the sister I never had; and finally Dr. Laura Zaunbrecher, for keeping me on track and inspiring me to do more.

TABLE OF CONTENTS

LIST OF TABLES

LIST OF FIGURES

LIST OF ABBREVIATIONS

Mg……..……....Magnesium
EDS…….. Energy Dispersive Spectroscopy
g……...……..…Gram
GSU……...……....…Georgia State University
HCl…..…….……..…….....……..…Hydrochloric acid
ICP-OES…….…..... Inductively Coupled Plasma Optical Emission Spectroscopy
L…….……...….……...……..…Liter
M…….……Molarity
$MgCl_2 \cdot 6H_2O$…….....Magnesium Chloride Hexahydrate
Na_4SiO_4…….……..Sodium Orthosilicate
mL…….……....…Milliliter
NaOH…….……..Sodium Hydroxide
Na_2SiO_3 ……..…… Sodium Silicate
NSF……..…....…….……..National Science Foundation
pH……...… Decimal Logarithm of the Reciprocal of the Hydrogen Ion Activity
Si……....Silica
ppm……..……Parts Per Million
PRF……...…….....Petroleum Research Fund
rpm……..…Revolutions per minute
H_2O……...Water
SEM…….……Scanning Electron Microscopy
Sep-sp-1…….. Clay Mineral Society Sepiolite Source Clay
SWy-2……Clay Mineral Society Na-Montmorillonite Source Clay
µm…….……..…Micrometer
wt%.....Weight Percent
Al……..…Aluminum
XRD……...……...…..X-Ray Diffraction
XRF…….…..…....…X-Ray Fluorescence
WD……Wavelength Dispersive
SiO_2……...……..…….……Silicon Dioxide
MgO……. Magnesium Oxide

LIST OF MINERAL CHEMICAL FORMULAS

Chalcedony……..……..SiO_2
Chrysotile…… $Mg_3(Si_2O_5)(OH)_4$
Halite……..……..NaCl
Na-Montmorillonite…….....$Na_{0.33}(Al,Mg)_2(Si_4O_{10})(OH)_2\ nH_2O$
Opal-CT……..……..…$SiO_2 \bullet n(H_2O)$
Quartz.…….SiO_2
Talc…….…….$Mg_3Si_4O_{10}(OH)_2$
Saponite……..…….….. $Ca_{0.25}(Mg,Fe)_3((Si,Al)_4\ O_{10})(OH)_2 \bullet n(H_2O)$
Sepiolite……...…… $Mg_4Si_6O_{15}(OH)_2 \cdot 6H_2O$

LIST OF EQUATIONS

1 INTRODUCTION

Clay minerals have been recognized as one of the most abundant minerals on the surface of the earth (Moore and Reynolds, 1997). Authigenic clays have been acknowledged as important chemical precipitates in both continental and marine sediments. They are a main component from the period of initial deposition through late diagenesis.Over the years, authigenic clays have proven to not only be important in marine sediments, but in lake sediments as well (Jones, 1986). Factors such as aqueous geochemistry and tectonics can affect how clays appear in the deposition record of lacustrine basins (Jones and Deocampo, 2003).

1.1 Background

1.1.1 Clay Minerals (Focusing on Smectite and Sepiolite)

According to Bergaya and Lagaly (2006) there is not one consistent nomenclature for clay and clay materials, and although size is a key feature in identifying clays, there is no overall accepted upper limit. Generally the term "clay" refers to materials, which have a particle size (e.g. spherical diameter) less than 2 μm, but a distinction must be made between the term "clay" and "clay mineral". Clay usually refers to the size fraction of natural materials, and clay minerals can be both natural and synthetic phases within the clay fraction. They are associated with having large cation exchange capacity and the ability to show interlayer swelling with the addition of water. Non-crystalline and X-ray amorphous gel silicates may also be referred to as clay minerals due to past usage of the term (Bergaya and Lagaly, 2006).

As described by Brigatti et al. (2006), clay minerals are categorized depending on how the octahedral and tetrahedral sheets are formed into layers. Each silicon tetrahedron corresponds

to four oxygen atoms, and is linked to other tetrahedra by sharing three corners (Figure 1.1.1.1). This forms an "infinite two-dimensional hexagonal mesh pattern" in the tetrahedral sheet (Brigatti et al., 2006).

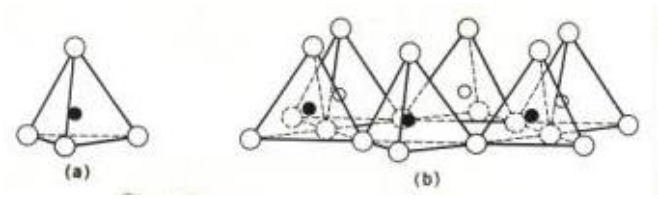

Figure 1.1.1.1: Sketch Showing (a) a single tetrahedron and (b) a tetrahedral sheet.[+]

In each octahedral sheet, connections between neighboring octahedra are formed by sharing edges, as seen in Figure 1.1.1.2, creating "pseudo-hexagonal symmetry" (Brigatti et al., 2006). The free end point (apical Oxygen) of the tetrahedral sheet connects the tetrahedral and octahedral sheets together, forming a common plane.

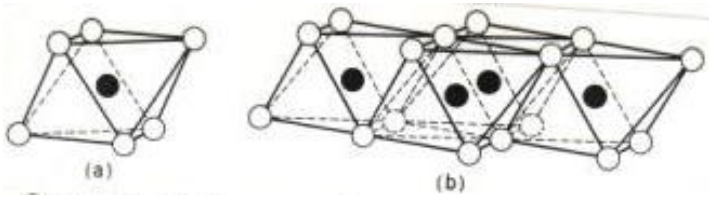

Figure 1.1.1.2: Sketch Showing (a) a single octahedron and (b) an octahedral sheet.[+]

[+] Adapted from: http://ethomas.web.wesleyan.edu/ees123/sheet04.htm

Smectites are expandable 2:1 phyllosilicate minerals; i.e. they are composed of two silica tetrahedral sheets, with an octahedral sheet in the center (Figure 1.1.1.3). The unit cell is composed of eight tetrahedral sites and six octahedral sites.

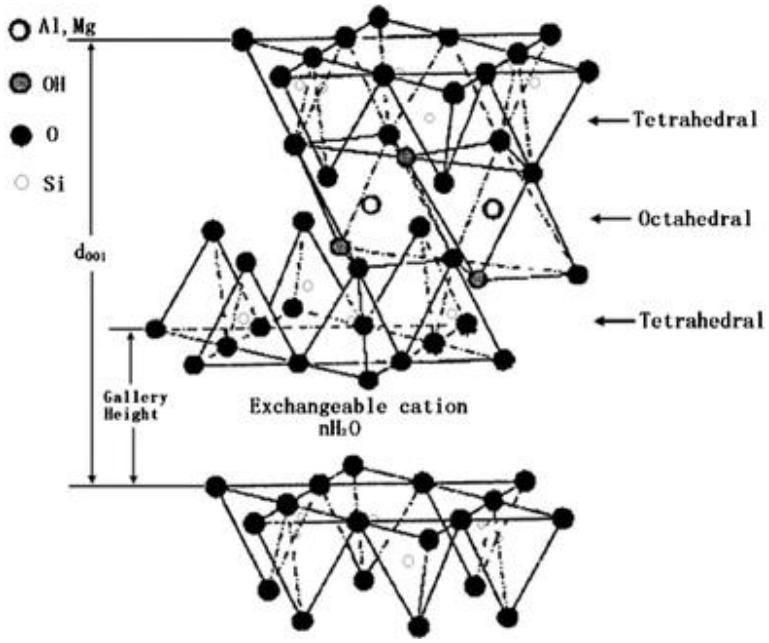

Figure 1.1.1.3: Structure of 2:1 Smectite Clays *

If all six octahedral sites are occupied by three divalent cations (Mg^{+2}) the structure is considered trioctahedral. If only four are occupied by two trivalent cations (Al^{+3}), and no three octahedral cations are sharing an oxygen, it is referred to as dioctahedral (Brigatti et al., 2006). Magnesium can substitute into the octahedral layer, allowing the structure to have the capability to be either dioctahedral or trioctahedral. Although it is not common, under certain conditions some clay minerals may have an intermediate dioctahedral-trioctahedral composition (Deocampo et al., 2009). The layered phyllosilicate structure can be negatively charged due to the substitution of Al^{3+} or Mg^{2+} in the octahedral sites or Al for Si in the tetrahedral sheets. As reported by Brigatti

* http://pubs.rsc.org/en/content/articlelanding/2008/cs/b702653f#!divAbstract

et al. (2006), this variability in layer charge is the most important characteristic of 2:1 clays, because it allows exchangeable cations to occupy the interlayer space between 2:1 groups and balance the charge deficiency created.

This 2:1 structure allows water molecules to occupy the space between the 2:1 layers, expanding the clay when water is absorbed. The removal of water collapses the 2:1 layer spacing. Because of this phenomenon smectite is often referred to as 'swelling clay'. This process is influenced by the hydration of exchangeable cations (Schoonheydt and Johnston, 2006). Water molecules that are joined to exchangeable cations are chemically and physically different from bulk water. Sposito and Prost (1982) revealed that water molecules connected to these cations in the interlayer are strongly polarized and are more attracted to the exchangeable cations than to other water molecules. Schoonheydt and Johnston (2006) describe how adsorption of water occurs due to the movement of cations and leads to the occupancy of remaining interlayer space. In the case of dehydration, water molecules sorbed on external surfaces are removed before the strongly bonded water molecules joined to exchangeable cations present in the interlayer spacing.

The most common smectite is montmorillonite, with the following chemical formula: $(Ca,Na)_{0.33}(Al,Mg)_2(Si_4O_{10})(OH)_2\ nH_2O$. Table 1.1.1.1. offers a summary of smectitic characteristics.

Table 1.1.1.1: Characteristics of Smectite (Murray, 2007).

2:1 Layer Clay	High Cation Exchange Capacity
High Surface Area	Fine Particle Size
High Sorptive Capacity	High Viscosity
High Swelling Capacity	High Plasticity
High Layer Charge	Lattice Substitutions

Sepiolite is also a 2:1 layer phyllosilicate mineral. Murray (2007) discusses how the tetrahedral sheets are linked the same, but they are structurally different from smectites and other clay minerals because the octahedral sheets are one-dimensional, and the tetrahedral sheets are separated into ribbons by cycles of inverted rows of tetrahedrons, forming a chain-like morphology (Figure 1.1.1.4). This structure results in parallel channels running throughout the chain. Because of this structural difference, sepiolite contains two different types of water: one connected to the octahedral cations and the second is bonded in the channels between groups. These channels give the clay mineral a high internal surface area and also provide cation exchange capacity. Some of sepiolite's additional characteristics are summarized in Table 1.1.1.2.

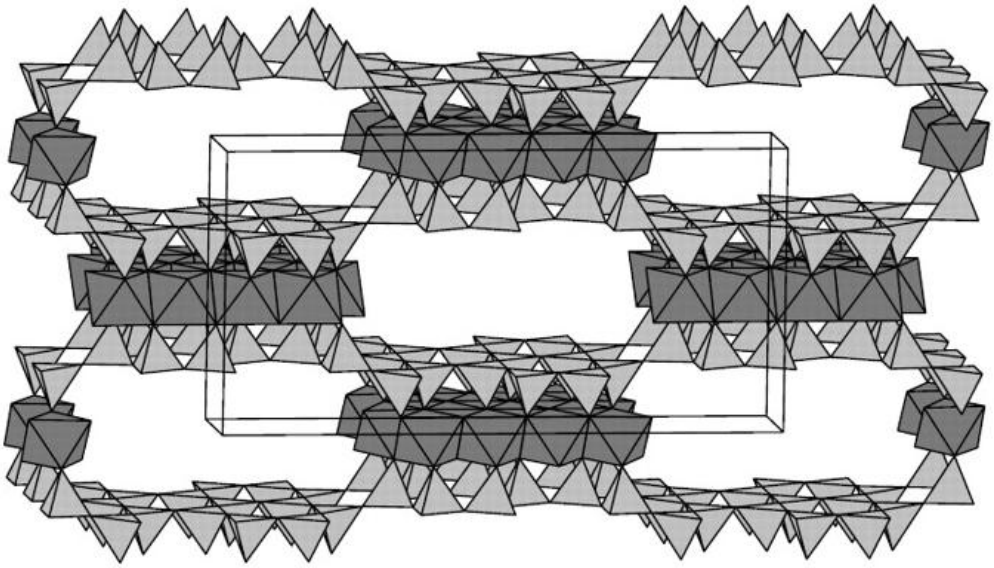

Figure 1.1.1.4: Structure of 2:1 Sepiolite Clay.*

* Adapted from: http://rimg.geoscienceworld.org/content/57/1/69/F13.expansion.html

Table 1.1.1.2: Characteristics of Sepiolite (Murray, 2007).

2:1 Layer Clay	Medium Exchange Capacity
High Surface Area	Moderate Layer Charge
High Sorptive Capacity	High Viscosity
Some Lattice Substitutions	

1.1.2 Detrital vs. Authigenic Clays

Distinguishing between detrital and authigenic clay minerals is often complicated and difficult to achieve (Calvo et al., 1990). Authigenic clays form from solution through direct precipitation, the reaction of amorphous gels, or are transformed from a former mineral (Jones, 1986, and Chamley, 1989). Typically aluminum-rich clays form through hydrolytic weathering of silica-rich minerals and result in detrital clays (Jones and Deocampo, 2003). These clays then react with highly evaporative concentrated fluids, resulting in a neoformation of clay minerals. Several different precipitation systems have arisen, including the growth of interstratified kerolite (Jones, 1986) and Mg-rich layers interlaid in Al-rich substrates (Banfield et al., 1991). These processes are affected by the chemical make-up of the solution in which they are formed in and can easily be altered with the addition or subtraction of a key component, such as detrital silicates (Jones and Deocampo, 2003).

Hay and Stoessel (1984) previously hypothesized the importance of Al-rich detrital substrate in authigenic precipitation. Since then Jones (1986) and Deocampo (2005) have concluded that the absence of Al-rich detritus could be an explanation for the occurrence of pure Mg silicates (Sepiolite) with no Smectite structure present. In situations where there is an absence of magnesium carbonates, magnesium silicates become the primary chemical control in brine evolution; therefore they become important in controlling the chemical composition of the lake wa-

ters (Hardie and Eugster, 1970 and Garrels and Mackenzie, 1967). This increased amount of silicates begins to alter the physical make-up of the authigenic clays.

1.1.3 East African Lacustrine Clay Minerals

In parts of Africa, the East African Rift has formed many Neogene lakes and paleolakes that are either hydrologically closed basins themselves, or through-flow basins upstream of terminal, evaporite lakes (Jones and Deocampo, 2003). Johnson (1996) believes that the extensive Neogene sedimentary records documented in these basins are some of the most important records due to their sensitivities to climate change. The semi-arid climate of the region implies that many of these basins have high evaporation rates and therefore develop some of the most concentrated brines. An example from the area would be the Natron-Magadi Basin, where waters have tested above 300g/kg total dissolved solids at times (Jones et al, 1977).

According to Calvo et al. (1999), saline deposits commonly form in closed continental basins that are located in semi-arid areas, with rift valley settings being the most common areas in which hypersaline conditions develop. The saline rich basins have commonly been associated with magnesium-rich clays as dissolved solids are necessary for the authigenic precipitation of the Mg-rich clay minerals (Jones, 1986). Considerable study of the aqueous geochemistry of the basins has occurred due to their significance in paleoenvironmental reconstructions and potential impacts on local water resources (Jones and Deocampo, 2003). Such high brine concentrations generally lead to higher levels of silica in the water, which in turn alter the geochemistry of the precipitating clays.

1.1.4 Silica Saturation States and Clay Precipitation

Rapid silicate hydrolysis of volcanic glass and lavas provide alkalinity to lacustrine basins and produce high initial SiO_2 and HCO_3^- concentrations (Jones et al, 1977). As the dissolved

solid concentrations increase, the major controls on solutes seem to be the precipitation of biogenic amorphous silica, inorganic calcite, Fe-bearing sulfides, Mg-bearing phyllosilicates, carbonates and oxides (Jones et al, 1977, Hardie and Eugster, 1970, and Jones and Deocampo, 2003). There are many kinetic barriers to authigenic clay mineral precipitation; thermodynamically the importance of silica availability for clay neoformation is the primary determinate of whether smectite or kaolinite precipitates (Jones, 1986). In the case of Deocampo and Ashley's (1999) work, sediments rich in amorphous silica buffered silica concentrations as diagenetic reactions proceeded; this may have contributed to a close association between authigenic smectite and sources of amorphous silica.

1.1.5 Smectite vs. Kaolinite

Kaolinite is the clay mineral that is favored to form in a low silica environment, as it is a layered silicate that can form in most conditions. Under extreme weathering conditions Kaolinite is the contributing detrital substrate, not dioctahedral smectite. In intermediate weathering conditions, dioctahedral smectite is the main detritus. Kaolinite doesn't swell much with fluid as it has a 1:1 structure and is generally considered a non-expandable clay in natural settings. Smectite on the other hand, as previously described, has a large capacity to swell when it comes in contact with fluids. The crystalline structure of smectities allow for a higher surface area and greater absorption of fluids. Deocampo (2010) states that by determining how the clays mineralogy is affected by silica saturation, one can therefore better understand the process in which the clays directly affect the fluids in which they absorb.

Despite all of the previous work surrounding the clay mineralogy of the Neogene paleolakes in Africa, many questions remain regarding clay crystallization mechanisms, neoformation, and diagenesis in these lakes specifically related to silicate levels. This project will address our

poor understanding of the structural changes in crystallinity associated with clay mineral diagenesis.

1.2 Purpose of the Study

Through this research we are looking to answer the following questions:

How will Mg-silica concentrations impact the mineralogy and geochemistry of precipitated clays, and what implications will these impacts have on paleoenvironmental reconstruction?

AND

How will Al-rich detritus affect Mg-silicate precipitation?

By altering Mg-silica concentrations over time in variable conditions we will test the importance of silica availability for clay neoformation and determine how reactions are affected by heating time. By altering the presence of Al-rich detritus we will determine whether a pure Mg-silicate such as sepiolite precipitates, or if a smectite will precipitate.

1.3 Significance and Impacts of Research Findings

Studies of silicates have provided perspectives on the paleoenviroment and climate changes through time (Larsen, 2008). Understanding diagenetic changes in clays is key to reconstructing paleo-humidity. If we wish to apply the geochemistry of lacustrine clays to paleoenvironmental reconstructions, we must first understand the processes that affect the clays (Deocampo, 2005).

By examining how the clay neoformation process is affected by silica saturation, we can better understand how the clays found in the Neogene lacustrine environments were formed and therefore better understand the climate and environment of that time. Much is known about how

clays formed in the past, but if it were shown that silica saturation drastically changes the clays, new processes would need to be taken into consideration.

2 ANALYTICAL METHODOLOGY

2.1 X-ray Diffraction (XRD)

XRD is typically used for the identification of clay minerals. When the wavelength of the radiation emmited is roughly the same as the structural spacings of the clay mineral, diffraction of the beam occurs. Bragg's Law (Bragg, 1913) shows us that when there is constructive interference both the diffraction and subsequent d-spacing of the clay mineral can be determined from the following equation:

$$2d\sin\theta = n\lambda \qquad \text{(Equation 1)}$$

Where:

λ = the wavelength of the rays emitted (Cu Kα = 1.54 Å)

θ = the angle between the incident rays and the surface of the crystal

d = the spacing between layers of atoms (basal layers of the clay)

and constructive interference occurs where n is an interger (typically 1)

Diffraction within a sample's atomic layers is illustrated in Figure 2.1.1

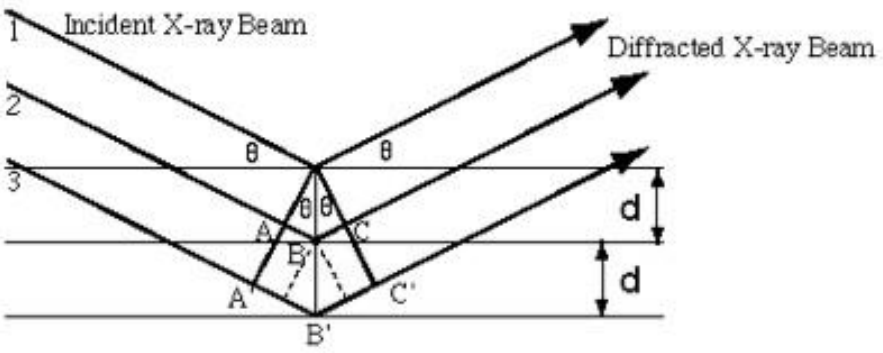

Figure 2.1.1: X-ray diffraction according to Bragg's Law. *

* Adapted from: http://www.geology.wisc.edu/~g203/xray

The principle behind diffraction analysis (per Bragg's law) dictates the 2θ angle position for every peak is based off of interlayer distance. This principle works because each crystalline component phase of a specimen results in its own unique diffraction pattern that arises from the crystal structures of the phases (ICDD).

To generate X-rays, a cathode is heated and electrons are emited across the X-ray tube at 40 kV. From there the electrons hit a copper anode and when they have suffient energy, continuoius characteristic radiation is produced (Moore and Reynolds, 1997). The beam is first passed through soller slits to limit vertical divergence and improve final peak shape. It then passes through several divergence silts to achive simple collimation and control central divergence of the incidence beam, therefore controlling the amount of sample being irradiated. The beam then enters the sample lattice structure and is scattered, creating interference. If the atoms are not evenly spaced within the lattice, i.e not crystalline, constructive interference will not occur and diffraction cannot take place (Moore and Reynolds, 1997). The diffracted beam passes again through several divergence silts and soller slits before it reaches a databox for interprtation and analysis (Figure 2.1.2).

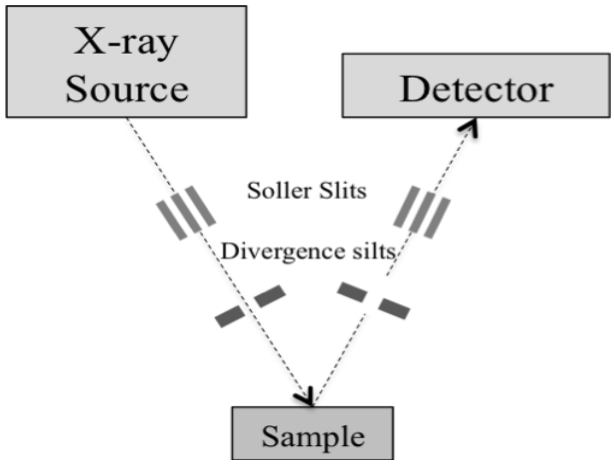

Figure 2.1.2: X-ray Diffraction.

XRD will not only be used to identify the creation of clay minerals but to track crystallinity via changes in peak shape and height.

2.2 X-ray Fluorescence (XRF)

Wavelength Dispersive (WD) X-ray Fluorescence Spectroscopy is the instrumentation used for elemental analysis of a sample (LaTour, 1989). Much like XRD, XRF operates following the principles of Bragg's Law, and the source X-rays cause the sample to emit characteristic radiation. The instrument uses an X-ray tube to directly excite the sample and a crystal diffraction device to diffract X-rays from the sample toward the detector, which measures the fluorescence radiation emitted from the sample (Figure 2.2.1). Collimators are used to limit the spread of X-rays and improve resolution of the system. All of the elements in the sample are excited simultaneously and by placing the detector at a certain angle, the intensity of certain wavelengths can be counted and measured to determine elements in weight percent (wt%). This is completed by a data processing unit, which converts fluorescence into elemental concentrations (Billets, 2006).

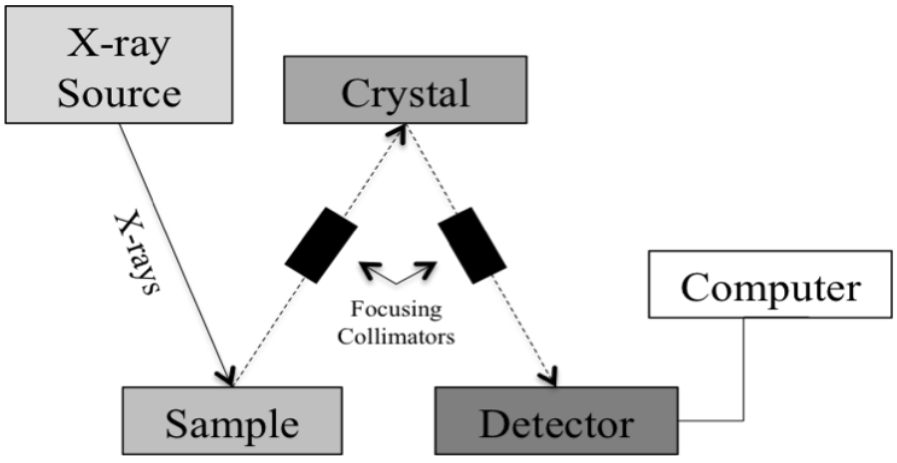

Figure 2.2.1: Wavelength Dispersive X-ray Fluorescence.*

* Adapted from: http://www.slideshare.net/mebecker1/xrf-basic-principles

2.3 Scanning Electron Microscopy (SEM) and Energy Dispersive Spectroscopy (EDS)

SEM is used to produce magnified images of a sample using electrons instead of light. This is useful in investigating clay minerals as it provides the shape and dimensions of the product. SEM functions by showering a sample with primary electrons in a scanning pattern. The electron beam is produced by an electron gun at the top of the microscope, and travels down through a 3-stage condenser lens system, which focuses the beam down toward the sample (Figure 2.3.1).

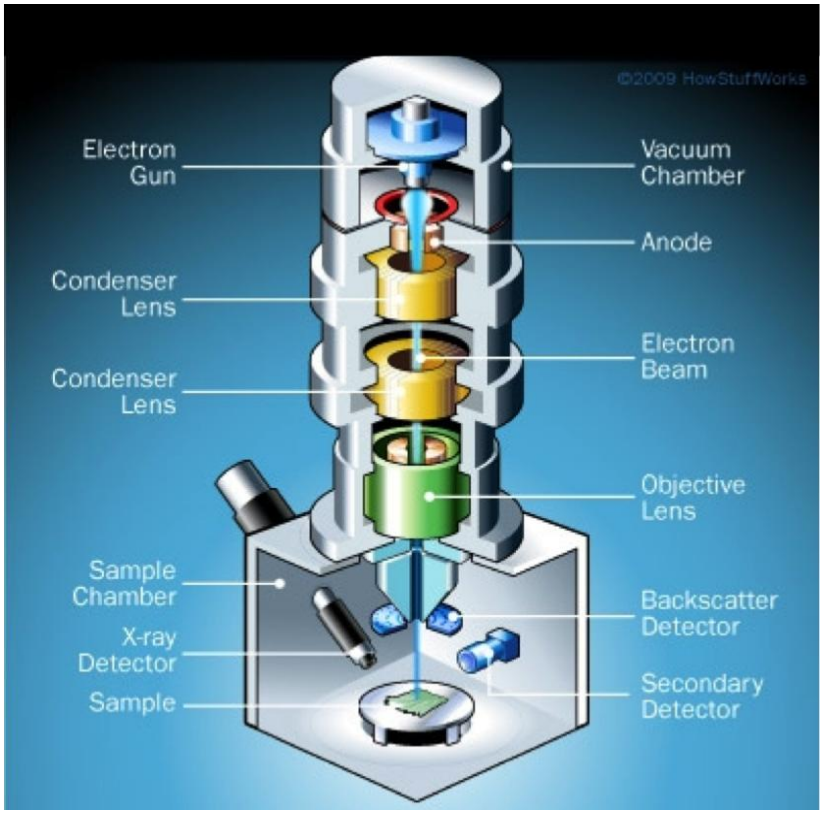

Figure 2.3.1: Scanning Electron Microscopy.*

When the beam hits the sample, both electrons and X-rays are ejected from the sample and collected by detectors. Secondary electrons are generated from the interactions between the electron

* Adapted from: http://science.howstuffworks.com/scanning-electron-microscope2.htm

beam and the atoms in the sample. These inelastic-scattered electrons are collected by a scintillator, which produces photons from electron energy. The photons are then amplified to produce a signal that forms the final image (Bozzola and Russell, 1998).

X-rays are also produced from beam interactions with the atoms in the sample. An EDS detector is used to separate X-rays of different elements into an energy spectrum. The detector contains a silicon crystal that absorbs the X-rays energy by ionization and produces an electrical charge, therefore converting the energy of the X-rays into voltages that correspond to X-rays of individual elements. Software analyzes the produced energy spectrum in order to determine the abundance of specific elements (Bozzola and Russell, 1998).

3 EXPERIMENTAL METHODOLOGY DEVELOPMENT (PART I-PILOT)

According to Carrado et al. (2006), there are limited successful methodologies regarding the laboratory synthesis of sepiolite (Hast, 1956; Siffert and Wey, 1962; Wollast et al., 1968; Abtahi, 1985 and Mizutani et al., 1991). This is because sepiolite is (a) unpredictable in acidic and alkaline solutions at high temperatures (Golden et al., 1985), (b) unstable at hydrothermal conditions (Otsuka et al., 1974) and (c) occupied by smectites that crystallize faster from magnesium silicate gels. This first experiment was a methodological pilot study to determine which methodology would work best for our study. All of the following experiments were conducted in a laboratory facility located in the Department of Geosciences at GSU.

3.1 Magnesium Silicate Super Saturated Solutions Experiment

The Wollast et al. (1968) sepiolite ($Mg_4Si_6O_{15}(OH)_2 \cdot 6H_2O$) synthesis experiment was replicated using synthetic seawater (Table 3.1.1). The seawater was prepared in 2-liter batches (Table 3.1.2) according to Kester et al's (1967) specifications and filtered for solids through a 0.45 µm Millipore filter.

Table 3.1.1: Chemical Composition of Artificial Seawater (Kester et al. 1967).

Salt	**g L^{-1} solution**
Sodium Chloride (NaCl)	23.93g
Sodium Sulfate (Na_2SO_4)	4.01g
Potassium Chloride (KCl)	0.68g
Sodium Bicarbonate ($NaHCO_3$)	0.20g
Magnesium Chloride ($MgCl_2$)	2.53g
Calcium Chloride ($CaCl_2 * 2H_2O$)	3.04g

Seventy-five milliliters of 1000 ppm +/- 1% Fisher Scientific sodium silicate (Na_2SiO_3) solution was buffered to a pH of 9.5 with hydrochloric acid (HCL) and diluted to 500 mL in a volumetric flask. The addition of the buffered Na_2SiO_3 solution to the seawater resulted in the precipitation of a fine white hydrated magnesium silicate powder (Figure 3.1.1). The precipitate was filtered using a 0.22 µm filter and dried for further analysis (Figure 3.1.2). As the first trial only produced 0.1 g of dried product the experiment was replicated four additional times resulting in approximately 0.5 g of product (Figure 3.1.3).

Table 3.1.2: Detailed Make-Up of Synthetic Seawater Batches.

Salt	Batch 1 ($g\ 2L^{-1}$ solution)	Batch 2 ($g\ 2L^{-1}$ solution)	Batch 3 ($g\ 2L^{-1}$ solution)
Sodium Chloride (NaCl)	47.86	47.85	47.86
Sodium Sulfate (Na_2SO_4)	8.02	8.02	8.02
Potassium Chloride (KCl)	1.35	1.36	1.36
Sodium Bicarbonate ($NaHCO_3$)	0.39	0.39	0.39
Magnesium Chloride ($MgCl_2$)	5.07	5.07	5.07
Calcium Chloride ($CaCl_2 * 2H_2O$)	3.04	3.04	3.04

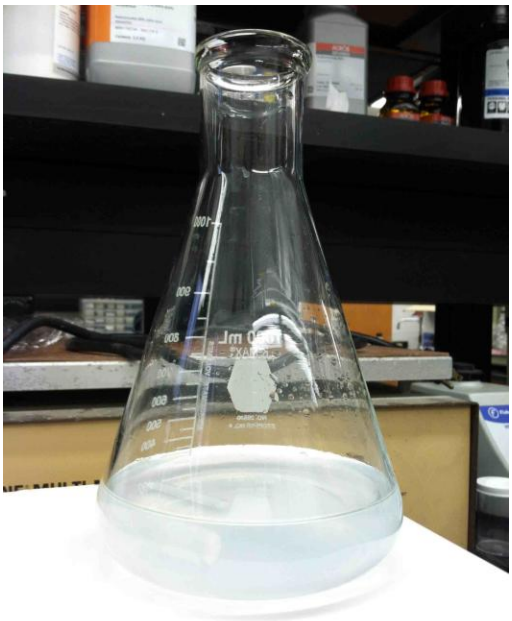

Figure 3.1.1: Initial Formation of the Fine White Precipitate.

Figure 3.1.2: Filtering the Fine White Precipitate Out of Solution.

The experiment was then replicated with the addition of 2 grams of a purified sub-micron Clay Mineral Society Wyoming Na-montmorillonite Source Clay (SWy-2) dispersed in the sea-water. This second reaction produced a thick, viscous cream-colored precipitate (Figure 3.1.4).

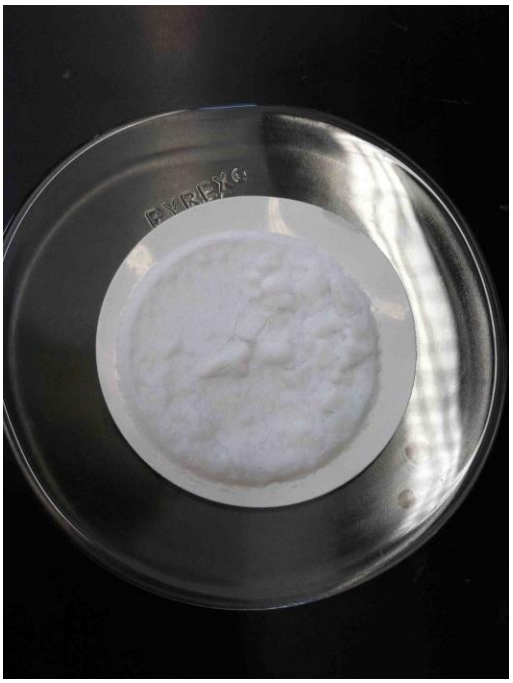

Figure 3.1.3: Final Fine White Powder Produced by the First Reaction (Pre-Clay).

Figure 3.1.4: Thick Precipitate Produced by the addition of SWy-2 (Post-Clay).

3.2 XRF Sample Preparation

Samples were prepared following La Tour's (1989) methodology. Fused discs (Figure 3.2.2) were prepared for analysis to allow for a homogenous distribution of the elements in the sample and a more accurate chemical analysis. To make a fused disc, 0.5 g of sample was mixed with 4.5 g of lithium tetraborate ($Li_2B_4O_7$). This mixture was placed inside a 95% Platinum (Pt), 5% Gold (Au) crucible and heated at 1000° C for 15 minutes in a furnace. At the 10-minute mark, the mixture was swirled to allow for even distribution. After heating, the homogenous mixture was then poured into a preheated mold to form the sample disc (Figure 3.2.1). Sample discs were run for major elemental composition on an automated Rigaku 3270 Wavelength Dispersive X-ray Fluorescence Spectrometer fitted with a Rhodium X-ray tube (Figure 3.2.3). An alpha correction and standard were done prior to running each sample batch.

Figure 3.2.1: Sample Being Poured into Pre-heated Mold.

Figure 3.2.2: Fused Disk

Figure 3.2.3: Rigaku 3270 Wavelength Dispersive XRF.

3.3 XRD Sample Preparation

A sample that is finely ground and has no preferred orientation is crucial for XRD analysis (Jenkins and Snyder, 1996). Therefore, all samples were finely ground before testing and prepared for analysis according to Moore and Reynolds (1997) specifications. Due to small sample size, zero background holders (Figure 3.3.1) were used instead of bulk powder holders. Zero background holders consist of an off-cut single piece of silicon that will not produce background in the pattern, and does not require a specific amount of sample. These holders are crucial for analyzing small amounts of amorphous material (ICDD).

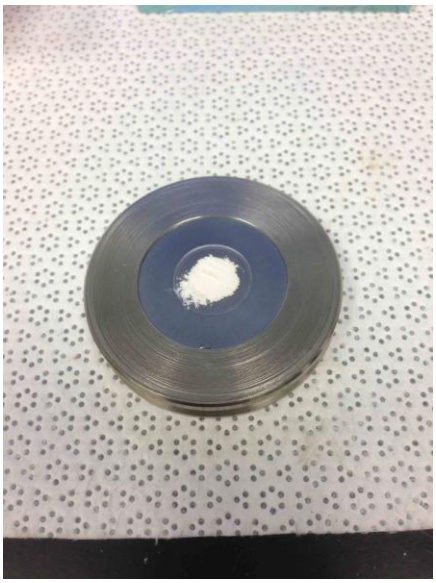

Figure 3.3.1: Zero Background Holder with Powdered Sample.

Both a randomly oriented 5-70 degree (4 hr, 15 min measurement) and 59-62 degree (11 hr, 7 min measurement) were taken on a PANalytical X'pert Pro XRD (Figure 3.3.2) fitted with an Empyrean Copper X-ray tube and a PIXcel 1D detector (Figure 3.3.3). The 060 reflections allow for differentiation between trioctahedral and dioctahedral clays. These peaks are weak and require much longer scan times. Scan specifications are shown in Table 3.3.1. Software programs used were Data Collector, Data Viewer and HighScore Plus.

Figure 3.3.2: PANalytical X'pert Pro XRD

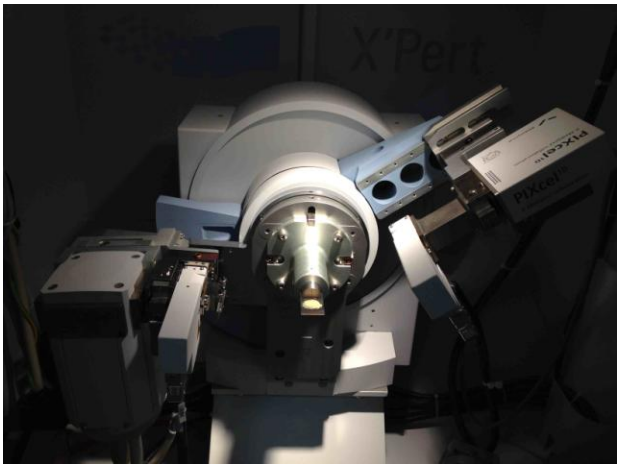

Figure 3.3.3: Close up of XRD sample stage, showing the PIXcel detector on the right.

Table 3.3.1: XRD Scan Specifications.

	5-70 Scan	**060 Scan**
Scan Axis	5.0 – 69.995°	57.997 – 62.999°
Step Size	0.0131°	0.0131°
No of Points	4950	381
Phi	194.0°	291.2°
Voltage	45 kV	45 kV
Current	40 mA	40 mA
Soller Slits	0.04 rad.	0.04 rad.
Fixed Incident Bean Mask	11.6 mm	11.6 mm
Sample Movement	Spinning	Spinning
	2 seconds per rotation	2 seconds per rotation
Scan Time	4 Hrs and 15 Mins	11 Hrs and 7 Mins
Programmable Divergence Slit (PDS)	140 mm to sample 1/8°	140 mm to sample 1/8°
Anti-Scatter Slit	Fixed 1/4°	Fixed 1/4°
Programmable Anti-Scatter Slit (PASS)	Fixed 1/8°	Fixed 1/8°
Beta Filter	Ni	Ni
PIXcel 1D Dectector Active Length	3.347°	3.347°

3.4 SEM and EDS Sample Preparation

To prepare the samples for analysis they were first made electrically conductive by coating them with a thin layer of carbon, a process referred to as sputter coating. The samples are first mounted on sample pegs with a piece of carbon tape and placed in a vacuum chamber (Figure 3.4.1). Oxygen inside the chamber is replaced by argon and an electric field positively charges the argon atoms. The argon ions then knock the carbon atoms loose from the carbon rod, which in turn settle onto the surface of the sample producing a thin even coating (Figure 3.4.2).

Figure 3.4.1: Loading the samples into the sputter coater.

Figure 3.4.2: SEM samples mounted on sample pegs and coated with carbon layer.

All samples were analyzed using a LEO 1450 VP SEM (Figure 3.4.1) with a RonTech Detector and IXRF X-ray system for the pulse processor. SEM accelerating voltage was set to 20 kV. Probe current for EDS was 5 nA with a beam current of 80 mA. Software used for analysis was Zeiss Smart SEM and EDS – IXRF "Iridium".

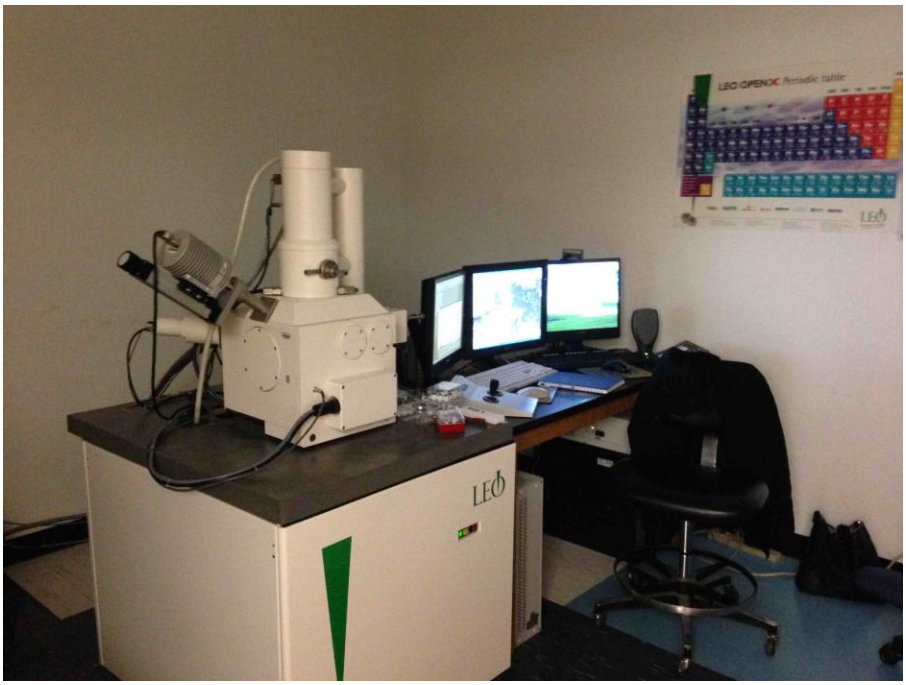

Figure 3.4.3: LEO 1450 VP SEM with a RonTech Detector

4 RESULTS PART I

4.1 XRF

Table 4.1.1: Corrected Major Elemental Composition in Weight Percent (wt%).

Sample	**SiO_2 (wt %)**	**TiO_2 (wt %)**	**Al_2O_3 (wt %)**	**Fe_2O_3 (wt %)**	**MnO (wt %)**	**MgO (wt %)**
Pre-Clay Powder	67.60	0.04	0.39	0.37	0	26.17
SWy-2	65.92	0.14	22.81	4.88	0.01	3.26
Post-Clay Gel	45.08	0.07	13.34	2.92	0	6.92

Sample	**CaO (wt %)**	**Na_2O (wt %)**	**K_2O (wt %)**	**P_2O_5 (wt %)**	**MgO/SiO_2**
Pre-Clay Powder	5.49	0	0.15	0.02	0.57
SWy-2	0.93	1.84	0.18	0.02	0.07
Post-Clay Gel	7.03	23.78	0.81	0.04	0.23

As show in Table 4.1.1, XRF analysis of experimental products revealed that there were both higher levels of Silicon Dioxide (SiO_2) and Magnesium Oxide (MgO) in the Pre-Clay product before SWy-2 was added. Pre-Clay Powder was composed of 67.60 wt % SiO_2 and 26.71 wt % MgO. Post-Clay Gel consisted of 45.08 wt % SiO_2 and 6.92 wt % MgO. Additionally the ratio between MgO and SiO_2 decreased from 0.57 in the Pre-Clay Powder to 0.23 in the Post-Clay Gel due to the addition of SWy-2.

4.2 XRD

Results show some effects of adding Al-rich clay to Mg-silicate synthesis experiments. Pre-Clay Powder produced an X-ray amorphous Mg-silicate, with a broad diffraction hump from ~3.0 – 4.0 Å (Figure 4.2.1), but no discernable 060 peak, which is commonly associated with clay octahedral layers (Figure 4.2.2). The second part of the experiment (Post-Clay Gel) produced a clay mixture with no discernable difference from SWy-2 oriented XRD (Figure 4.2.1) and with a broad 060 peak observed at ~ 1.49-1.50 Å (Figure 4.2.2).

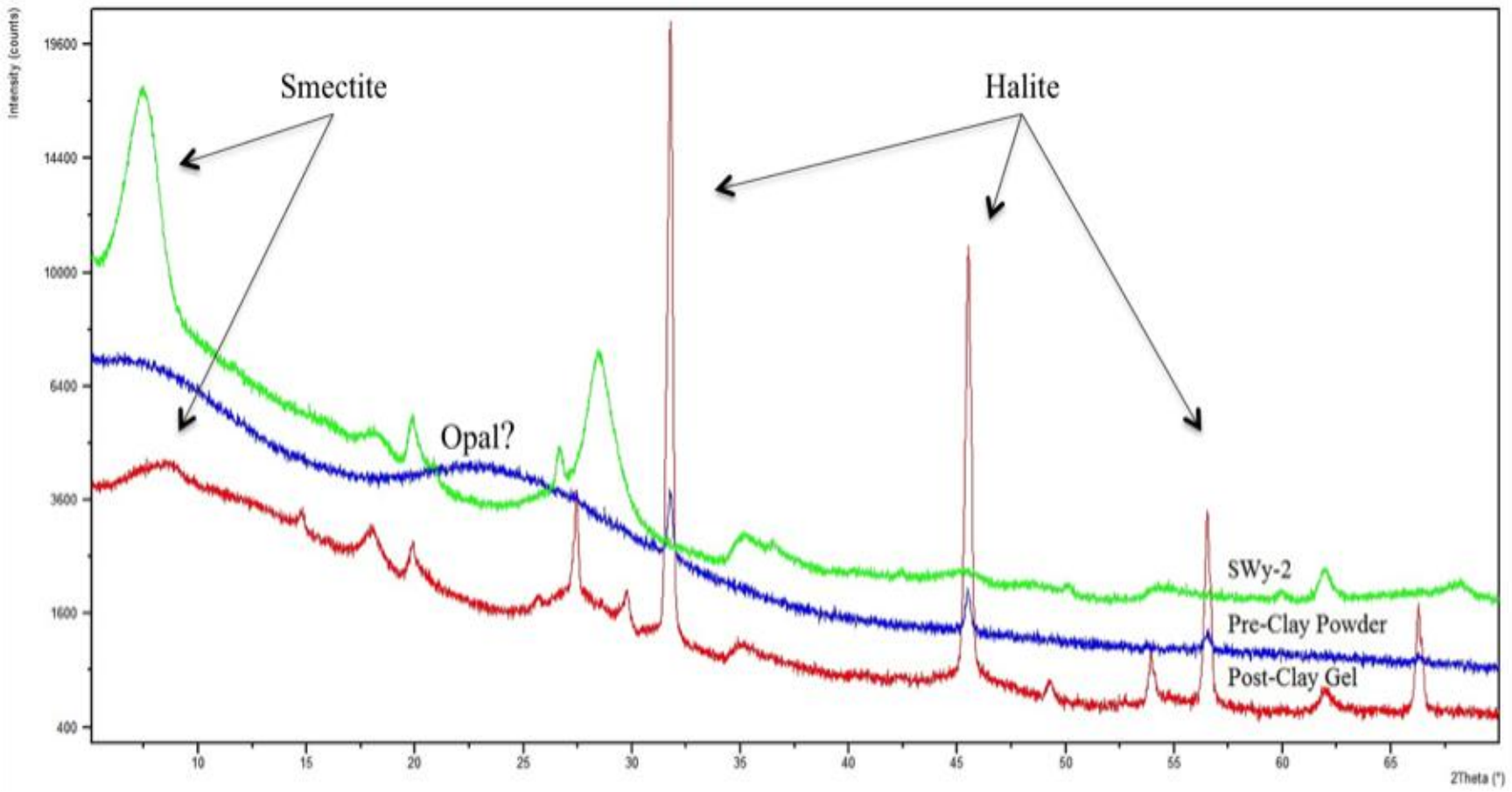

Figure 4.2.1: Diffractogram of SWy-2, Mg-Silicate Precipitate without the Addition of SWy-2 (Pre-Clay Powder) and Mg-Silicate Precipitate with the Addition of SWy-2 (Post-Clay Gel) from 5-70 degrees.

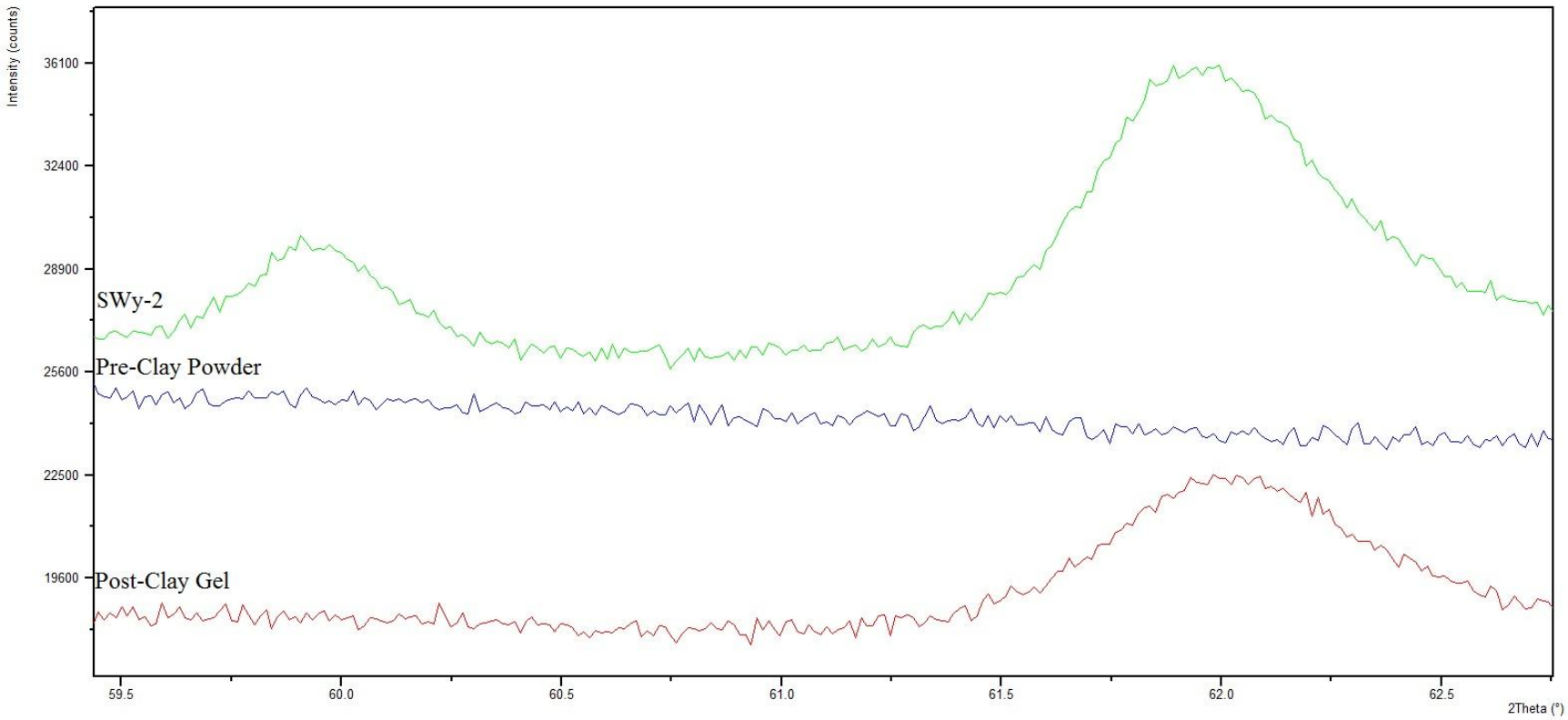

Figure 4.2.2: Diffractogram of SWy-2, Pre-Clay Powder and Post-Clay Gel showing 060 peaks.

4.3 SEM and EDS

SEM images paired with EDS data provide a qualitative way of looking at sample change. Results showed no Mg in either Pre-Clay Powder (Figure 4.3.2) or Post-Clay Gel (Figure 4.3.3) products. Under SEM, smectite is usually wavy and flaky, as seen in Figure 4.3.1, this waviness disappeared in Post-Clay Gel (Figure 4.3.3), partially because of large halite crystals that were identified by EDS. Additionally, Pre-Clay Powder (Figure 4.3.2) looks completely different from SWy-2 (Figure 4.3.1) and Post-Clay Gel (Figure 4.3.3), forming large rectangular smooth blocks.

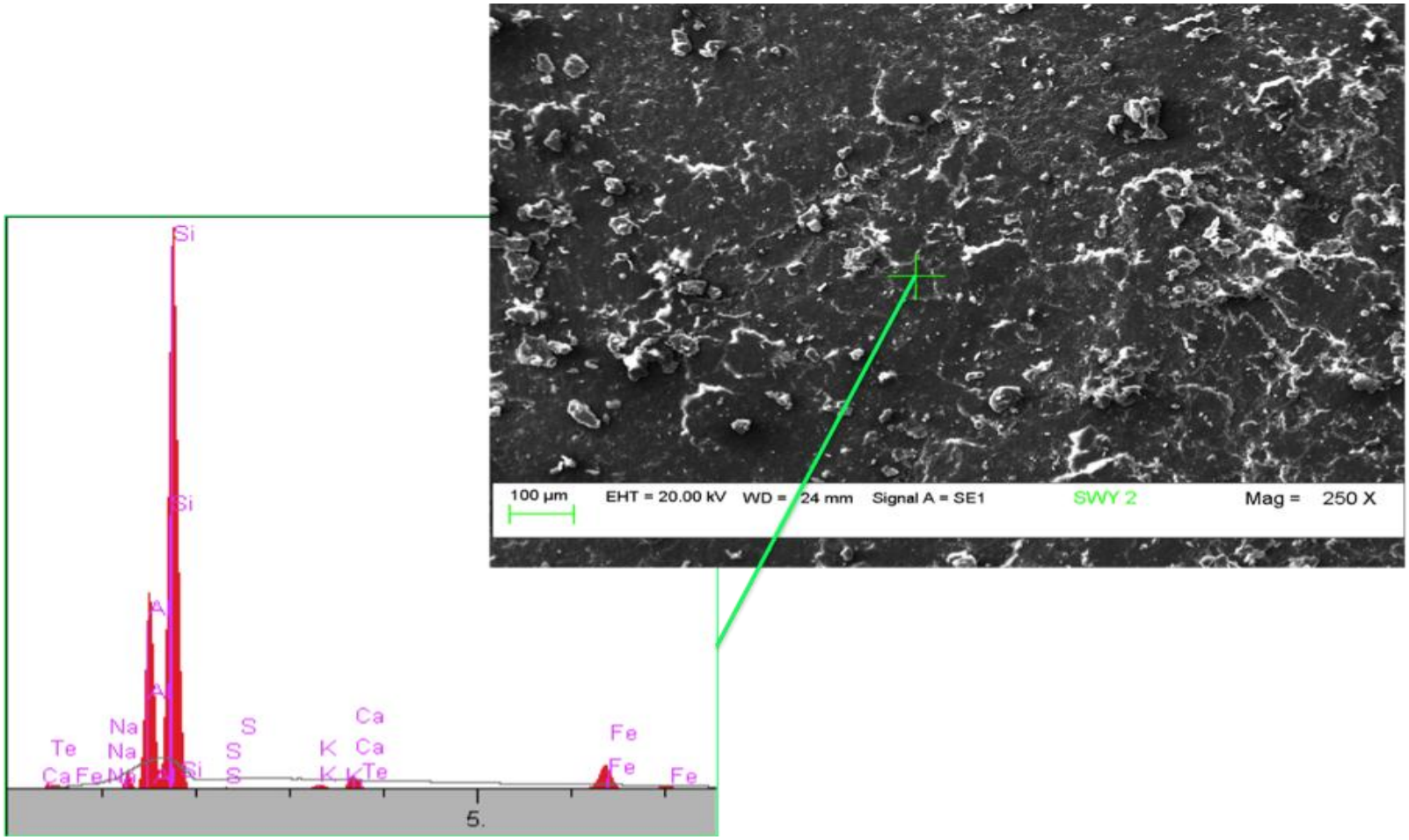

Figure 4.3.1: SEM Image of SWy-2 with Corresponding EDS Results.

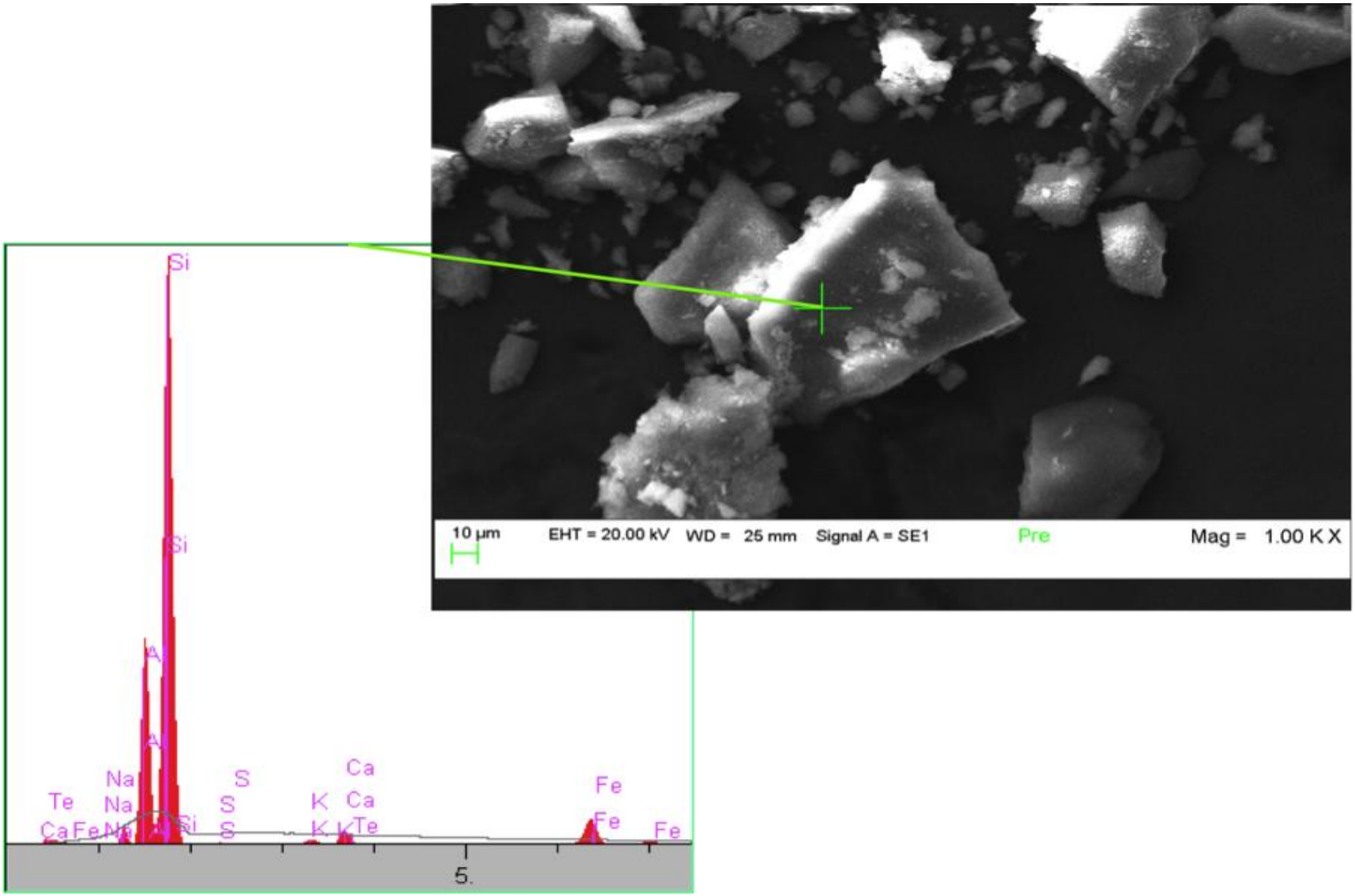

Figure 4.3.2: SEM Image of Pre-Clay Powder with Corresponding EDS Results.

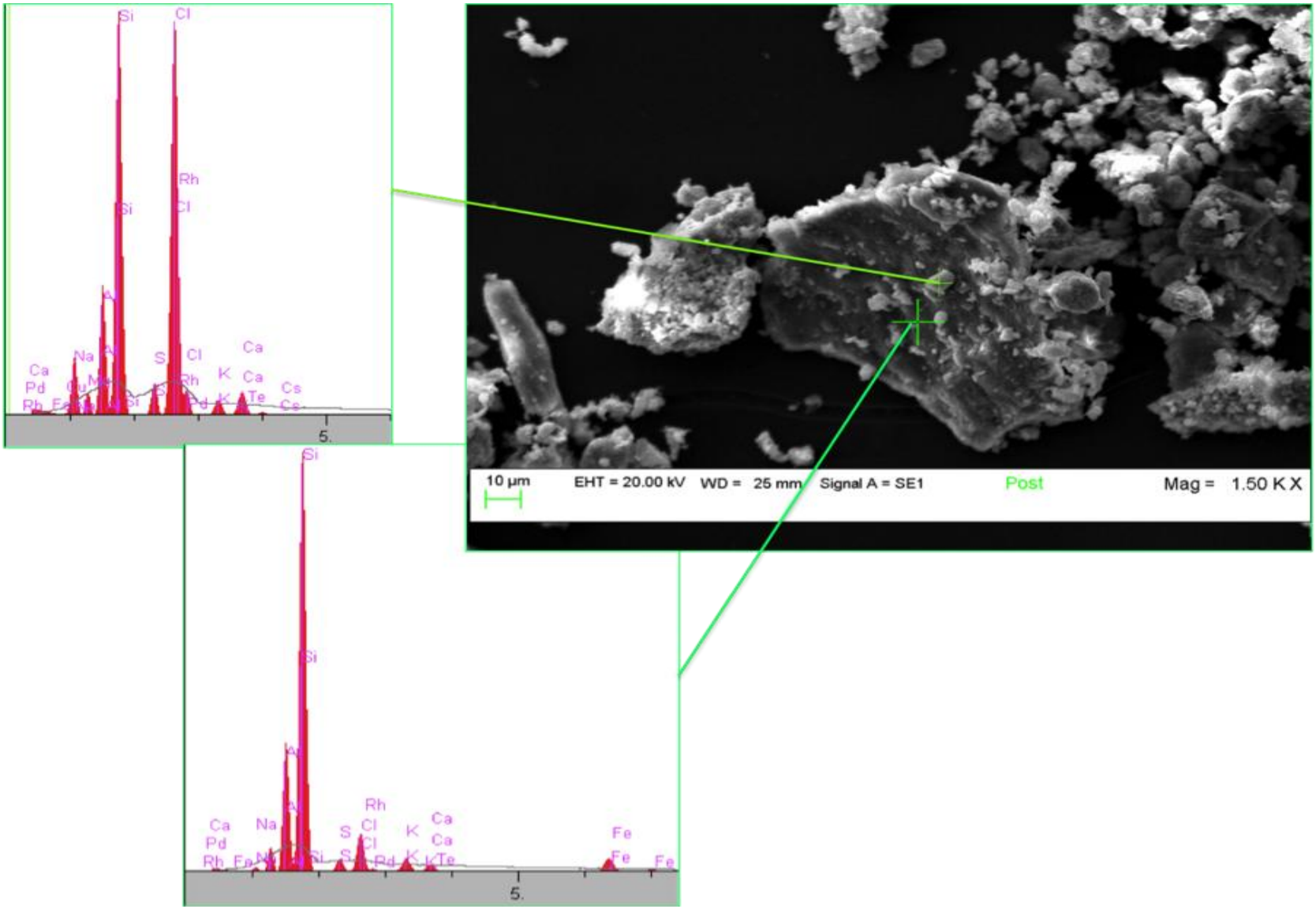

Figure 4.3.3: SEM Image of Post-Clay Gel with Corresponding EDS Results.

5 DISCUSSION PART I

XRD data showed that Pre-Clay Powder produced a broad diffraction hump that is similar to the pattern of Opal-CT with no 060 peak. 060 peaks are frequently seen in clay octahedral layers. The absence of one may suggest that further treatments need to be added to complete the formation of sepiolite (i.e. pressure, heat, or geological time). Opal-CT is a common mineral connected to smectites and its presence indicates high levels of silica in the pore fluid (Christidis, 2009). Both Pre-Clay Powder and SWy-2 experiments (Table 4.1.1) began with high levels of silica, so this connection is likely.

While there was no discernable difference between Post-Clay Gel and SWy-2 oriented (Figure 4.2.1), the 060 pattern (Figure 4.2.2) of Swy-2 did however have a Quartz peak that is no longer visible in the Post-Clay Gel pattern. The formation of Opal-CT could explain the disappearance of the peak, as the silica (SiO_2) would be hydrated. XRD analysis also showed the formation of salt crystals (Halite) on both Pre-Clay Powder and Post-Clay Gel, which is an expected result, due to the formation of the precipitates in Sea Water.

Table 5.1: Chemical Analysis of Pre-Clay Powder Compared with Natural and Synthetic Sepiolite.*

	Natural Sepiolite, Mid-Atlantic Ridge (Hathaway and Sachs, 1965)	Natural Sepiolite, Little Cottonwood, Utah (Nagy and Bradley, 1955)	Synthetic Sepiolite, (Wollast et al., 1968)	Pre-Clay Powder
SiO_2	45.8 wt %	53.0 wt %	47.6 wt %	67.6 wt %
MgO	23.8 wt %	22.5 wt %	20.0 wt %	26.2 wt %
MgO/SiO_2	0.6	0.6	0.7	0.6

* Adapted From Wollast et al (1968)

As expected, the XRF data (Table 4.1.1) showed that the ratio between MgO/SiO_2 decreased from 0.57 (Pre-Clay) to 0.23 (Post-Clay) and weight % Al_2O_3 increased from 3900 ppm (0.39 %) in Pre-Clay Powder to 133,400 ppm (13.34%) in Post-Clay Gel due to the addition of SWy-2, an Al-rich clay that sorbs Magnesium. Comparison of the Pre-Clay Powder precipitate to other synthetic and natural sepiolites (Table 5.1) indicates the MgO/SiO_2 ratio was too low and the creation of sepiolite did not fully occur. This is consistent with the possible precipitation of opaline silica suggested by XRD. To further explore this ratio SEM data was collected. EDS of SWy-2 (Figure 4.3.1) only indicates the presence of Al and Si, but both Pre-Clay Powder and Post-Clay Gel (Figures 4.3.2 and 4.3.3) showed no Mg in either product. This implies that SEM analysis was not representative of the products and the Mg present is most likely not homogeneously distributed throughout the sample. Because no Mg-Salts have been identified by the XRD, we must infer that the Mg present must be in the amorphous silicate phase.

These preliminary results provided some insight into the mineral formation of silicates. Regrettably, this experimental procedure produced an X-ray amorphous Mg-silicate gel, which had very little reaction to the addition of Al-rich smectite. Therefore future research with different experimental procedures and additional treatments would potentially better our understanding of the geochemical evolution of these products. For these reasons, another methodological approach was taken.

6 EXPERIMENTAL METHODS (PART II)

6.1 Hydrothermal Sepiolite Synthesis Experiment

6.1.1 Preparation of Magnesium Silicate Gel

Mizutani et al's (1991) sepiolite synthesis was replicated. Fifteen grams of sodium orthosilicate (Na_4SiO_4) (Fisher Scientific) was dissolved in 840 mL of deionized water, resulting in an alkaline solution of pH 13.5. This solution was acidified to pH 2.9 by the addition of 26 mL 12M HCl and 48.4 g of magnesium chloride hexahydrate ($MgCl_2 \cdot 6H_2O$). Forty-one milliliters of 1 M aqueous sodium hydroxide (NaOH) was then added at a rate of 0.3 mL per minute; during this step the solution became a turbid due to the precipitation of a viscous iridescent magnesium silicate gel with a final pH of 7.2 (Figure 6.1.1.1).

Figure 6.1.1.1: Solution Before (Left Image) and After (Right Image) the Addition of NaOH.

The suspension was allowed to sit overnight at room temperature for 24 hours and was then filtered using a 0.45 μm filter (Figure 6.1.1.2). Due to the viscosity of the gel, it took roughly three hours to filter a 10mL volume. Therefore the gel was centrifuged at 8000 rpm for 15 minutes, rinsed with deionized water and centrifuged again (Figure 6.1.1.3) before it was dried at 60° C for further analysis.

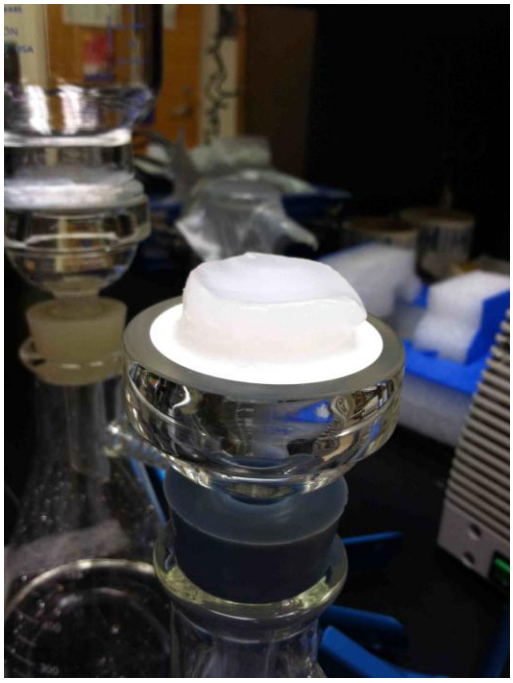

Figure 6.1.1.2: Magnesium Silicate Gel Being Filtered.

Figure 6.1.1.3: Centrifuged Gel Before Drying.

6.1.2 Hydrothermal Crystallization of the Magnesium Silicate Gel

The newly synthesized Mg-silicate gel (~0.07g) was seeded with 0.02 g of a purified submicron Clay Mineral Society Sepiolite Source Clay (Sep-sp-1) and suspended in 15 mL of deionized water. Purification of Sep-Sp-1 was used to obtained the >2 μm size fraction through centrifugation at 8000 rpm for 30 minutes. The suspension was then probe-sonicated with a Branson Digital Sonifier for three minutes before it was heated to 200° C for varying lengths of time in a Teflon lined Parr Instruments acid digestion vessel (Figure 6.1.2.1 and 6.1.2.2). The volume of

the vessel was 23 mL with 8 mL of headspace left for air. Samples were subjected to these conditions over 5, 25, 50, 120 and 242 hour time periods (Table 6.1.2.2). The time required for the temperature of the vessel to reach 200° C was not taken into account. Because the digestion vessel is a closed system, measurement of the temperature inside the Teflon cup during the experiment was not possible, and the exact time of temperature equilibration was unknown. Once the time period ended, samples were removed from the oven and allowed to cool overnight at ambient room temperature, before being removed from the Parr bomb. Precipitates were then filtered using a 0.22 µm Millipore filter and air dried for further analysis (Figure 6.1.2.3). The experiment was then repeated with the addition of Na-montmorillonite (SWy-2) in place of Sep-sp-1 (Figure 6.1.2.4). Blank standards were also heated for comparison (Table 6.1.2.1).

Table 6.1.2.1: Hydrothermal Reactions.

Sample Name	Swy-2 (g)	MgSi Gel (g)	H_2O (ml)	Temperature (°C)	Total Hours Heated
SWy2 Heat 50Hr Parr	0.07	0	15	200	50
MgSiGelSWy2Mix50Hr	0.02	0.078	15	200	50
2NewMgSiGelSWy2Mix	0.02	0.081	15	200	50
3NewMgSiGelSWy2Mix	0.021	0.079	15	200	50
LessNewMgSiGelSwY2Mix	0.02	0.045	15	200	50
2XMgSiGelSWy2Mix	0.021	0.157	15	200	50
MgSiGelSWy2Mix0Hr	0.025	0.075	15	0	0
MgSiGelSWy2Mix5Hr	0.021	0.071	15	200	5
MgSiGelSWy2Mix25Hr	0.022	0.077	15	200	25
MgSiGelSWy2Mix72Hr	0.021	0.08	15	200	72
MgSiGelSWy2Mix120Hr	0.02	0.078	15	200	120
MgSiGelSWy2Mix242Hr	0.021	0.072	15	200	242

Sample Name	Sep-Sp-1 (g)	MgSi Gel (g)	H_2O (ml)	Temperature (°C)	Total Hours Heated
HeatedSEP	0.076	0	15	200	50
MgSiGelSepMix50Hr	0.02	0.076	15	200	50
2NewMgSiGelSepMix	0.021	0.079	15	200	50
LessMgSiGelSepMix50Hr	0.02	0.051	15	200	50
MgSiGelSepMix0Hr	0.021	0.075	15	0	0
MgSiGelSepMix5Hr	0.022	0.079	15	200	5
MgSiGelSepMix25Hr	0.02	0.072	15	200	25
MgSiGelSepMix120Hr	0.02	0.08	15	200	120
MgSiGelSepMix242Hr	0.02	0.073	15	200	242

Sample Name	MgSi Gel (g)	H_2O (ml)	Temperature (°C)	Total Hours Heated
HeatedNewMgSiGel5Hr	0.077	15	200	5
HeatedNewMgSiGel25Hr	0.085	15	200	25
HeatedNewMgSiGel50Hr	0.077	15	200	50
HeatedNewMgSiGel120Hr	0.083	15	200	120
HeatedNewMgSiGel242Hr	0.075	15	200	242

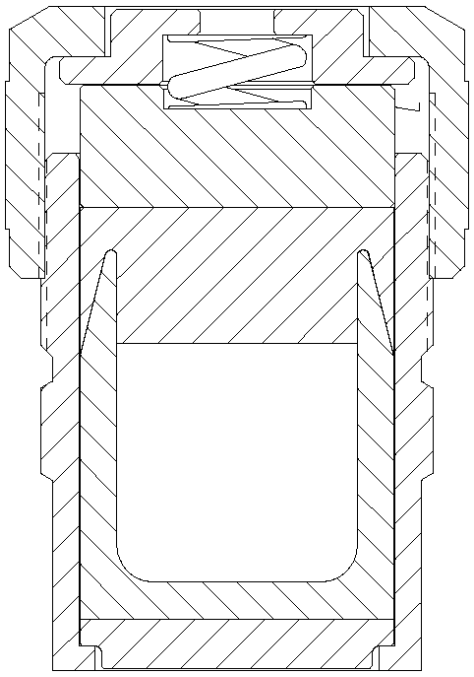

Figure 6.1.2.1: Cross-Section of a Acid Digestion Parr Bomb.*[+]

Figure 6.1.2.2: Parr Bomb External View.

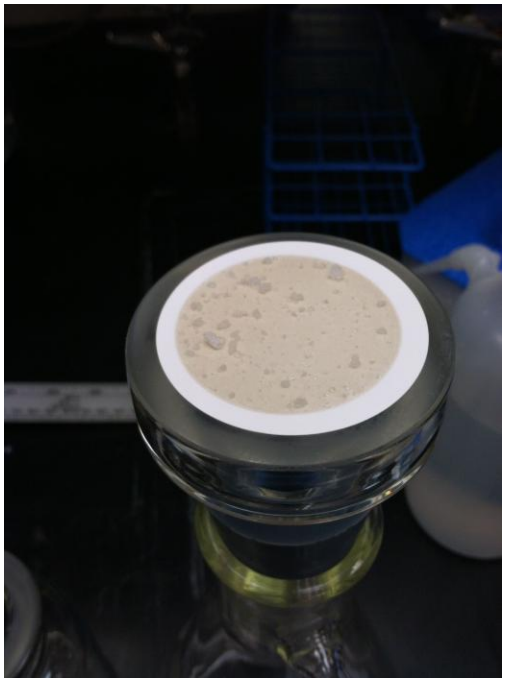

Figure 6.1.2.3: MgSiGel/ Sep-Sp-1 Mix Product.

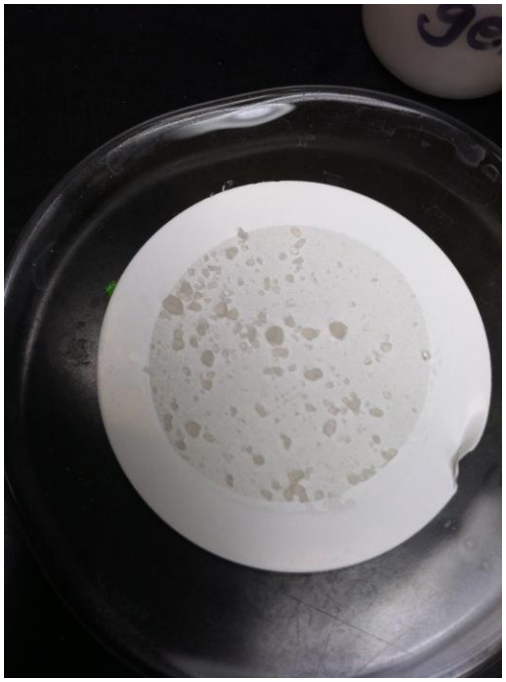

Figure 6.1.2.4: MgSiGel / SWy-2 Mix Product

[+] * http://www.parrinst.com/products/sample-preparation/acid-digestion/design-features/

6.2 Sample Preparation

XRF samples were prepared as described in Section 3.2, but due to low volume of experimental products only standards and the un-heated Mg-Silicate Gel were analyzed. XRD samples and standards were prepared as described in Section 3.3 and SEM/EDS samples were prepared as described in Section 3.4.

6.2.1 ICP-OES Sample Preparation

A sample of the newly synthesized Mg-Silicate Gel was sent to the Environmental Research Laboratory at GSU for further elemental analysis. The sample digestion was a modification of the Nitric, Hydrofluoric, Perchloric digestion. A LeForte or inverse aqua regia was used for the first step instead of straight nitric acid. After digestion the sample was diluted to 50 ml, with a final acid concentration of 0.5% HNO_3. The digest was then analyzed by ICP-OES.

7 RESULTS PART II

7.1 XRF

Table 7.1.1: Corrected Major Elemental Composition in Weight Percent (wt%).

Sample	SiO_2 (wt %)	TiO_2 (wt %)	Al_2O_3 (wt %)	Fe_2O_3 (wt %)	MnO (wt %)	MgO (wt %)
Sep-sp-1	68.12	0.24	1.51	0.52	0.01	29.45
Mg-Silicate Gel	77.58	0.03	0.27	0.13	0	20.04
SWy-2	65.92	0.14	22.81	4.88	0.01	3.26

Sample	CaO (wt %)	Na_2O (wt %)	K_2O (wt %)	P_2O_5 (wt %)	MgO/SiO_2
Sep-sp-1	0.15	0	0.15	0.06	0.65
Mg-Silicate Gel	0.01	1.95	0	0.01	0.41
SWy-2	0.93	1.84	0.18	0.02	0.07

Table 7.1.2: MgO/SiO_2 Ratios for Each Sample.

	MgO/SiO_2
Sep-sp-1	0.65
SWy-2	0.07
Mg-Silicate Gel	0.41
Pre-Clay Powder (Previous Work)	0.57
Post-Clay Gel (Previous Work)	0.23

XRF analysis (Table 7.1.1) of the Mg-Silicate Gel revealed it was composed of 77.58 wt% SiO_2 and 20.04 wt % MgO with an MgO/SiO_2 ratio of 0.41. This was ratio was compared to previous work and Sep-sp-1 (Table 7.1.2 and Figure 7.1.1) and is slightly lower than the Sepiolite Standard (Sep-sp-1) of 0.65.

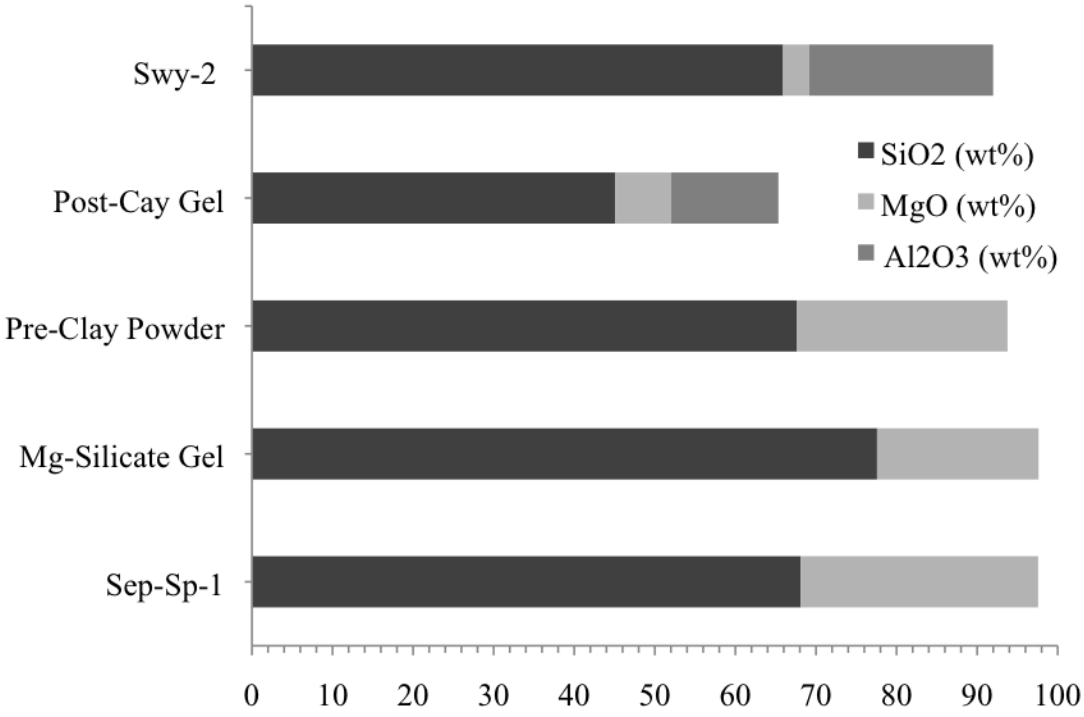

Figure 7.1.1: Major Elemental Composition of Samples (wt%).

7.2 XRD

7.2.1 X-ray Diffraction of the Magnesium Silicate Gel

The creation of the Mg-Silicate gel produced a broad diffraction hump from ~3.0 – 5.0 Å (Figure 7.2.1), but the 060 peak associated with clay octahedral sheets was not apparent (Figure 7.2.2). Heating the Mg-Si gel for varying lengths of time revealed the formation of three main peaks at ~4.5 Å, 2.5 Å, and 1.5 Å (Figure 7.2.1.3). These newly created peaks shifted to the right just slightly as time increased. Peak height also increased linearly with heating time, suggesting changes in crystallinity (Table 7.2.1.1 and Figure 7.2.1.4).

To ensure that the precipitate created was in fact a repetition of the same structure and not two different phases, peak height was compared to one another (Figures 7.2.1.7-9). R^2 values revealed moderate to weak correlation between Peaks 1 and 2 (Figure 7.2.1.6) and Peaks 1 and 3 (Figure 7.2.1.8), but indicated a stronger correlation ($R^2 = 0.90$) between Peaks 2 and 3 (Figure 7.2.1.7). When examining the newly formed 060 peaks over time (Figure 7.2.1.5) both peak height (cts) and peak area (cts* °2Theta) increased. The Full Width at Half Maximun (FWHM) (°2Theta) decreased (Table 7.2.1.2 and Figure 7.2.1.6), indicating an increase in crystallinity of octahedral layers. These measurements were taken using High Score Plus profile fit (Figures 7.2.1.10-15).

Note: All Peak Heights (cts) were determined after removing background values.

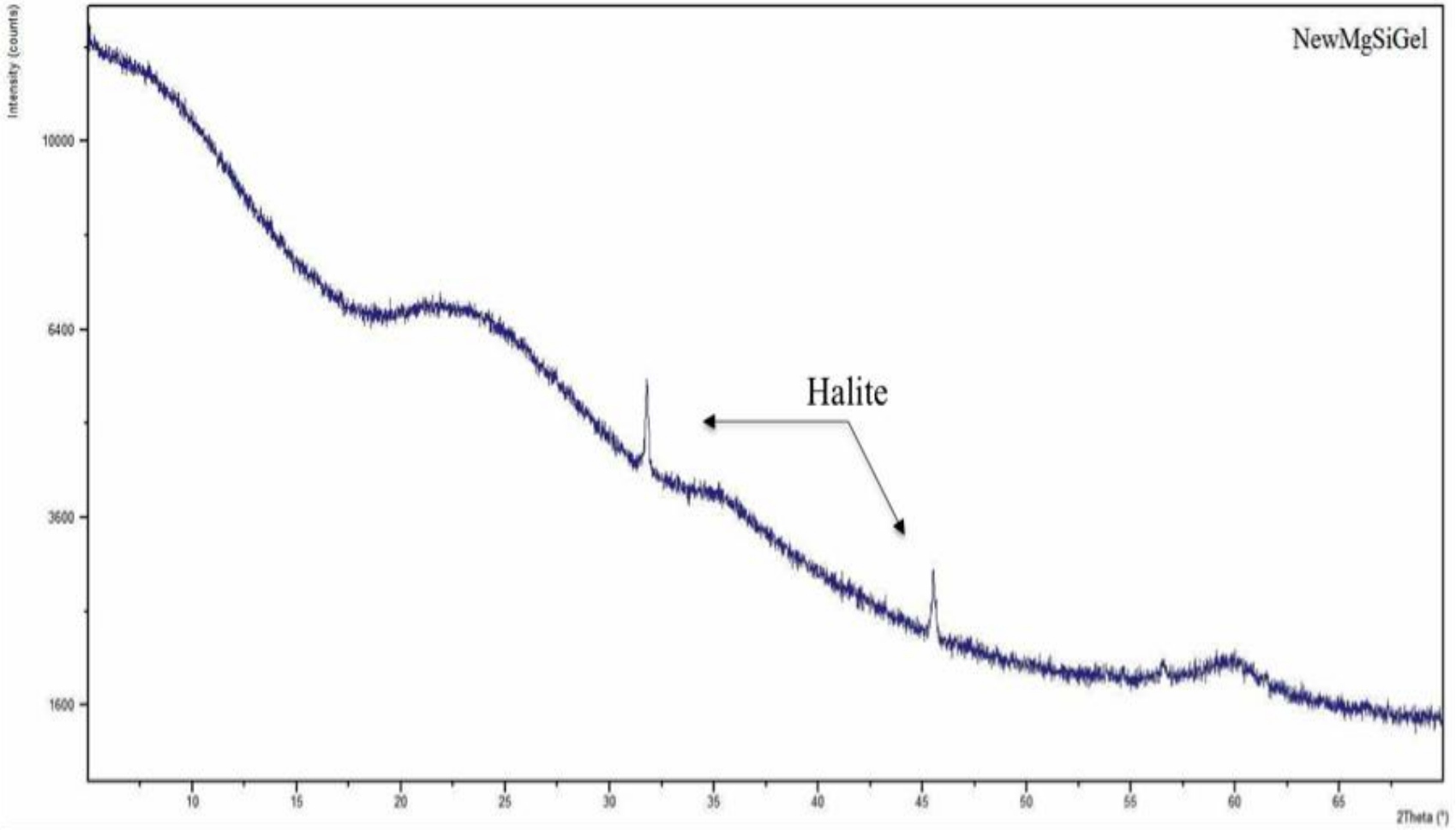

Figure 7.2.1.1: Diffractogram of Mg-Silicate Gel from 5-70 Degrees.

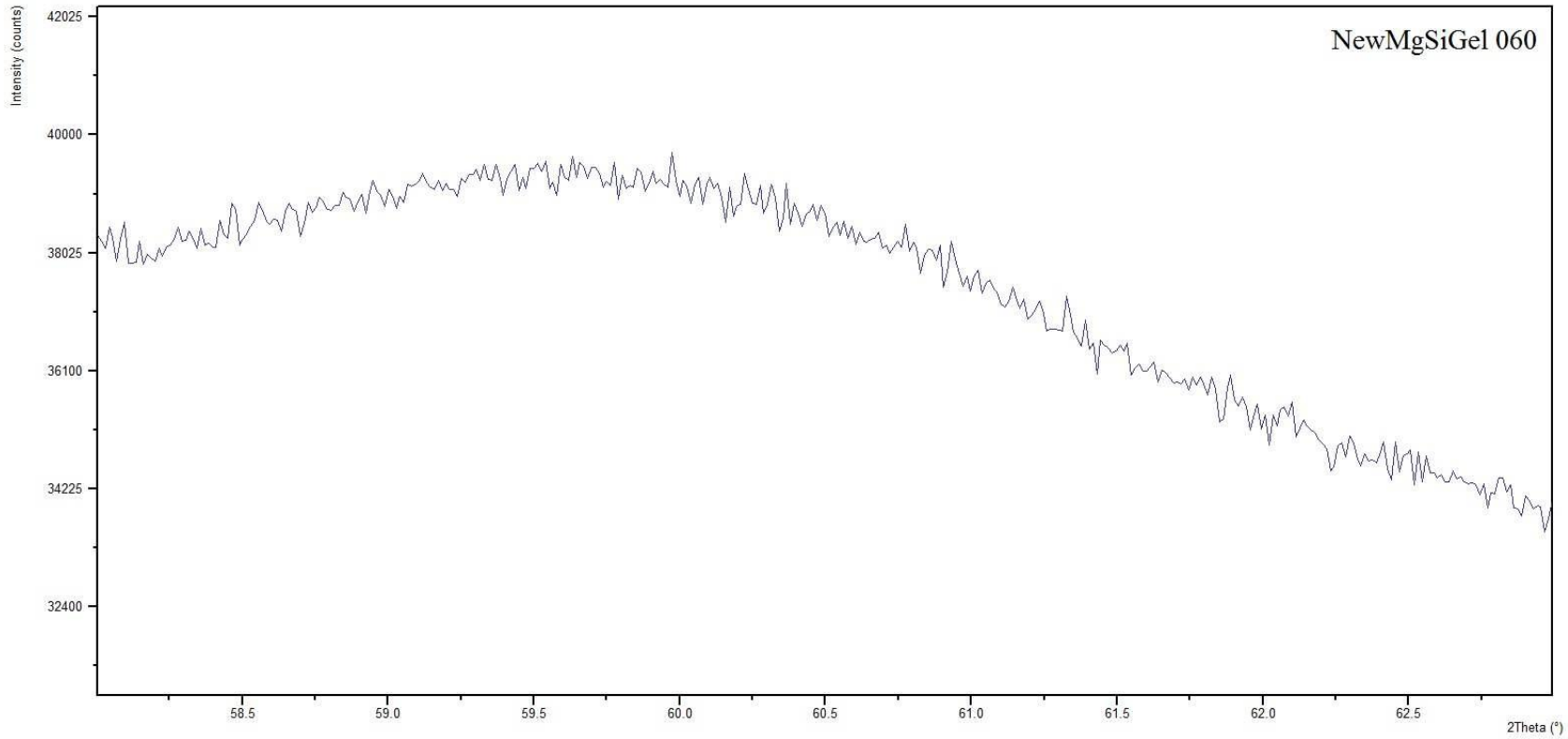

Figure 7.2.1.2: Diffractogram of Mg-Silicate Gel from 59-62 Degrees.

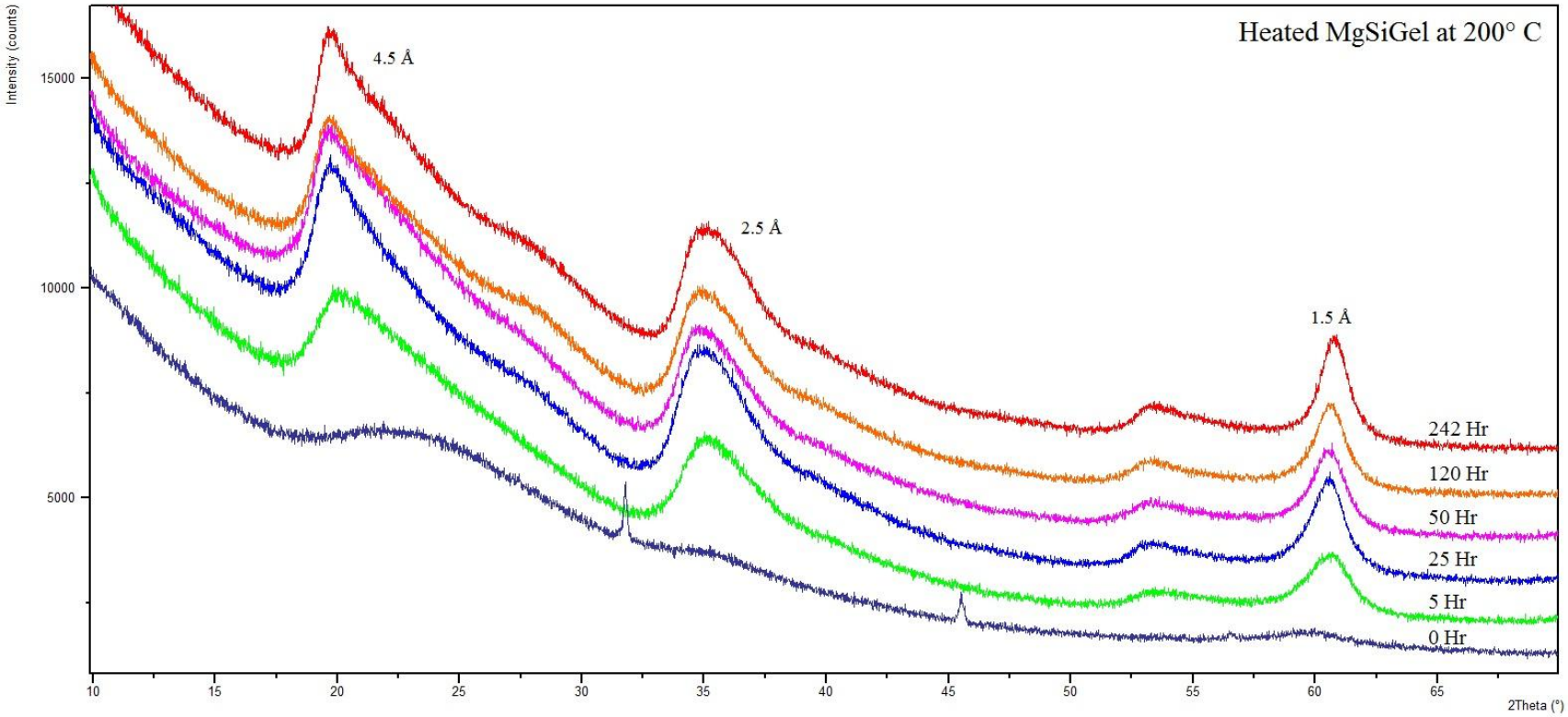

Figure 7.2.1.3: Diffractogram of Heated Mg-Silicate Gel at 200°C from 5-70 Degrees.

Table 7.2.1.1: Heated MgSiGel Peak Height Over Time at 200°C.

		PEAK 1	PEAK 2	PEAK 2a	PEAK 3
Name	**Time Heated at 200^0 C (hrs)**	**Height (cts)**	**Height (cts)**	**Height (cts)**	**Height (cts)**
NewMgSiGel	0	0	0	0	0
HeatedNewMgSiGel5Hr	5	2187	2066	523	1275
HeatedNewMgSiGel25Hr	25	3430	2898	672	2098
Heated NewMgSiGel50Hr	50	3528	2523	676	1745
HeatedNewMgSiGel120Hr	120	3055	2551	713	1845
HeatedNewMgSiGel242Hr	242	3292	2795	856	2326

Note: Peak Heights were determined after removing background values.

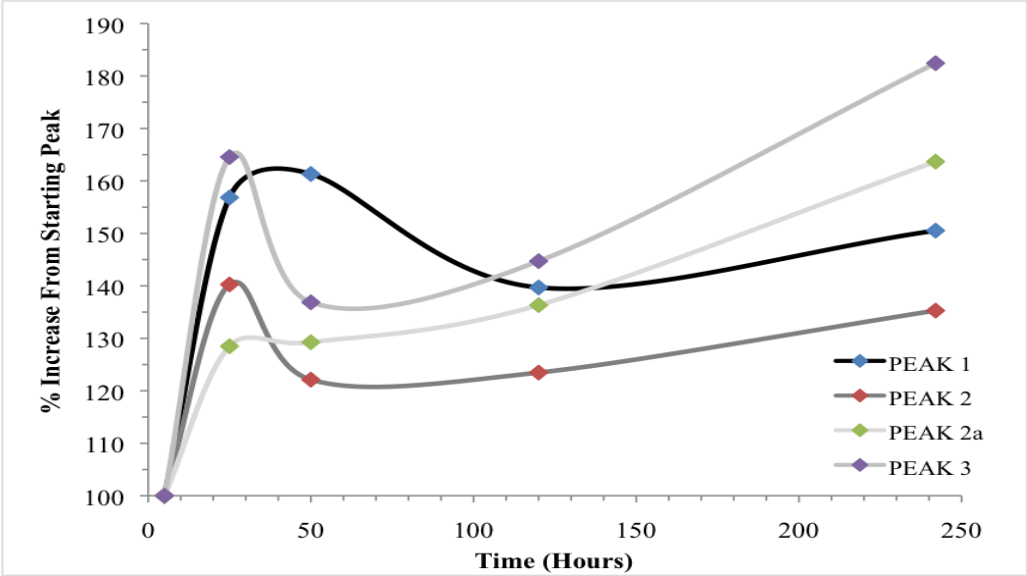

Figure 7.2.1.4: Percent Increase in Peak Height Over Time at 200°

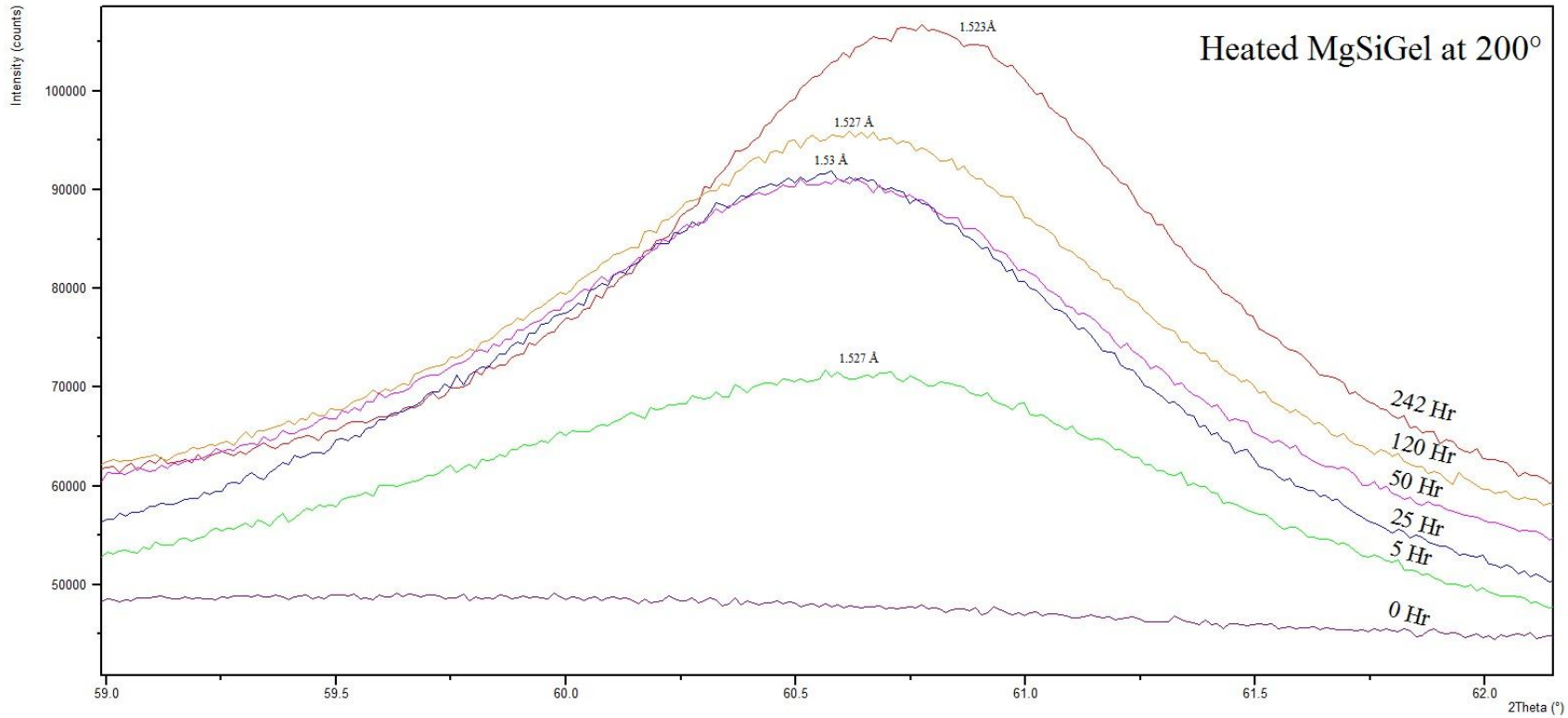

Figure 7.2.1.5: Diffractogram of Heated Mg-Silicate Gel at 200°C from 59-62 Degrees.

Table 7.2.1.2: Changes In MgSiGel 060 Peaks Over Time at 200°C.

Name	Time Heated at 200°C (hrs)	Height (cts)	FWHM (°2Theta)	Area (cts*°2Theta)
NewMgSiGel060	0	0	0	0
HeatedNewMgSiGel5Hr060	5	17950.35	1.9698	49054.14
HeatedNewMgSiGel25Hr060	25	20854.09	1.3248	36319.18
Heated NewMgSiGel50Hr060	50	22129.80	1.4004	38326.08
HeatedNewMgSiGel120Hr060	120	26717.69	1.4366	53237.66
HeatedNewMgSiGel242Hr060	242	33922.55	1.2684	61756.77

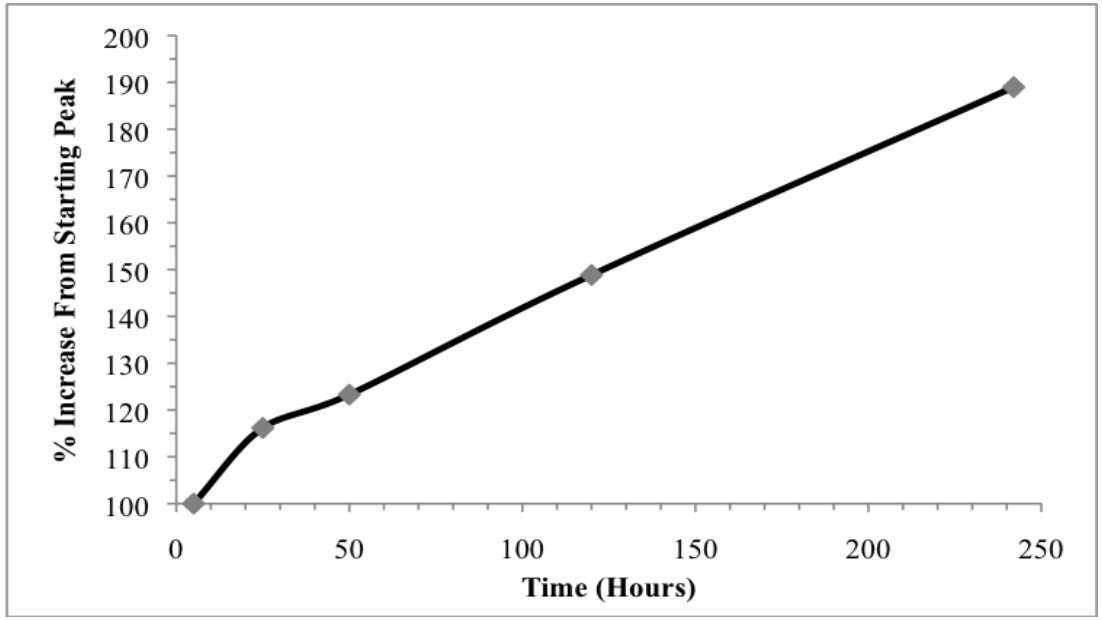

Figure 7.2.1.6: Percent Increase in 060 Peak Heights Over Time at 200°C

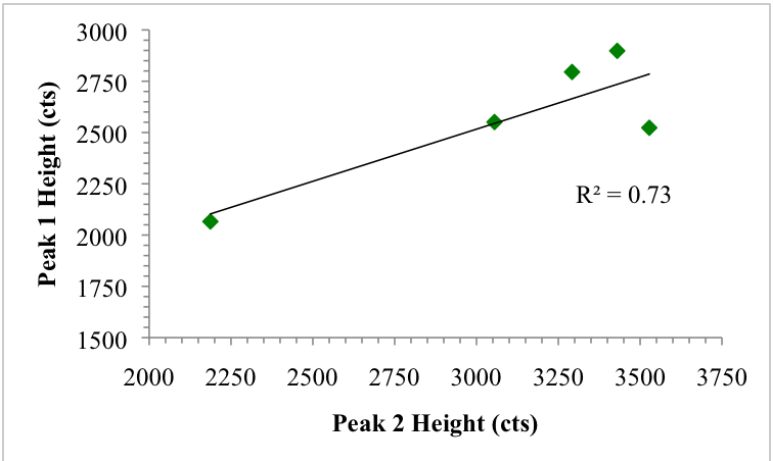

Figure 7.2.1.7: Peak 1 Height (cts) vs. Peak 2 Height (cts).

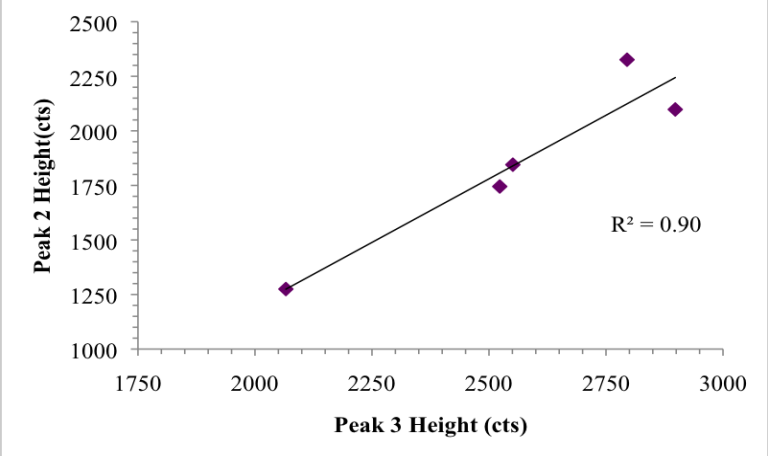

Figure 7.2.1.8: Peak 2 Height (cts) vs. Peak 3 Height (cts).

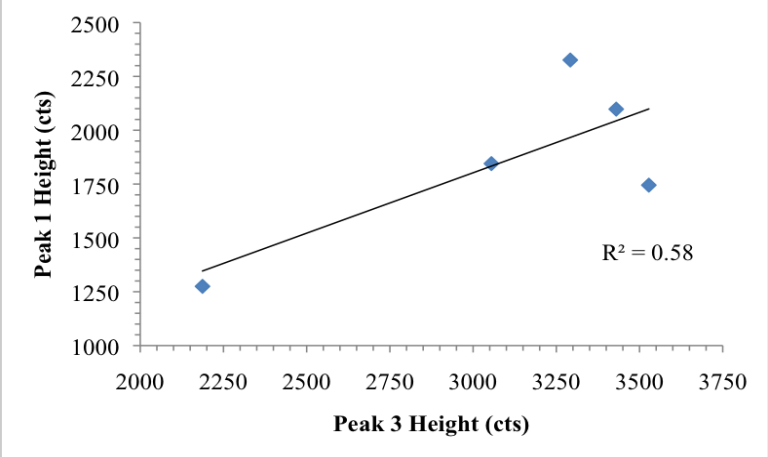

Figure 7.2.1.9: Peak 1 Height (cts) vs. Peak 3 Height (cts).

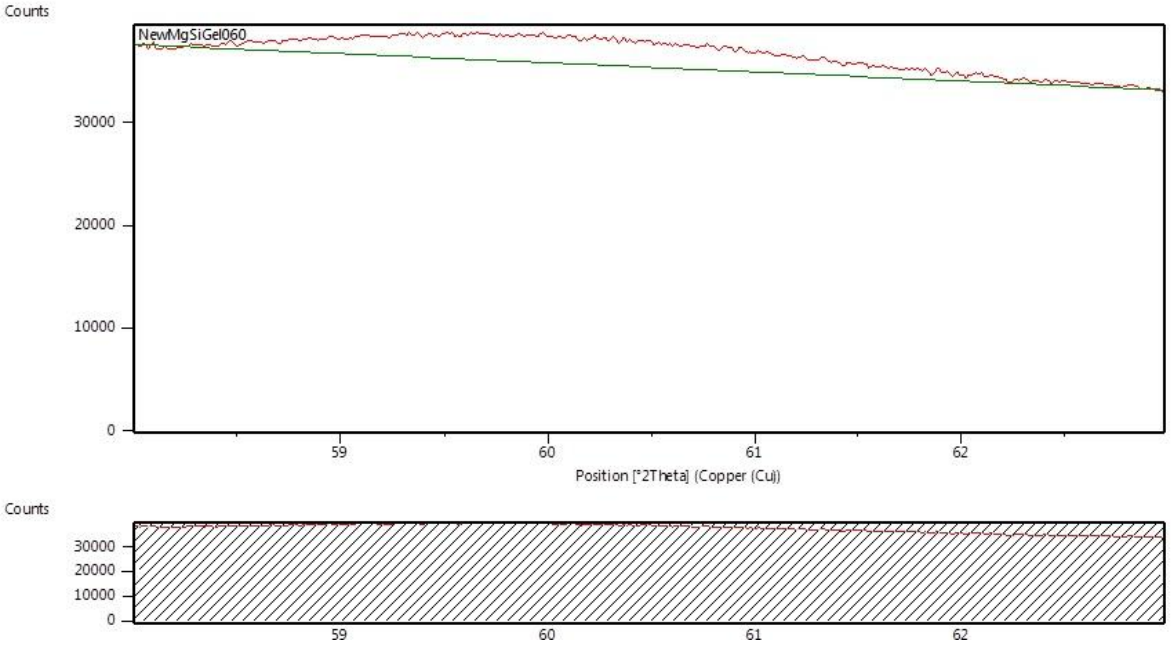

Figure 7.2.1.10: Individual HeatedNewMgSiGel0Hr 060 Peak, showing Fit Profile peak used for crystallinity determination.

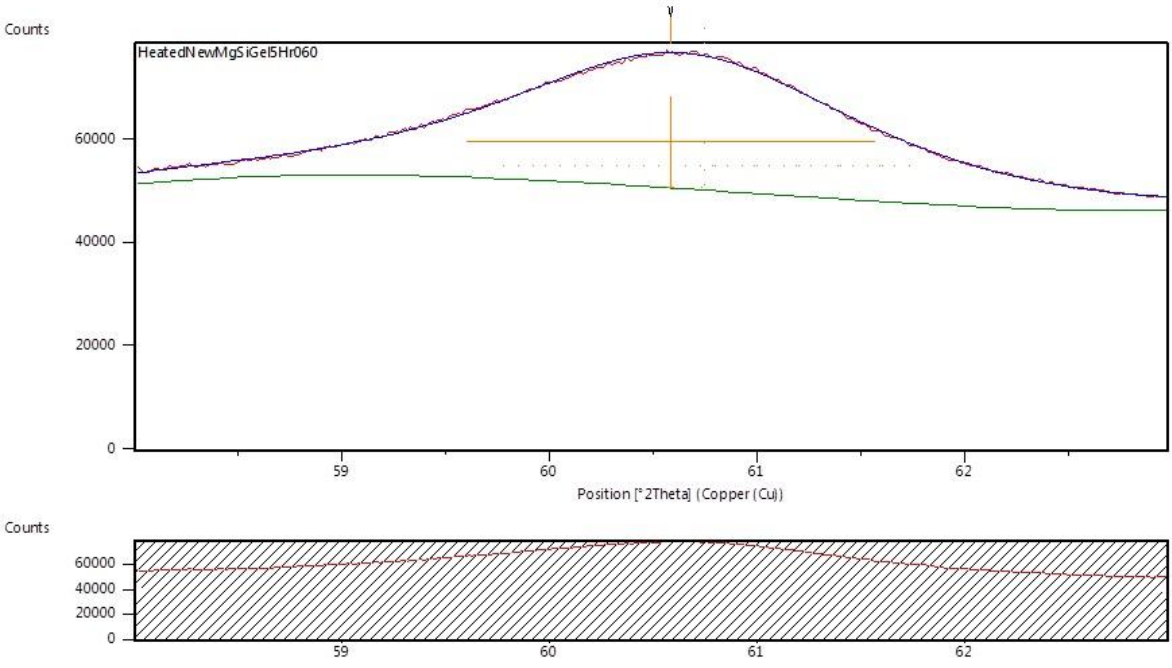

Figure 7.2.1.11: Individual HeatedNewMgSiGel5Hr 060 Peak, showing Fit Profile peak used for crystallinity determination.

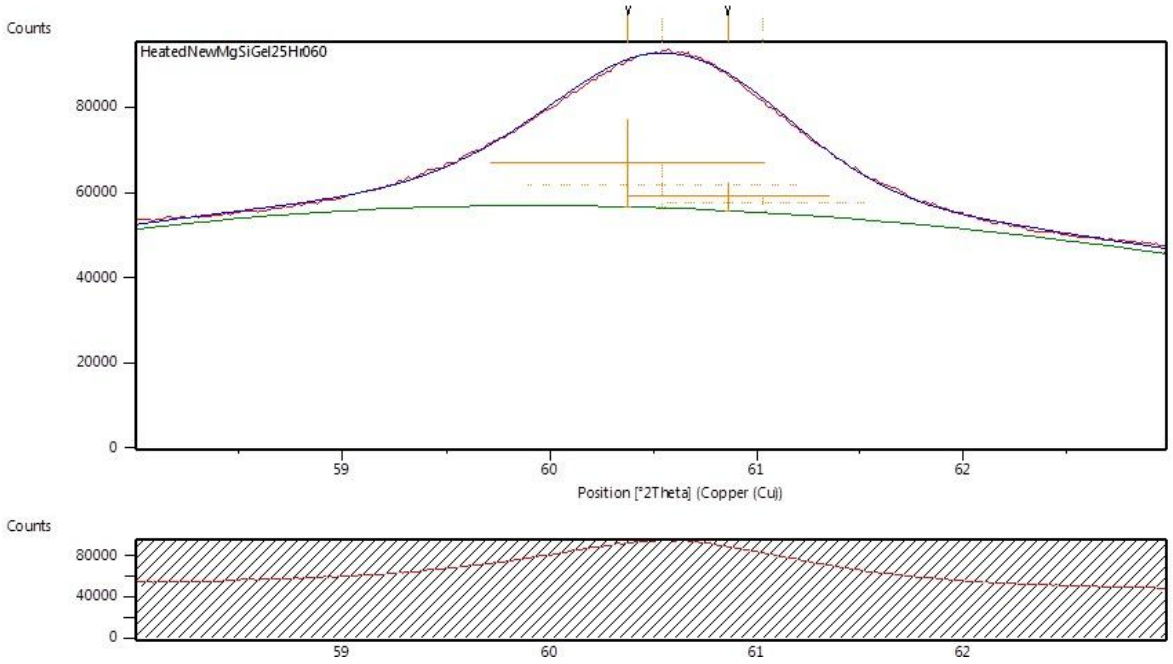

Figure 7.2.1.12: Individual HeatedNewMgSiGel25Hr 060 Peak, showing Fit Profile peak used for crystallinity determination.

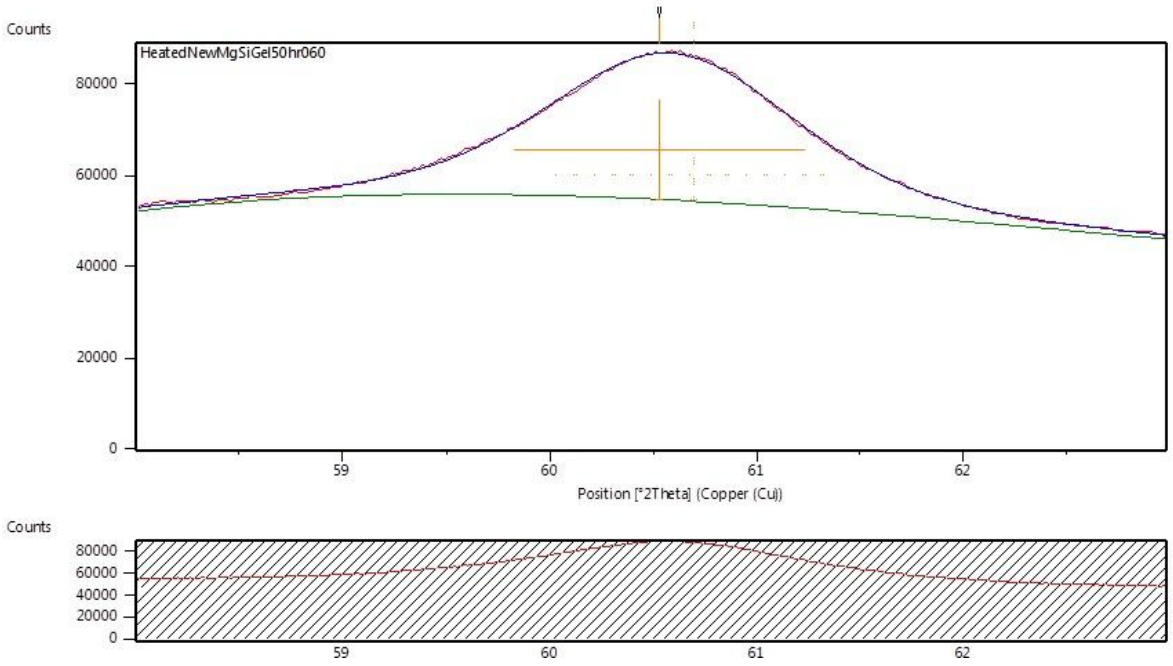

Figure 7.2.1.3: Individual HeatedNewMgSiGel50Hr 060 Peak, showing Fit Profile peak used for crystallinity determination.

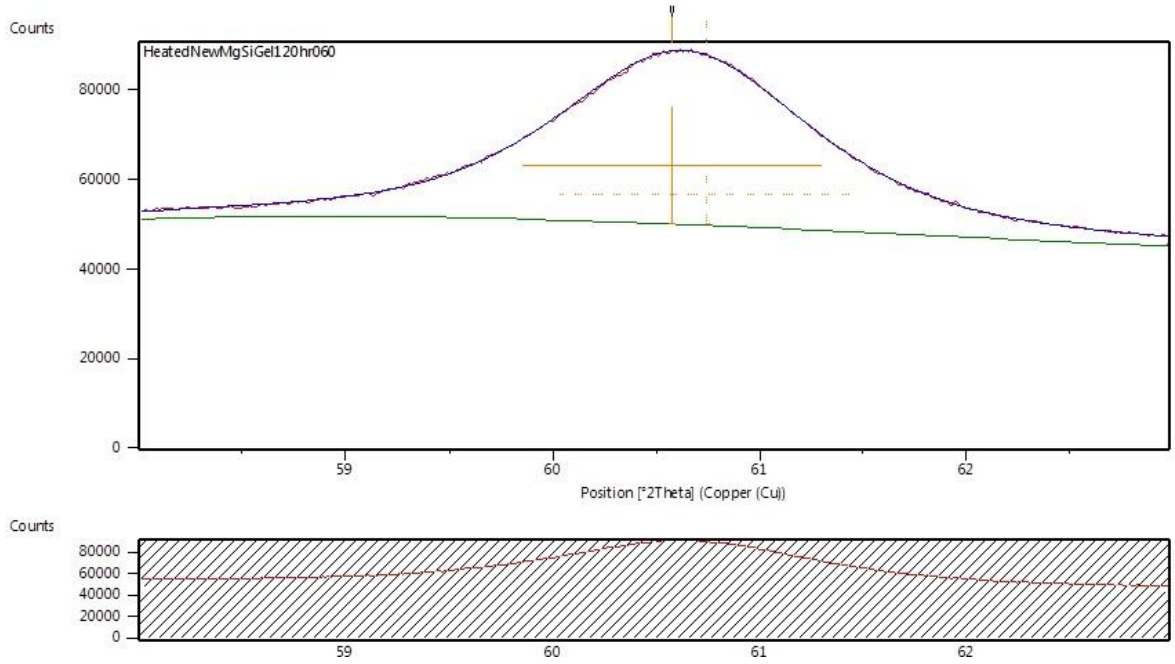

Figure 7.2.1.14: Individual HeatedNewMgSiGel120Hr 060 Peak, showing Fit Profile peak used for crystallinity determination.

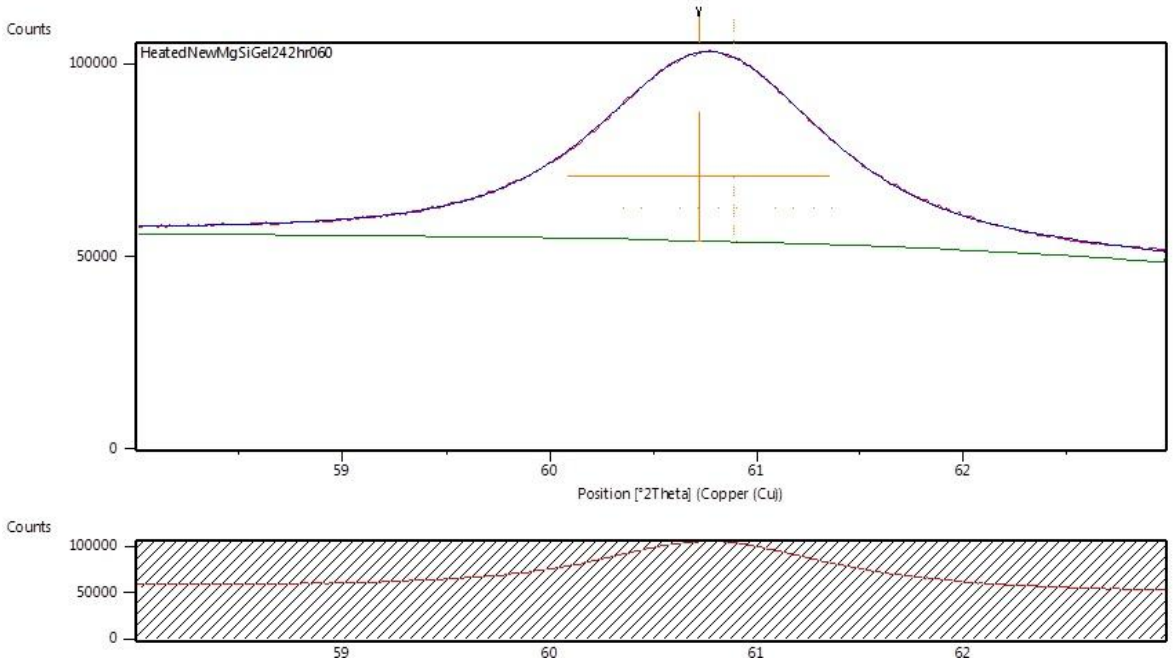

Figure 7.2.1.15: Individual HeatedNewMgSiGel242Hr 060 Peak, showing Fit Profile peak used for crystallinity determination.

7.2.2 X-ray Diffraction of the Magnesium Silicate Gel Mixed with Sepiolite (Sep-Sp-1)

After combining the Mg-Silicate Gel with Sep-sp-1 the precipitate had no key differences from Sep-sp-1 by oriented XRD analysis (Figure 7.2.2.1), but a slight expansion of the Sep-sp-1 060 peak was observed in d-spacings, or the spacing between layers of atoms, from ~ 1.549 to 1.52 Å in randomly oriented mounts (Figure 7.2.2.2). To ensure that these changes occurred due to the addition of the MgSiGel, Sep-sp-1 was heated to 200° C for 50 hours inside a Parr bomb, and showed no difference from Sep-sp-1 oriented XRD from both 5-70 degrees (Figure 7.2.2.3) and in the 060 peaks (Figure 7.2.2.4).

The experiment was then repeated with the addition of less MgSiGel and this resulted in no discernable difference from the first sample run (Figure 7.2.2.5) in oriented XRD, but the previous expansion of Sep-Sp-1 060 peak (~ 1.555 to 1.52 Å) did not fully occur (Figure 7.2.2.6). The addition of less MgSiGel resulted in the formation of the original Sep-Sp-1 060 peak (1.549 Å), as well as a slight expansion of a secondary peak from 1.517 Å to 1.518 Å. The valley between these two peaks disappeared in both cases.

When examining the changes in heated MgSiGel/Sep-Sp-1 Mix over time (Figure 7.2.2.7) there was no key difference in oriented XRD from 10 – 55 degrees, but large changes in the 011 peaks (6 – 8 degrees) (Figure 7.2.2.8) and 060 peaks (59 – 62 degrees) (Figure 7.2.2.11) occurred. Sep-Sp-1 normally has a 011 peak at 12.2 Å, as heating time increased, peak height (cts) and area (cts*^{0}2Theta) generally decreased and FWHM (^{0}2Theta) increased, indicating a decrease in both intensity and crystallinity of the products. D-spacing also expanded from 12.2 Å to 14.0 Å as heating time increased (Table 7.2.2.1 and Figure 7.2.2.9), indicating an expansion between crystal layers while overall crystallinity decreased and the mineral became less sepiolite

like. Figures 7.2.2.10 and 7.2.2.11 show the individual 011 peak changes over time, as well as profile fit used for 011 peak height determination.

In contrast to the 011 peak's irregular shifts, the 060 peaks (Figure 7.2.2.12) expanded over time in a more organized fashion. The original Sep-Sp-1 060 peak is found at 1.549 Å with a secondary peak at 1.517 Å, as seen in Table 7.2.2.2. The 060 peak height generally decreased while the secondary peak height increased and the valley between the two peaks disappeared (Figure 7.2.2.13). As time heated for the MgSiGel/Sep-Sp-1 Mix increased the two peaks moved closer towards each other (060 collapsing, secondary peak expanding) until the single resulting 1.524 Å peak emerged at 242 hours. Changes in individual peak movements are tracked in Figures 7.2.2.15 and 7.2.2.15. With time the 060 peaks become less Sepiolite like and more Mg-Silicate Gel like. This difference between the 011 and the 060 peak behaviors suggests more stability in the octahedral sheet once it is formed, whereas other crystallographic aspects of the sepiolite may be more easily reorganized.

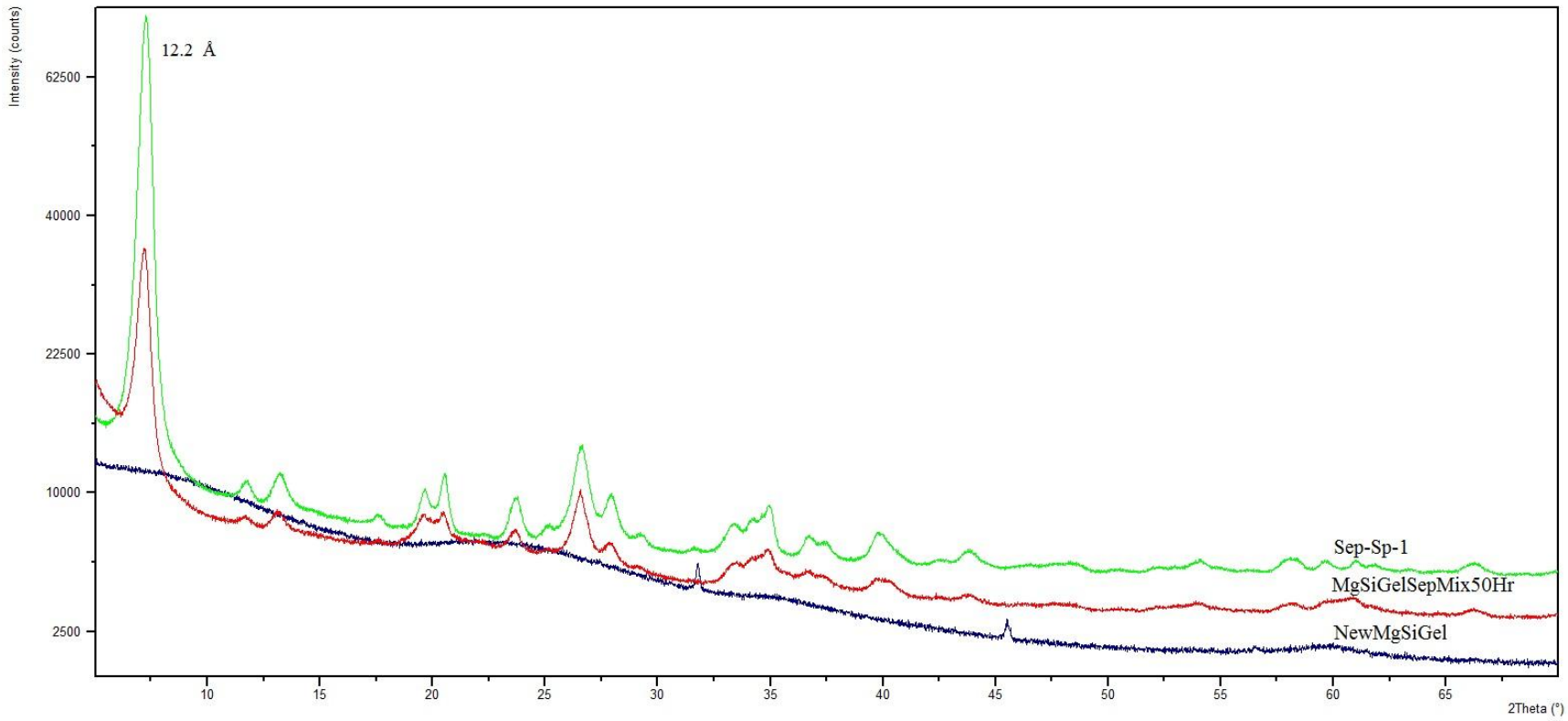

Figure 7.2.2.1: Diffractogram of Mg-Silicate Gel, Sep-sp-1 and Mg-Silicate/Sep-sp-1 Combined from 5-70 Degrees.

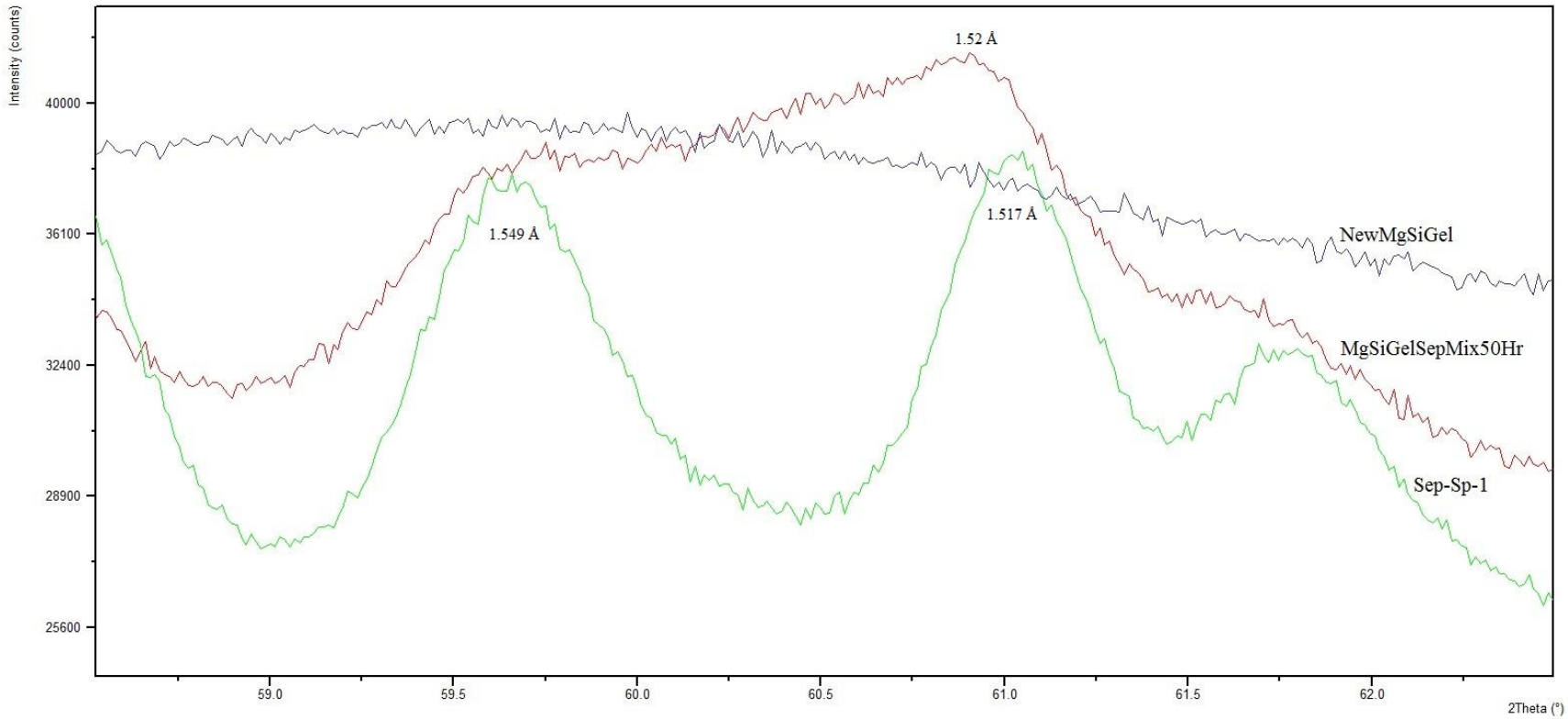

Figure 7.2.2.2: Diffractogram of Mg-Silicate Gel, Sep-sp-1 and Mg-Silicate/Sep-sp-1 Combined from 59-62 Degrees.

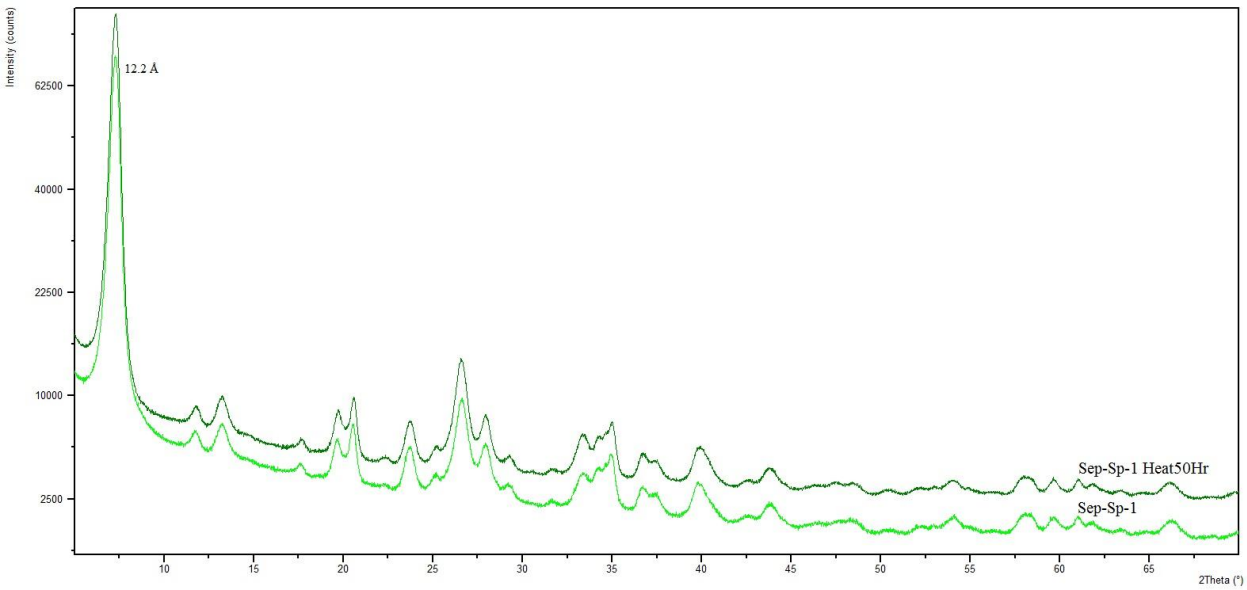

Figure 7.2.2.3: Sep-Sp-1 compared to Sep-Sp-1 Heated for 50 Hours at 200°C, 5-70 Degrees.

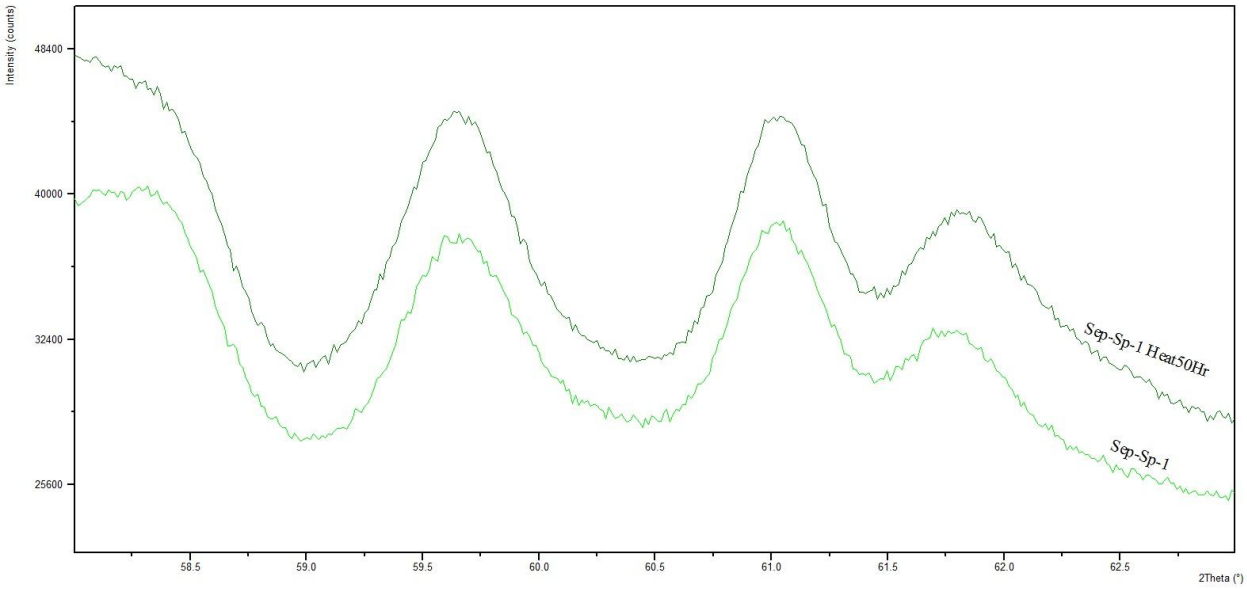

Figure 7.2.2.4: Sep-Sp-1 compared to Sep-Sp-1 Heated for 50 Hours at 200°C, Showing 060 Peaks.

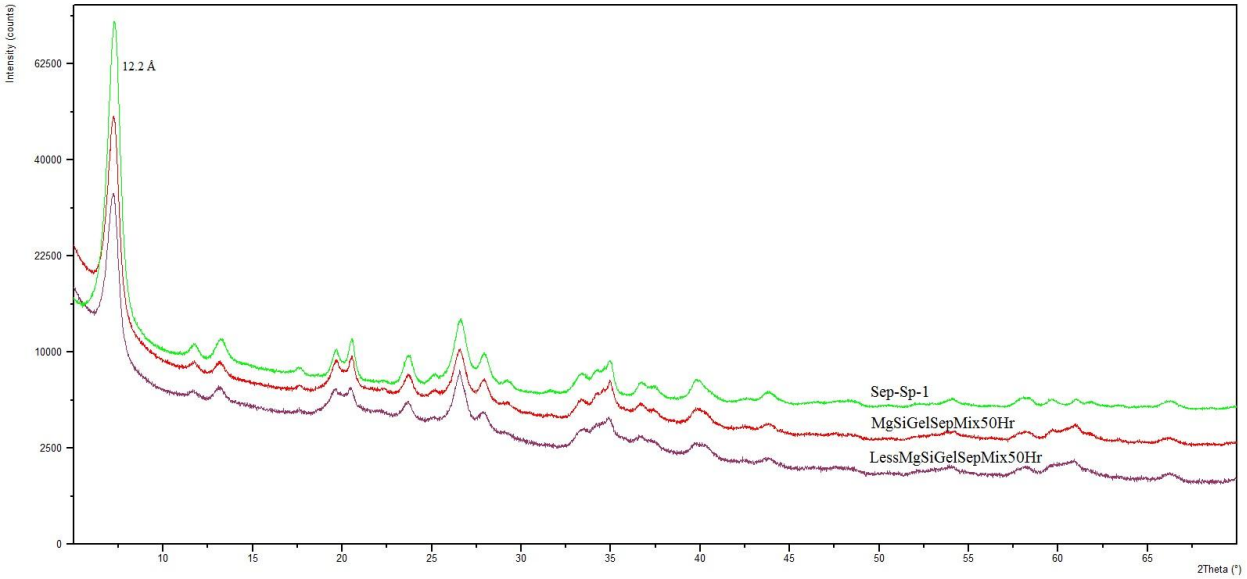

Figure 7.2.2.5: Less MgSiGel 5-70 Degrees.

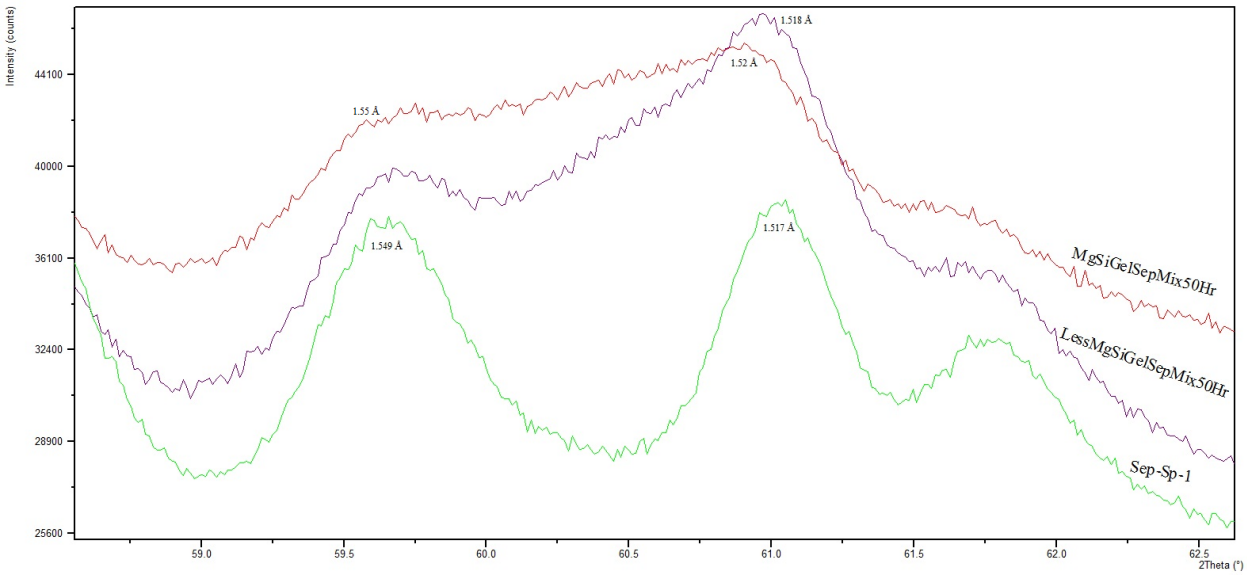

Figure 7.2.2.6: Less MgSiGel 59-62 Degrees.

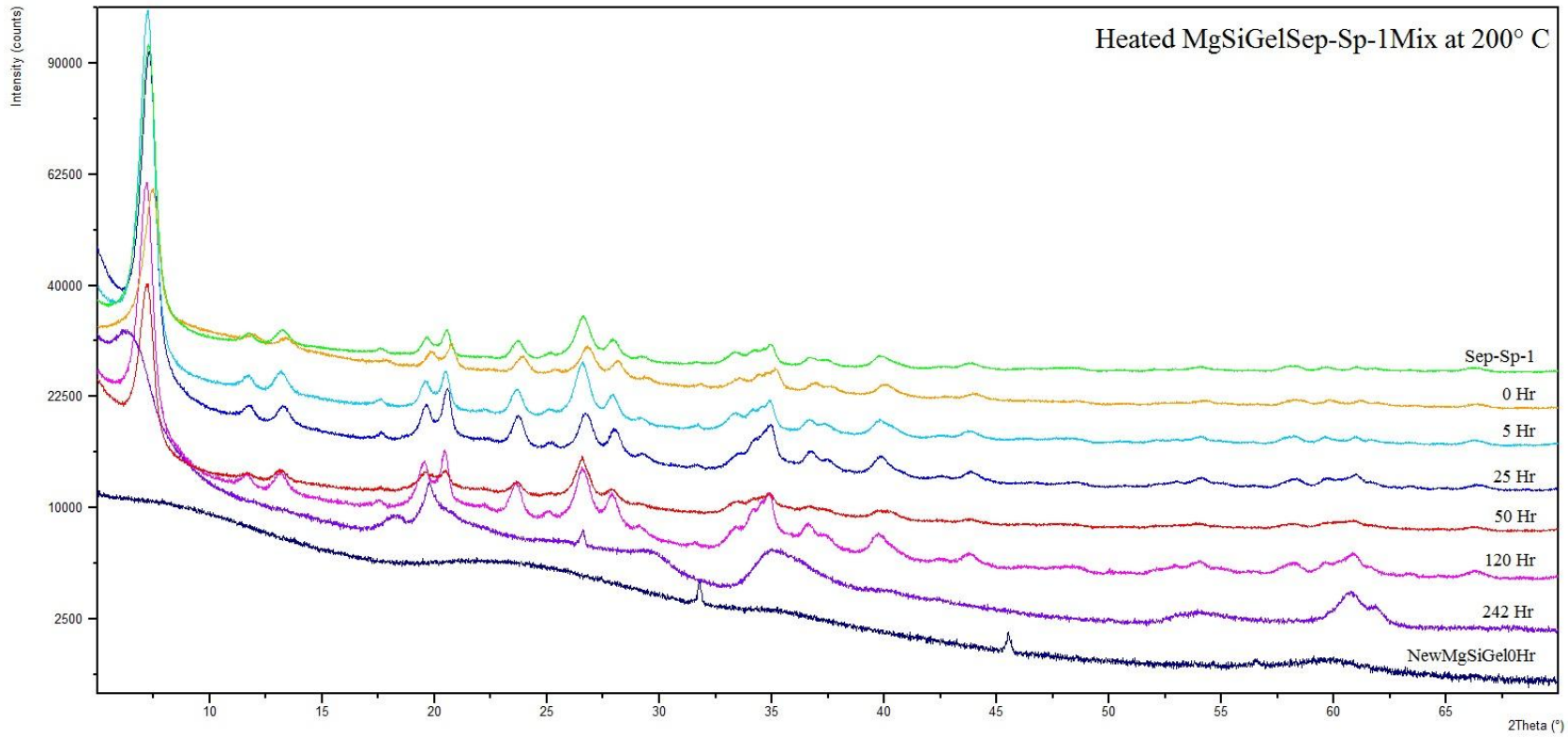

Figure 7.2.2.7: Diffractogram of Heated MgSiGel/ Sep-Sp-1 Mix at 200°C from 5-70 Degrees.

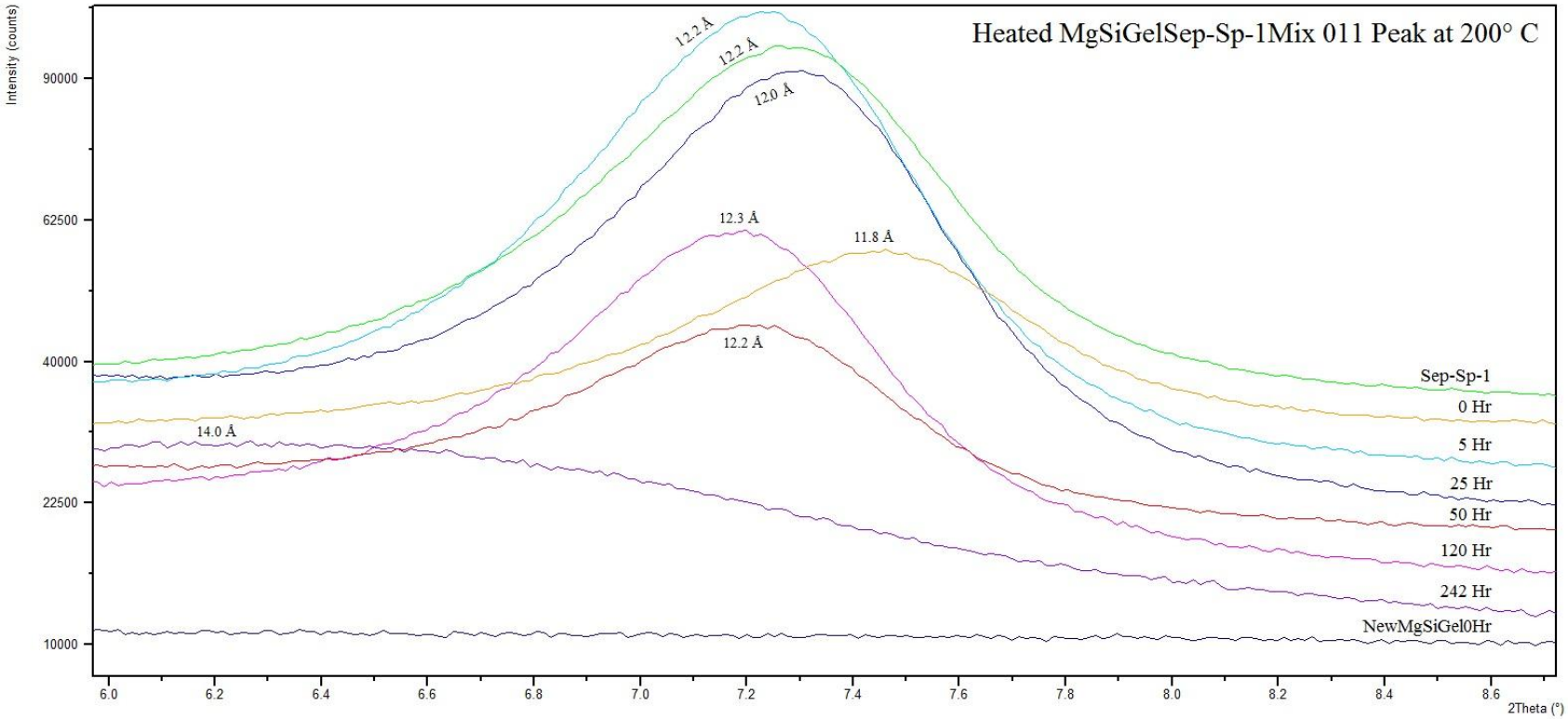

Figure 7.2.2.8: Diffractogram of Heated MgSiGel/ Sep-Sp-1 Mix at 200°C focusing on 011 Peak (6-8 degrees).

Table 7.2.2.1: Changes In MgSiGel/Sep-Sp-1Mix 011 Peaks Over Time at 200°C.

Name	Time Heated at 200^{0}C (hrs)	Height (cts)	FWHM (^{0}2Theta)	Area (cts*^{0}2Theta)	d-spacing
Sep-Sp-1	0	41603.88	0.7292	41328.61	12.2 Å
MgSiGelSepMix0Hr	0	18349.33	0.7279	19987.20	11.8 Å
MgSiGelSepMix5Hr	5	50192.73	0.6641	43997.78	12.2 Å
MgSiGelSepMix25Hr	25	43001.74	0.6510	36677.76	12.0 Å
MgSiGelSepMix50Hr	50	15368.06	0.6506	13375.44	12.2 Å
MgSiGelSepMix120Hr	120	28603.53	0.6597	27197.65	12.3 Å
MgSiGelSepMix242Hr	242	6019.92	1.3648	8745.35	14.0 Å

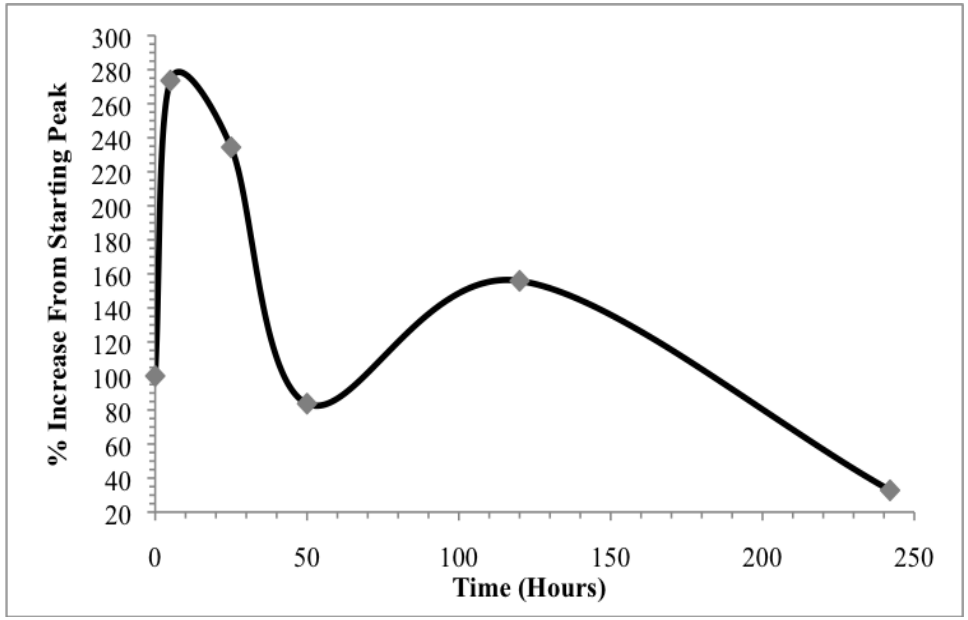

Figure 7.2.2.9: Percent Increase in 011 Peak Heights Over Time at 200°C.

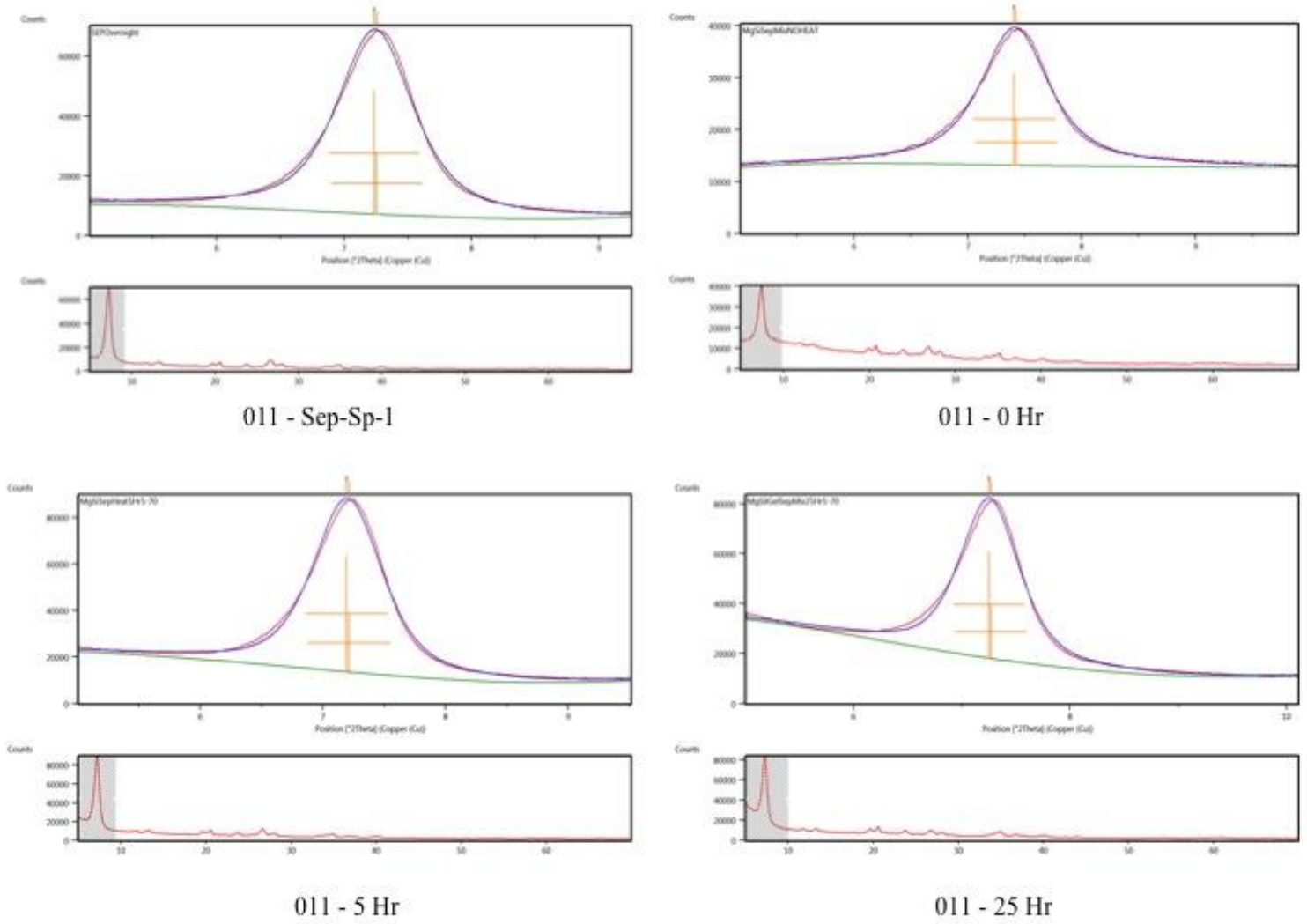

Figure 7.2.2.10: Individual Heated MgSiGel/ Sep-Sp-1 Mix 011 Peaks, showing Fit Profile used for crystallinity determination.

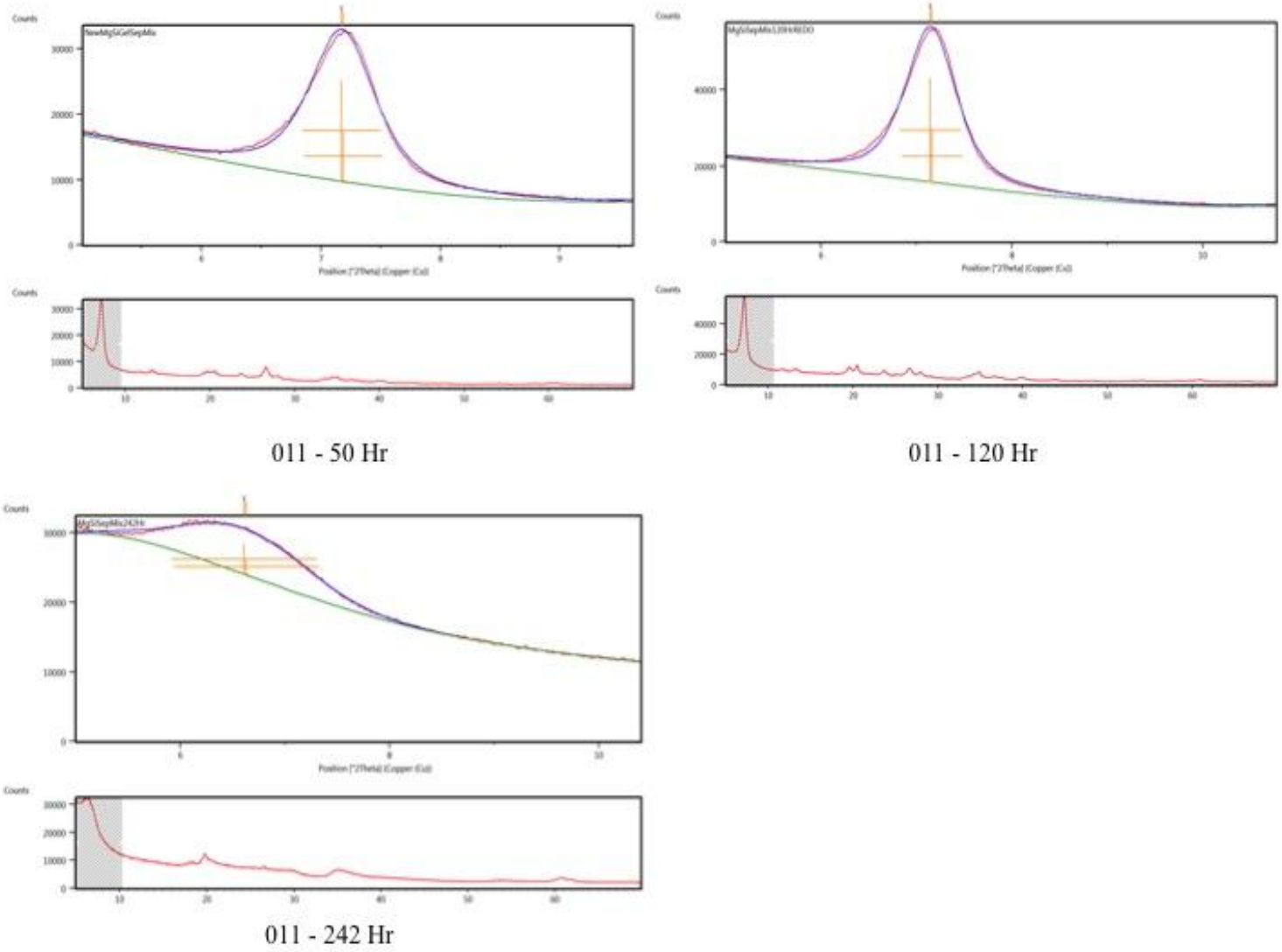

Figure 7.2.2.11: Individual Heated MgSiGel/ Sep-Sp-1 Mix 011 Peaks, showing Fit Profile used for crystallinity determination.

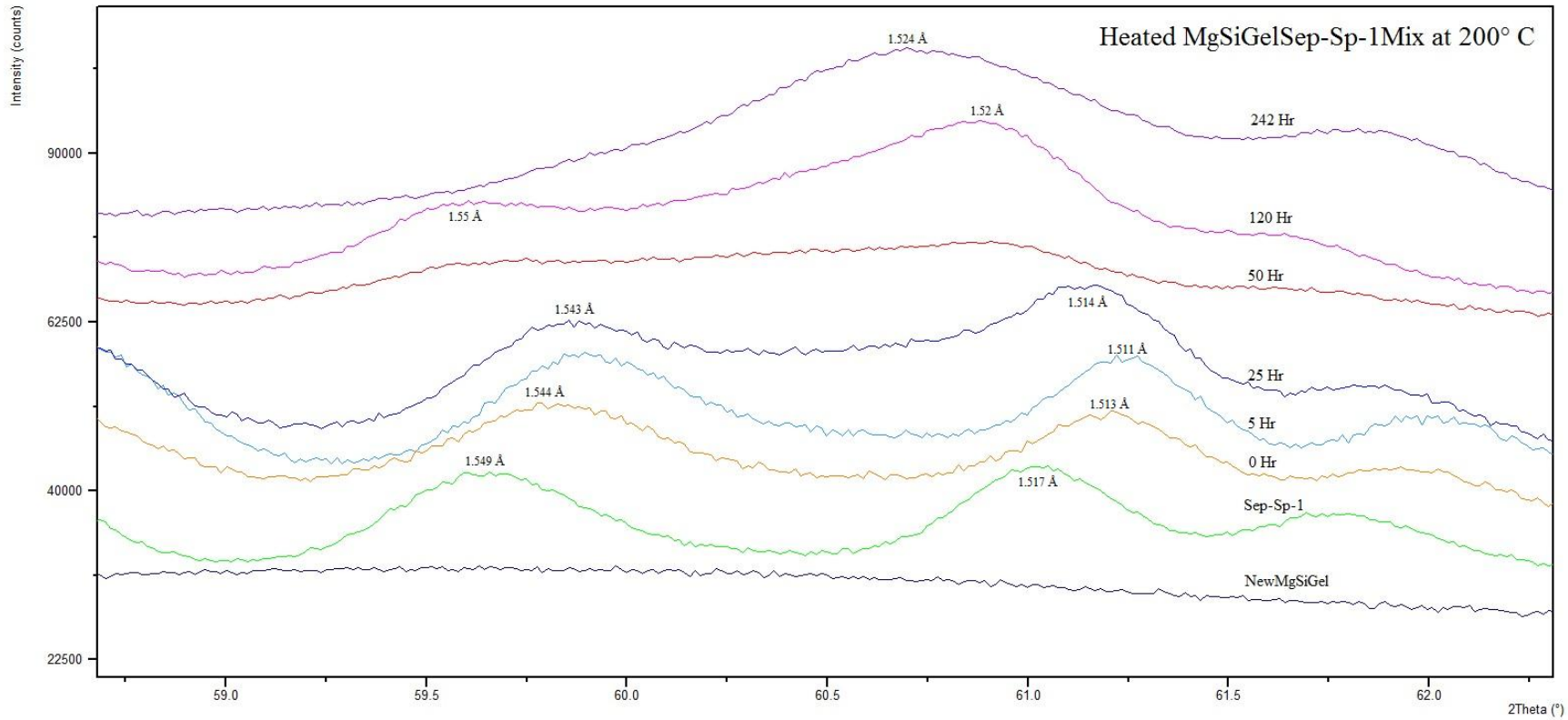

Figure 7.2.2.12: Diffractogram of Heated MgSiGel/ Sep-Sp-1 Mix at 200°C from 59-62 Degrees.

Table 7.2.2.2: Changes In MgSiGelSep-Sp-1Mix 060 Peaks Over Time at 200°C.

Name	Time Heated at 200^{0}C (hrs)	Peak 1 Height (cts)	Peak 2 Height (cts)	060 Peak d-spacing	2nd Peak d-spacing
Sep-Sp-1	0	8578.03	8153.51	1.549 Å	1.517 Å
MgSiGelSepMix0Hr	0	7047.74	6623.56	1.544 Å	1.513 Å
MgSiGelSepMix5Hr	5	10152.59	8668.37	1.543 Å	1.511 Å
MgSiGelSepMix25Hr	25	7946.57	9957.66	1.543 Å	1.514 Å
MgSiGelSepMix50Hr	50	4037.64	5568.73	1.55 Å	1.52 Å
MgSiGelSepMix120Hr	120	9287.82	20014.37	1.55 Å	1.52 Å
MgSiGelSepMix242Hr	242	-	20501.61	-	1.524 Å

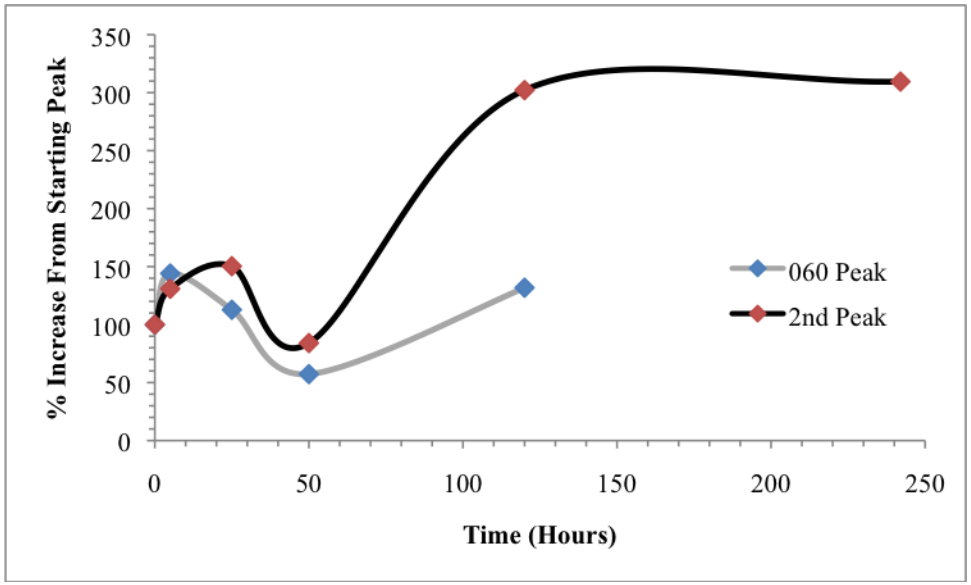

Figure 7.2.2.13: Percent Increase in 060 Peak Heights Over Time at 200°C.

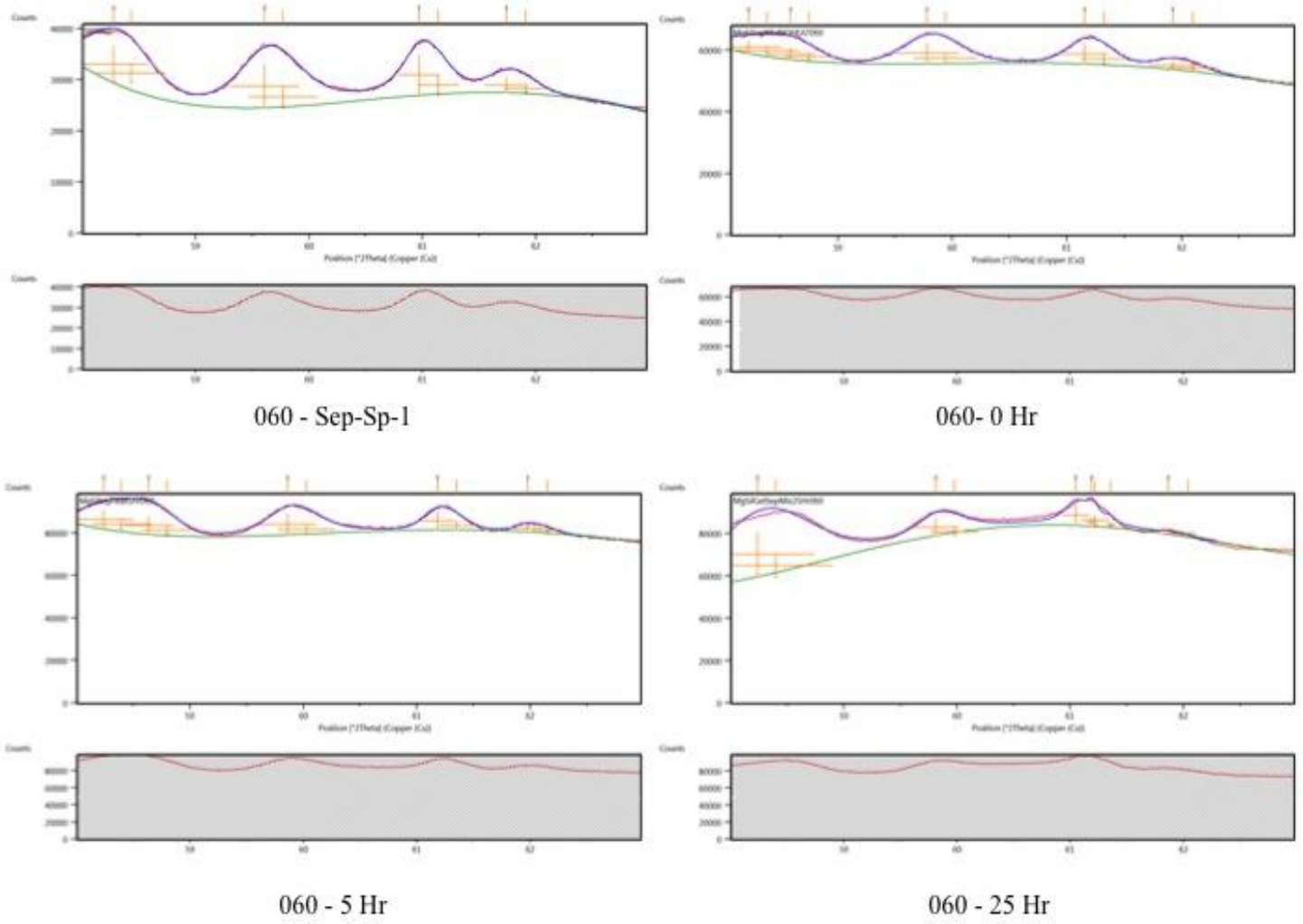

Figure 7.2.2.14: Individual Heated MgSiGel/ Sep-Sp-1 Mix 060 Peaks, showing Fit Profile used for crystallinity determination.

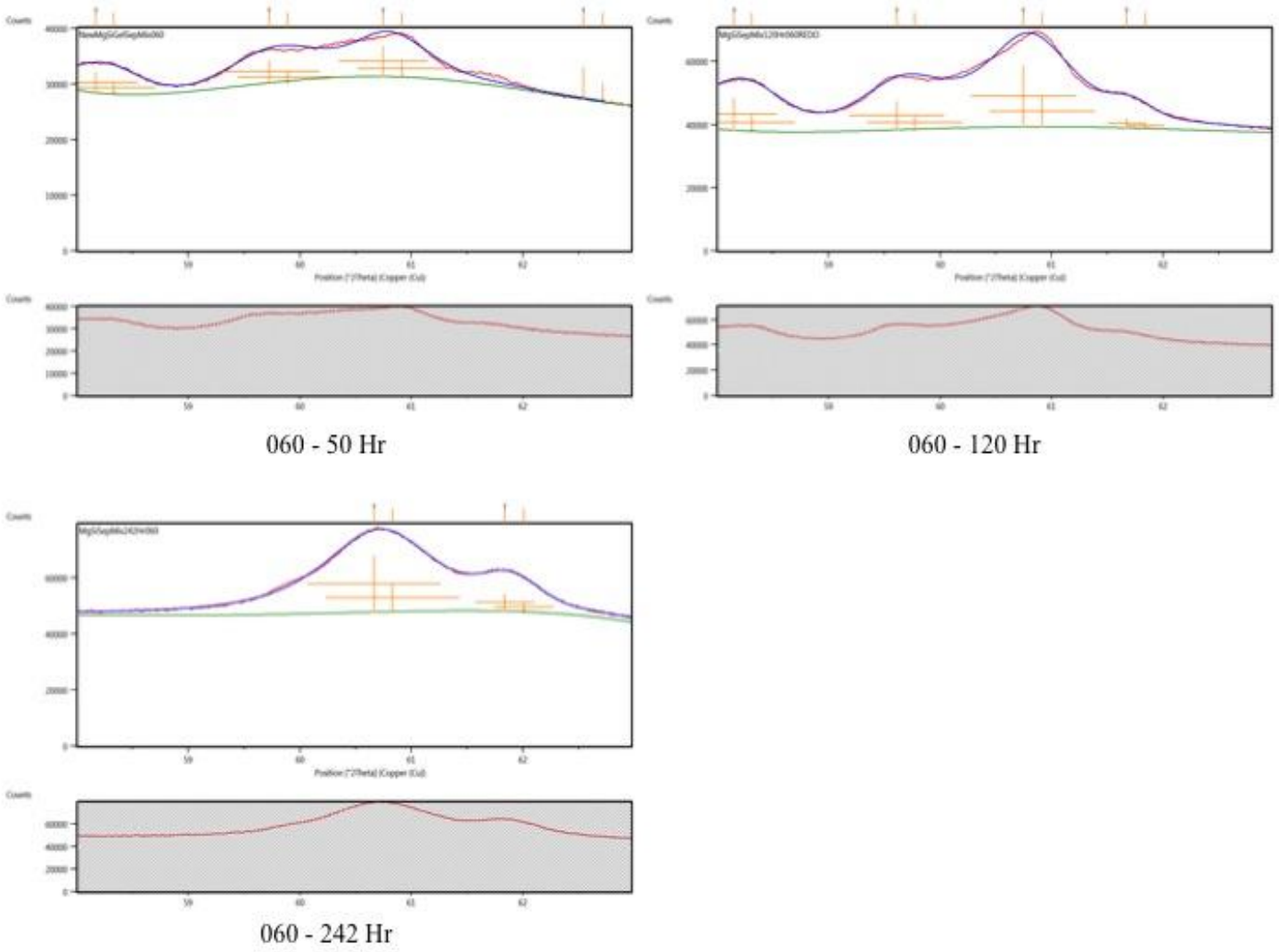

Figure 7.2.2.15: Individual Heated MgSiGel/ Sep-Sp-1 Mix 060 Peaks, showing Fit Profile used for crystallinity determination.

7.2.3 X-ray Diffraction of the Magnesium Silicate Gel Mixed with Na Montmorillonite (Swy-2)

The experiment was then repeated with the addition SWy-2 in place of Sep-Sp-1. The oriented pattern of the MgSiGel/Swy2 Mix produced two broad humps at 4.51 Å and 2.56 Å (Figure 7.2.3.1), and a new peak at ~1.526 Å was produced, contrasting with the original SWy-2 dioctahedral 060 peak (1.492 – 1.50 Å) (Figure 7.2.3.2). SWy-2 was then heated alone in 15 mL H_2O inside a Parr bomb for 50 hours and surprisingly the 001 peak expanded from 11.8 Å to 15 Å (Figure 7.2.3.3). This was repeated without H_2O outside of the Parr bomb and as expected the peak collapsed slightly to 9.6 Å. Normally heating SWy-2, collapses the 001 peak due to the removal of water from the interlayer between 2:1 groups. Expansion of the basal 001 peak inside the Parr bomb suggest that the water molecules in between the 2:1 groups are expanding when converted to gas molecules and therefore expanding the total crystallographic structure of the clay. This expansion and collapse only occurs in between groups and does not affect the octahedral layers, therefore the 060 peak (~1.492-1.50 Å) did not change (Figure 7.2.3.4). To show that this process was reversible and the re-hydration process is possible, SWy-2, SWy-2 Heated (Parr) and SWy-2 Heated (No Parr) were placed in glycol overnight and all three resulted in the expected expansion of the 001 peak to 16.8 Å (Figure 7.2.3.5).

The MgSiGel/SWy-2 Mix was then heated for the varying lengths of time (Figure 7.2.3.6) and results showed changes in both the 001 and 060 peaks. Additionally the 030 peaks' (2.9 – 3.1 Å) intensity collapsed and disappeared as heating time increased. When focusing on the 001 Peaks (Figure 7.2.3.7) the movement is slightly sporadic over time, beginning at 11.8 Å and then jumping to the 14 Å range, before slowly collapsing from 14.8 Å to 14.1 Å as time heated increased. The outlier lies in the 72-hour sample, which contrary to the rest of the samples expanded to 15.3 Å. As mentioned earlier, this expansion of the 001 peak suggests that the water

molecules between 2:1 layers are expanding and then are slowing squeezed out as time increases under pressure.

The 060 peaks, in Figure 7.2.3.8, indicate a shift in the octahedral layers of MgSiGel/ SWy-2 Mix. The original di-octahedral 060 peak, at 1.497 Å, collapsed to 1.489 Å after 25 hours of heating, and then expanded to a tri-octahedral peak at ~1.52 Å as time increased. Both peak height (cts) and area (cts*^{0}2Theta) increased, while FWHM (^{0}2Theta) decreased (Table 7.2.3.1 and Figure 7.2.3.9) indicating increases in crystallinity of theses newly formed tri-octahedral domains. The secondary quartz peak at 1.54 Å completely disappeared after 5 hours of heating. Changes in individual peak movements are shown in Figures 7.2.3.10 and 7.2.3.11.

Additionally one sample was run where the amount of MgSiGel present was doubled to ~0.157 g (Figure 7.2.3.12) and heated to 200° C for 50 hours. When comparing the oriented XRD from 5-70 degrees, there were no differences, but there was a change in the 060 peaks. The 2XMgSiGel/SWy-2 Mix resulted in an increased peak height (cts), and peak area (cts*^{0}2Theta) and decrease in FWHM (^{0}2Theta), indicating increasing in crystallinity. To help determine if a true tri-octahedral smectite was created MgSiGel/SWy-2Mix was glycolated and compared to SWy-2 in glycol (Figure 7.2.3.13). SWy-2 in glycol expands the basal 001 peak from 11.8 Å to 16.8 Å and the MgSiGel/SWy-2Mix in glycol is expanded further to 17.3 Å.

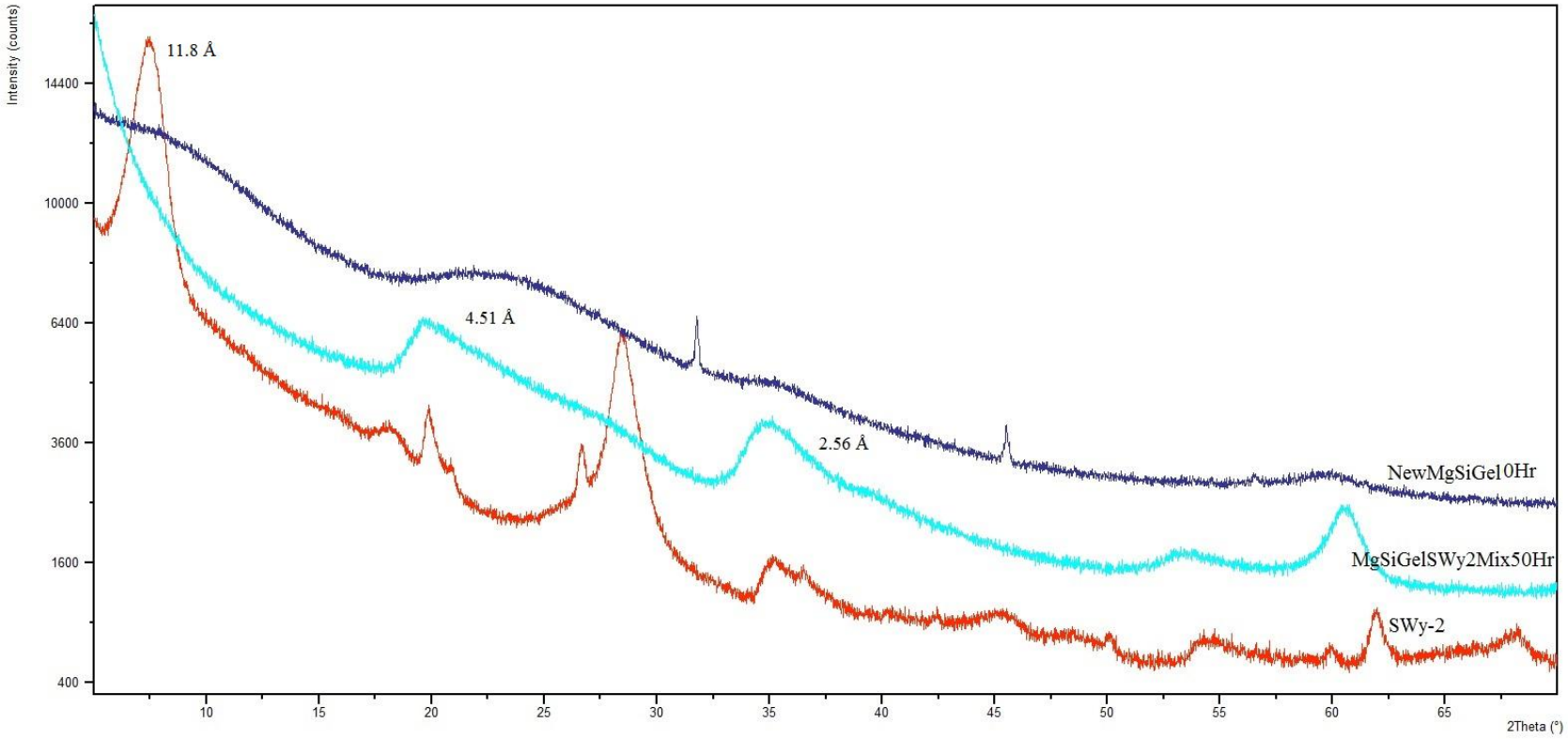

Figure 7.2.3.1: Diffractogram of Mg-Silicate Gel, SWy-2 and Mg-Silicate/SWy-2 Combined from 5-70 Degrees.

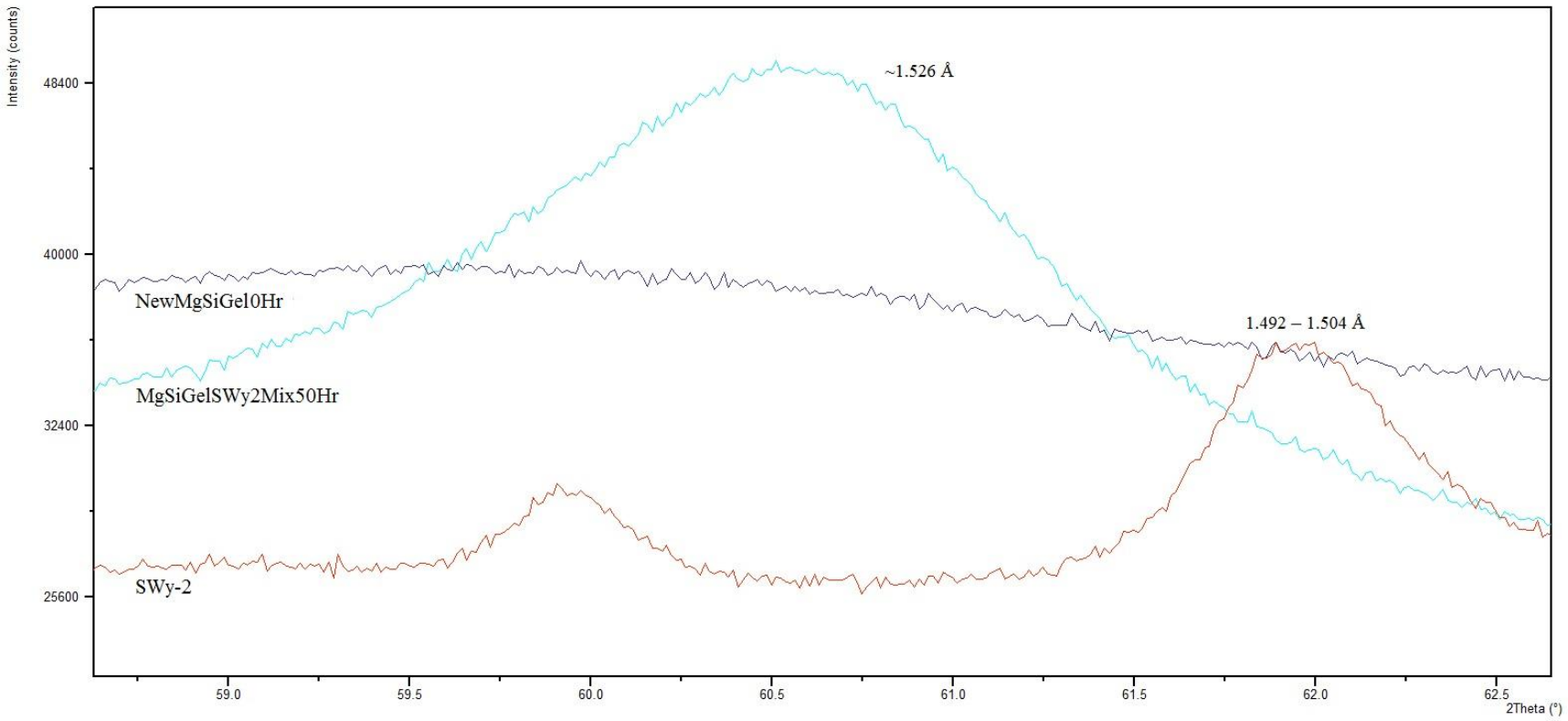

Figure 7.2.3.2: Diffractogram of Mg-Silicate Gel, SWy-2 and Mg-Silicate/SWy-2 Combined from 59-62 Degrees.

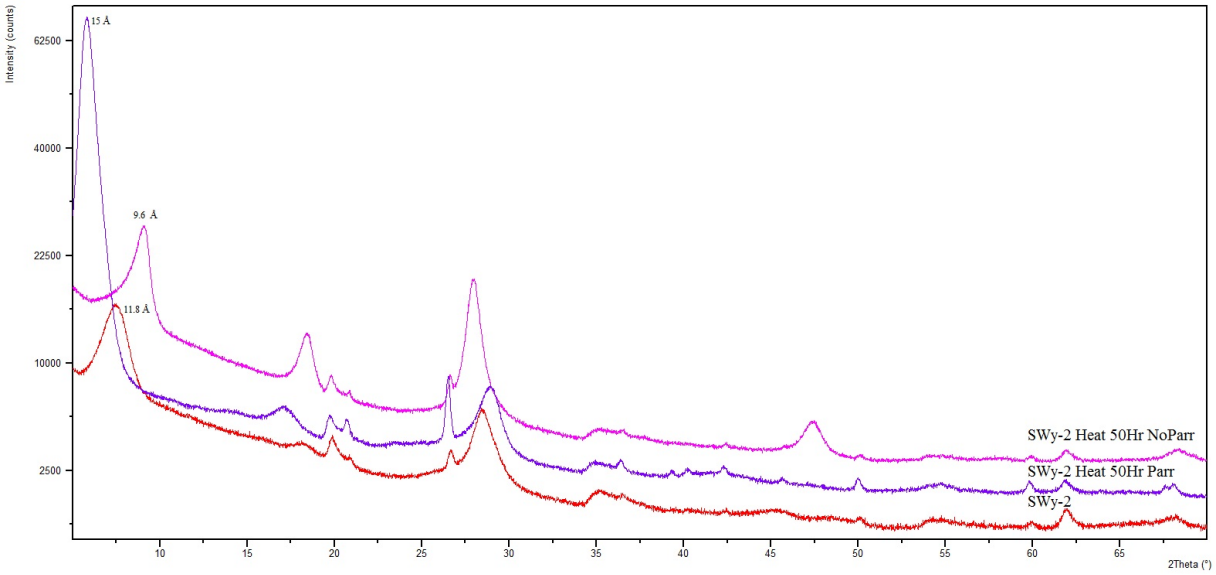

Figure 7.2.3.3: SWy-2 compared to SWy-2 Heated for 50 Hours at 200°C, 5-70 Degrees.

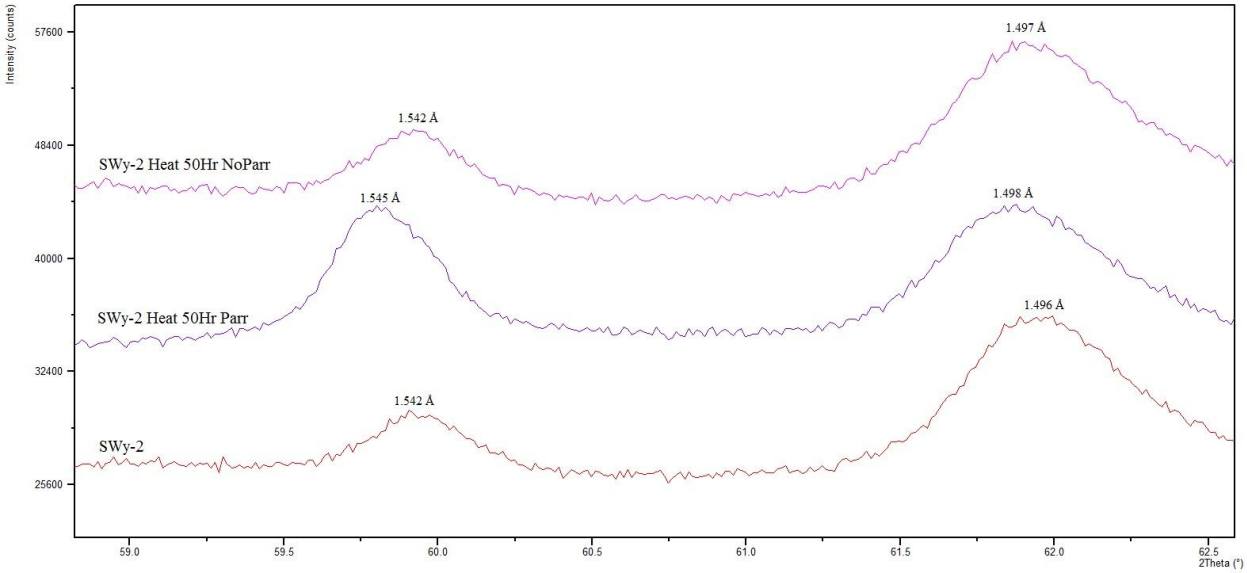

Figure 7.2.3.4: SWy-2 compared to SWy-2 Heated for 50 Hours at 200°C, Showing 060 Peaks.

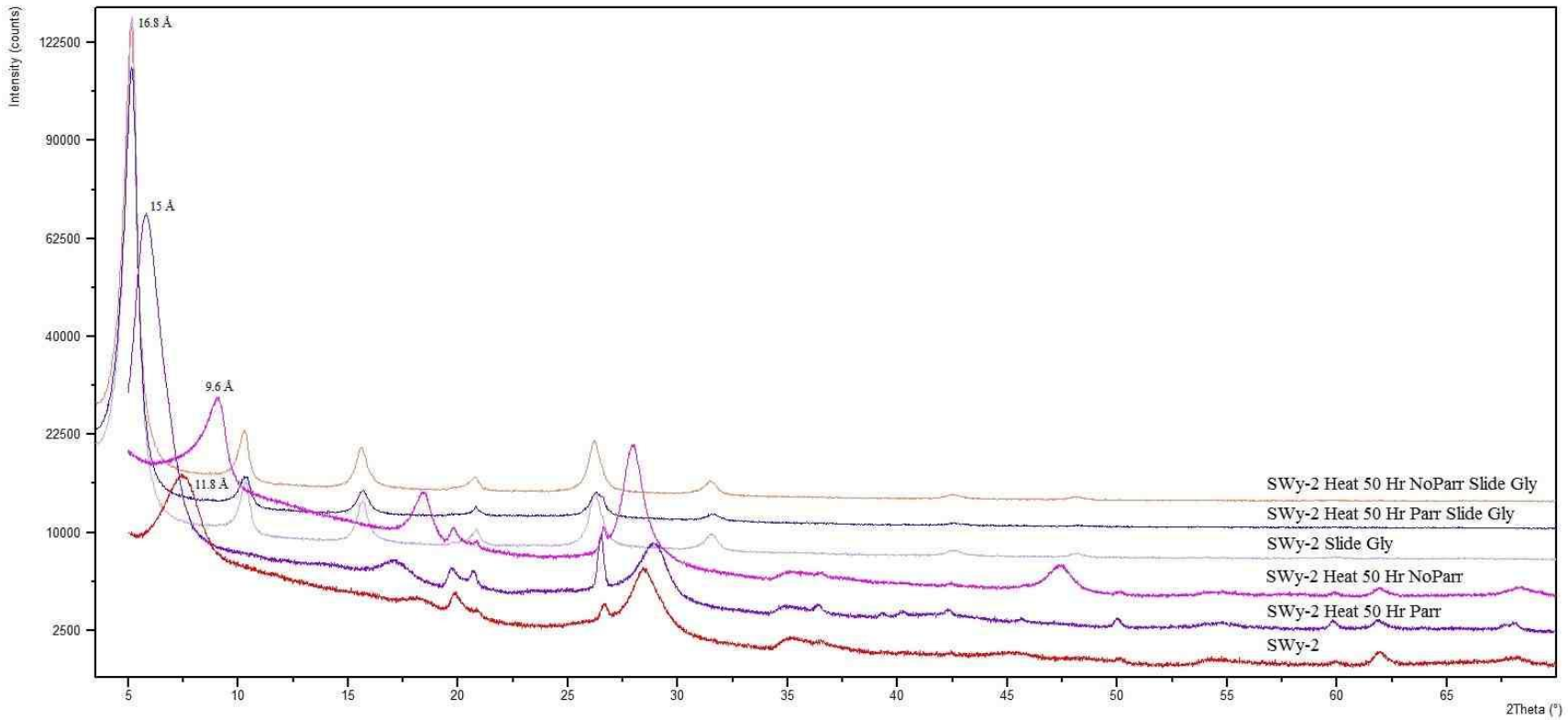

Figure 7.2.3.5: SWy-2 compared to SWy-2 Heated for 50 Hours at 200°C and Glycol slides, 5-70 Degrees.

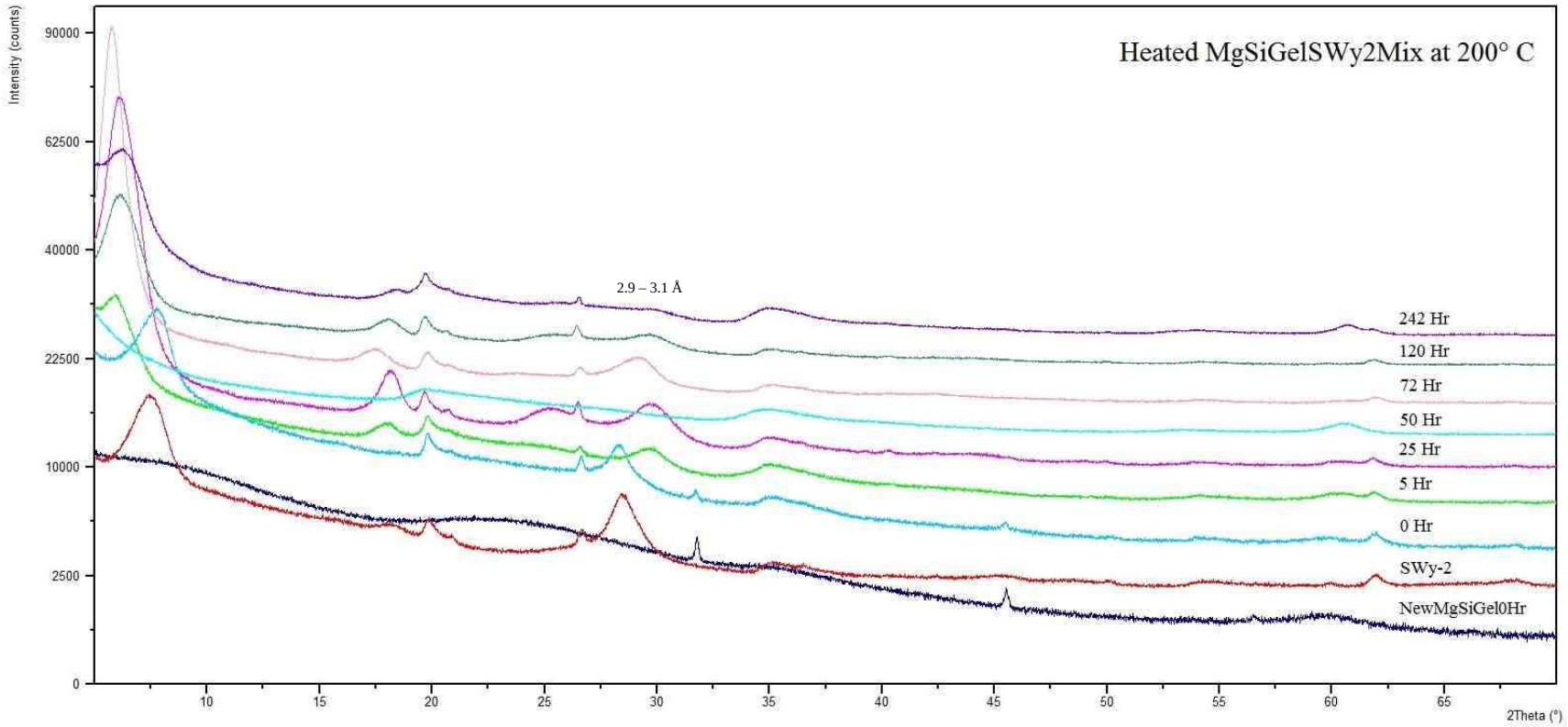

Figure 7.2.3.6: Diffractogram of Heated MgSiGel/ SWy-2 Mix at 200°C from 5-70 Degrees.

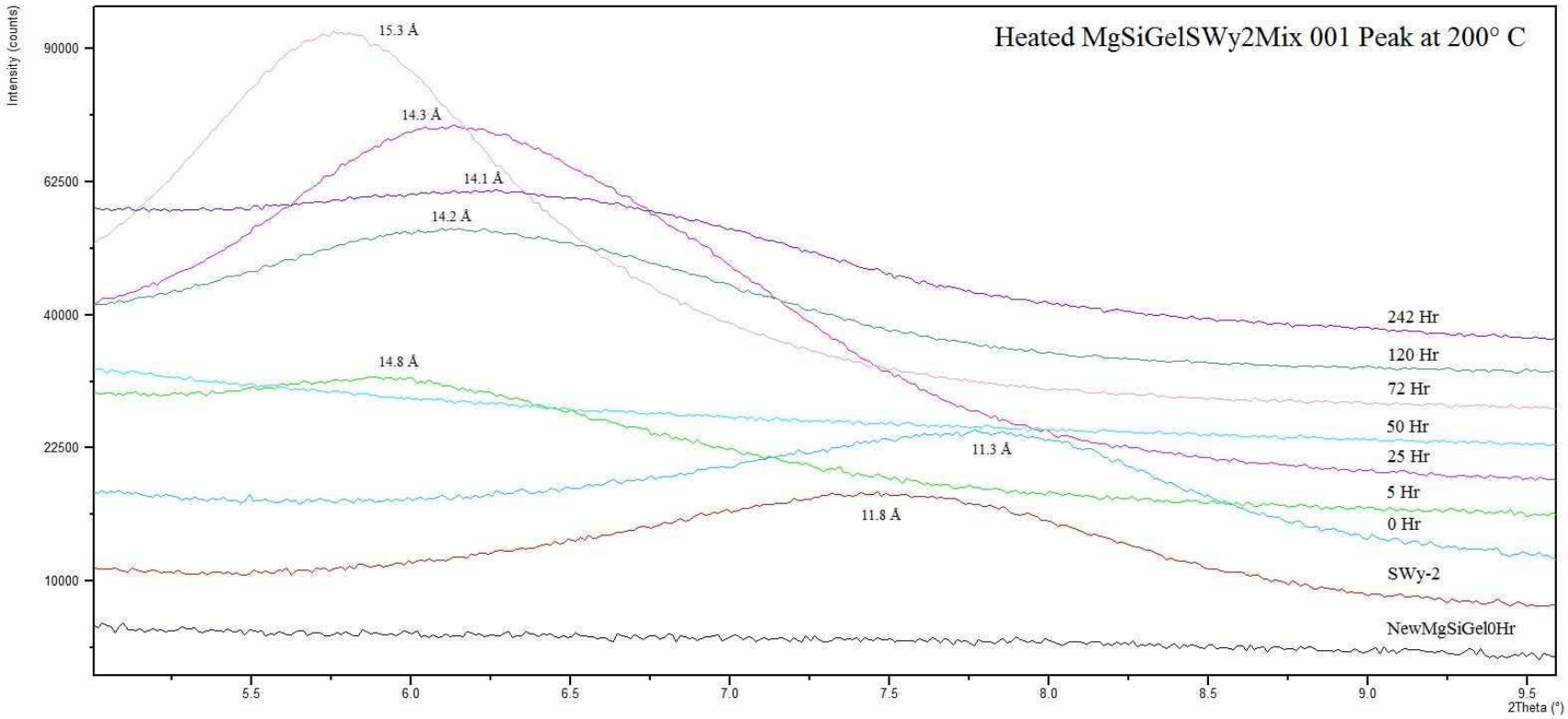

Figure 7.2.3.7: Diffractogram of Heated MgSiGel/ SWy-2 Mix at 200°C focusing on 001 Peak (5-9 degrees).

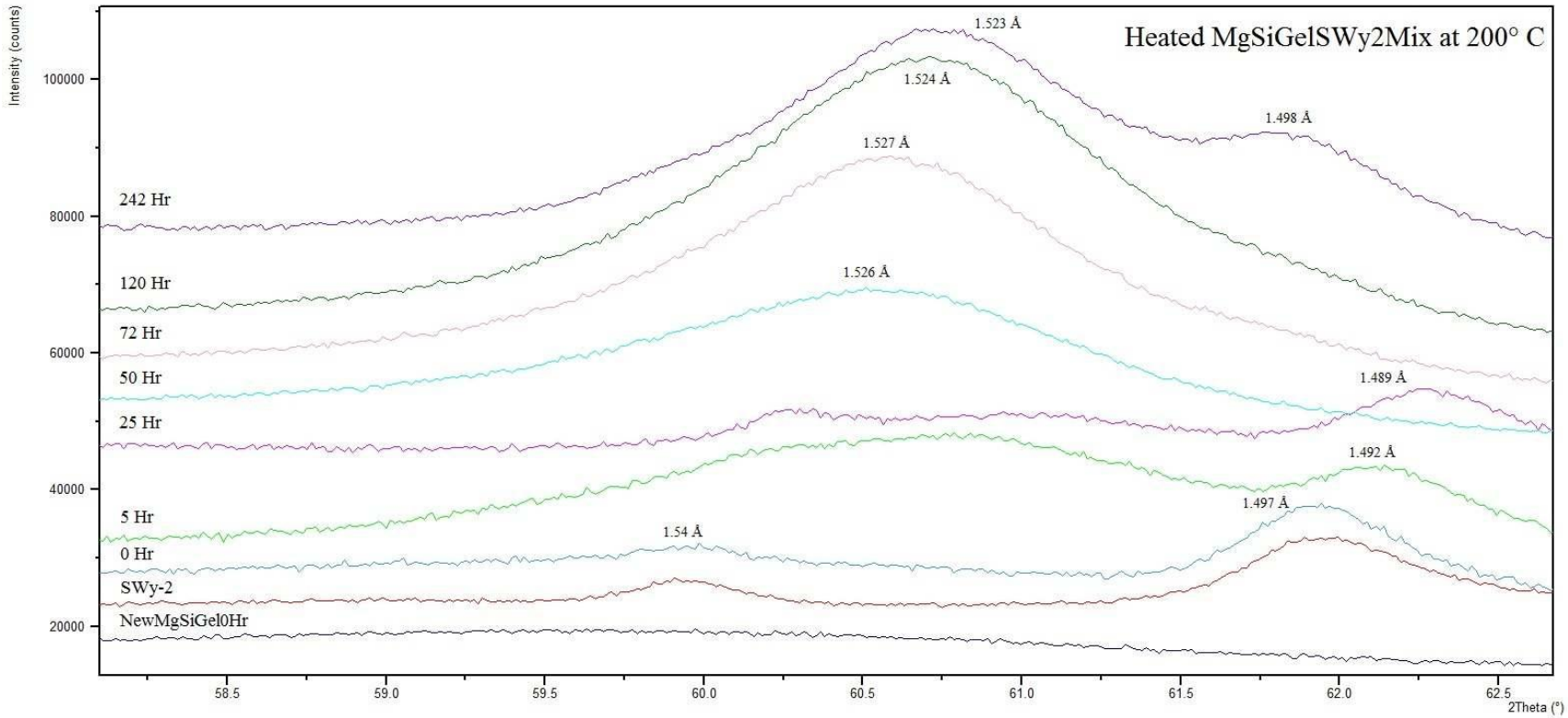

Figure 7.2.3.8: Diffractogram of Heated MgSiGel/ SWy-2 Mix at 200°C from 59-62 Degrees.

Table 7.2.3.1: Changes In MgSiGelSWy-2Mix 060 Peaks Over Time at 200°C.

Name	Time Heated at 200^{0}C (hrs)	Peak Height (cts)	FWHM (^{0}2Theta)	Area (cts*^{0}2Theta)	Peak d-spacing
Swy-2	0	7038.01	0.6047	5727.57	1.497 Å
MgSiGelSWy2Mix0Hr	0	7783.76	0.5504	4559.95	1.497 Å
MgSiGelSWy2Mix5Hr	5	3980.39	0.3876	1642.27	1.492 Å
MgSiGelSWy2Mix25Hr	25	5210.66	0.4697	2604.97	1.489 Å
MgSiGelSWy2Mix50Hr	50	13697.04	1.6433	32508.06	1.526 Å
MgSiGelSWy2Mix72Hr	72	22757.59	1.4147	50570.89	1.527 Å
MgSiGelSWy2Mix120Hr	120	27408.4	1.4697	62439.98	1.524 Å
MgSiGelSWy2Mix242Hr	242	16603.7	1.0336	26184.23	1.523 Å

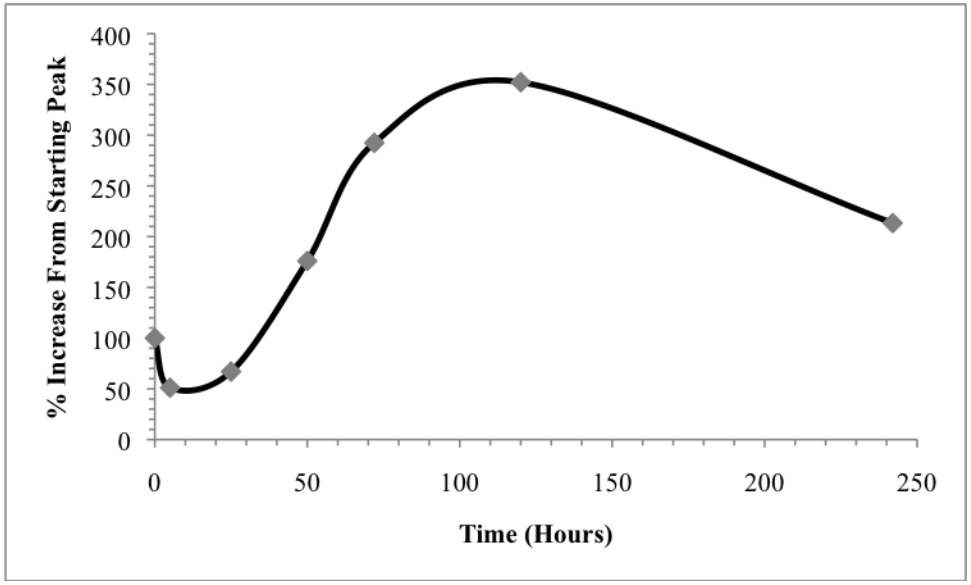

Figure 7.2.3.9: Percent Increase in 060 Peak Heights Over Time at 200°C.

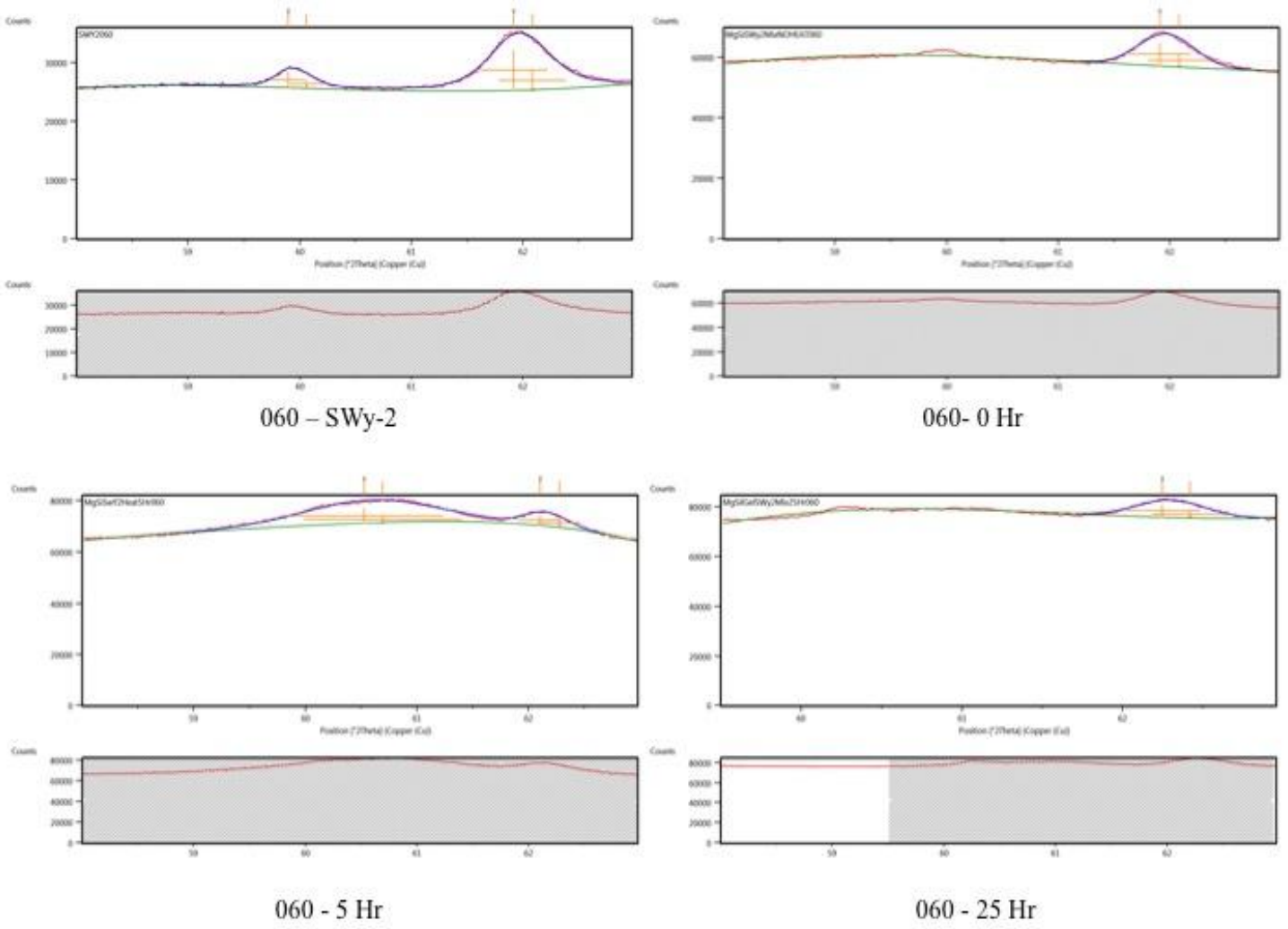

Figure 7.2.3.10: Individual Heated MgSiGelSWy-2Mix 060 Peaks, showing Fit Profile used for crystallinity determination.

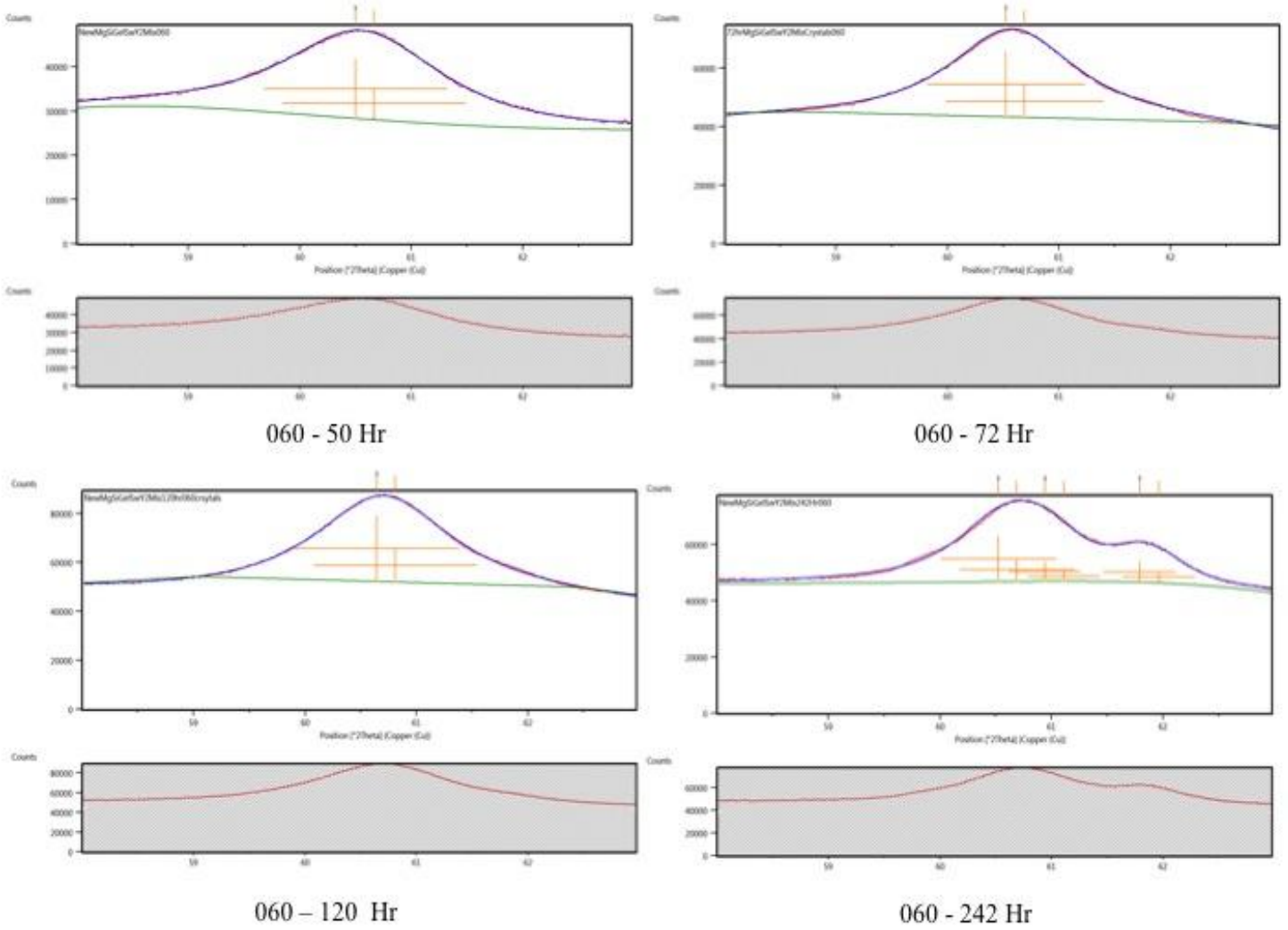

Figure 7.2.3.11: Individual Heated MgSiGelSWy-2Mix 060 Peaks, showing Fit Profile used for crystallinity determination.

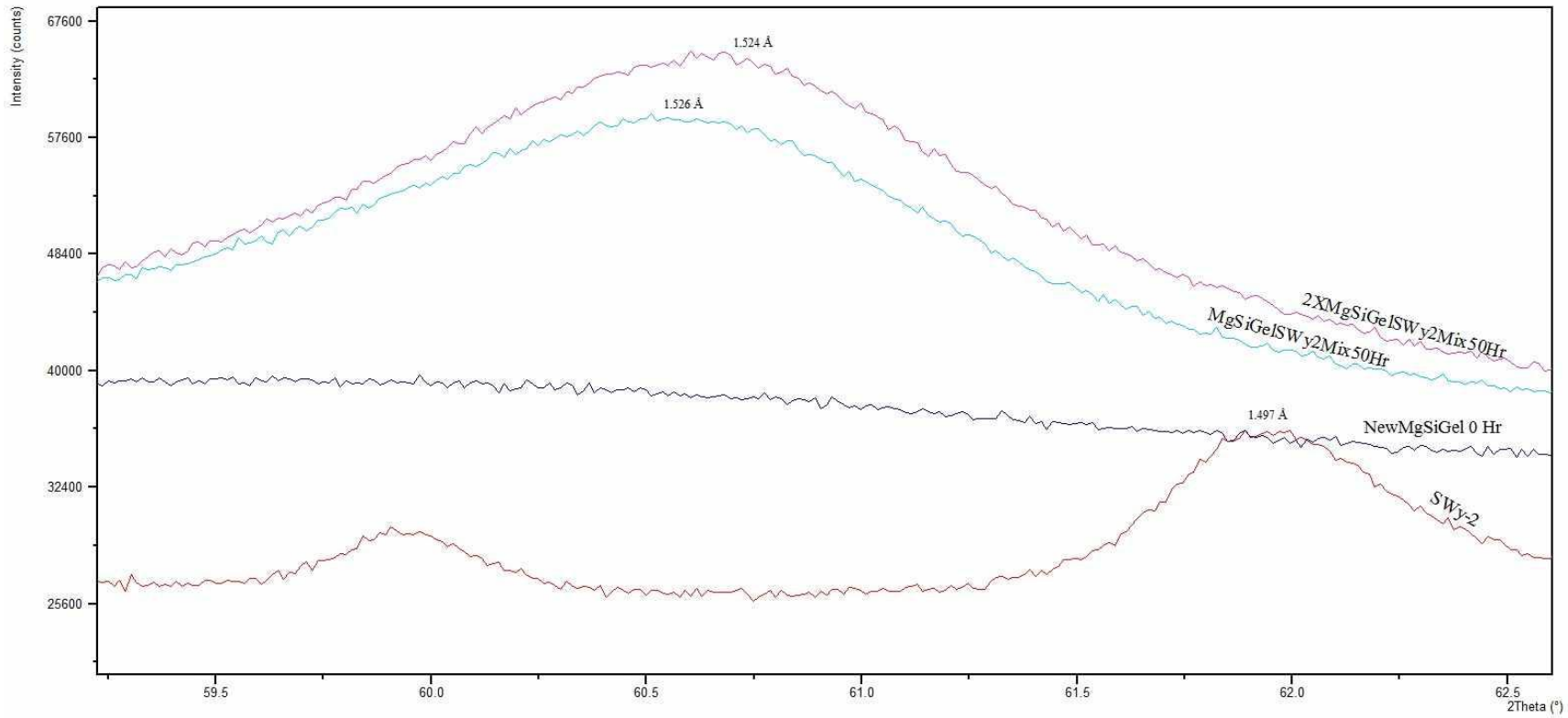

Figure 7.2.3.12: MgSiGel/SWy-2 Mix compared to 2X MgSiGel/SWy-2 Mix Heated for 50 Hours at 200°C, Showing 060 Peaks.

Table 7.2.3.2: Changes in 060 Peaks of MgSiGel/SWy-2 Mix compared to 2X MgSiGel/SWy-2 Mix.

Name	Time Heated at 200^{0}C (hrs)	Peak Height (cts)	FWHM (^{0}2Theta)	Area (cts*^{0}2Theta)	Peak d-spacing
MgSiGelSWy2Mix50Hr	50	13697.04	1.6433	32508.06	1.526 Å
2X MgSiGeSWy2Mix50Hr	50	16328.61	1.5388	38216.21	1.524 Å

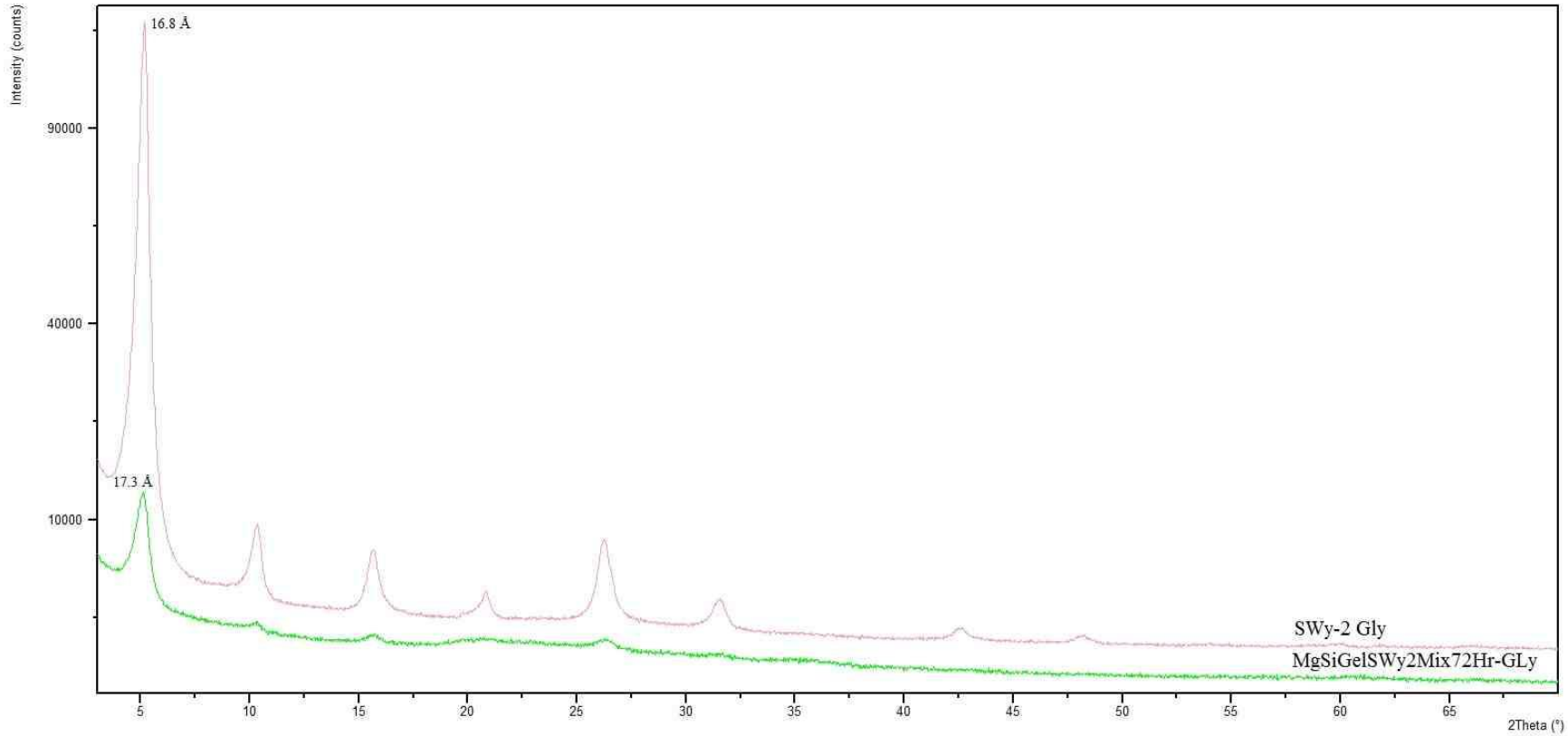

Figure 7.2.3.13: SWy-2 Glycol compared to MgSiGel/SWy-2 Mix Glycol Heated for 72 Hours at 200°C.

7.3 SEM and EDS

SEM showed an increase in Mg/Si ratio from Mg-Silicate Gel (Figure 7.3.1) to Mg-Silicate gel/Sep-sp-1 Mix (Figure 7.3.3). When examining Mg-Silicate gel/SWy-2 mix (Figure 7.3.5) the prescience of Al was only found as veins peaking through a possible Mg-silicate crust.

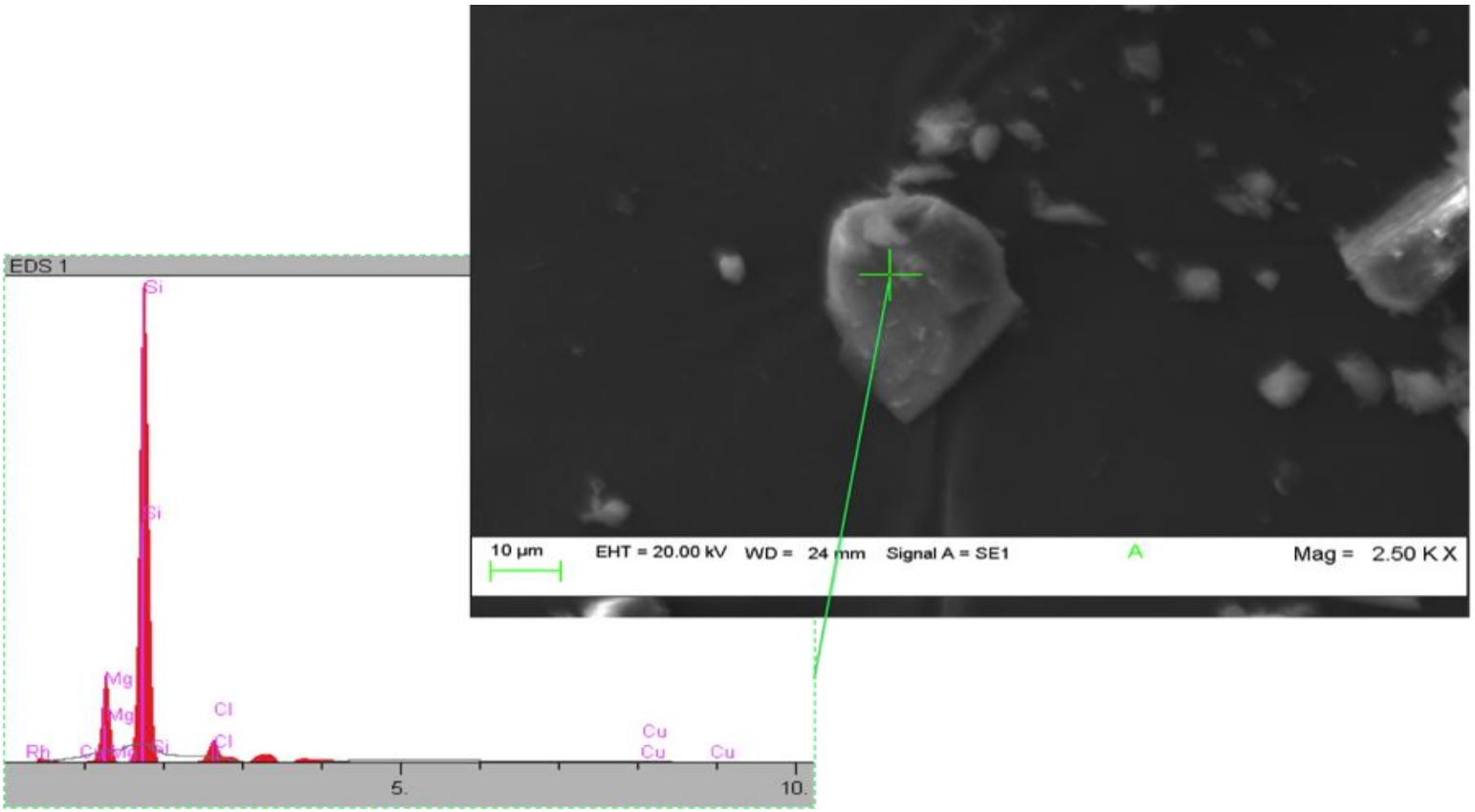

Figure 7.3.1: SEM Image of Mg-Silicate Gel with Corresponding EDS Results.

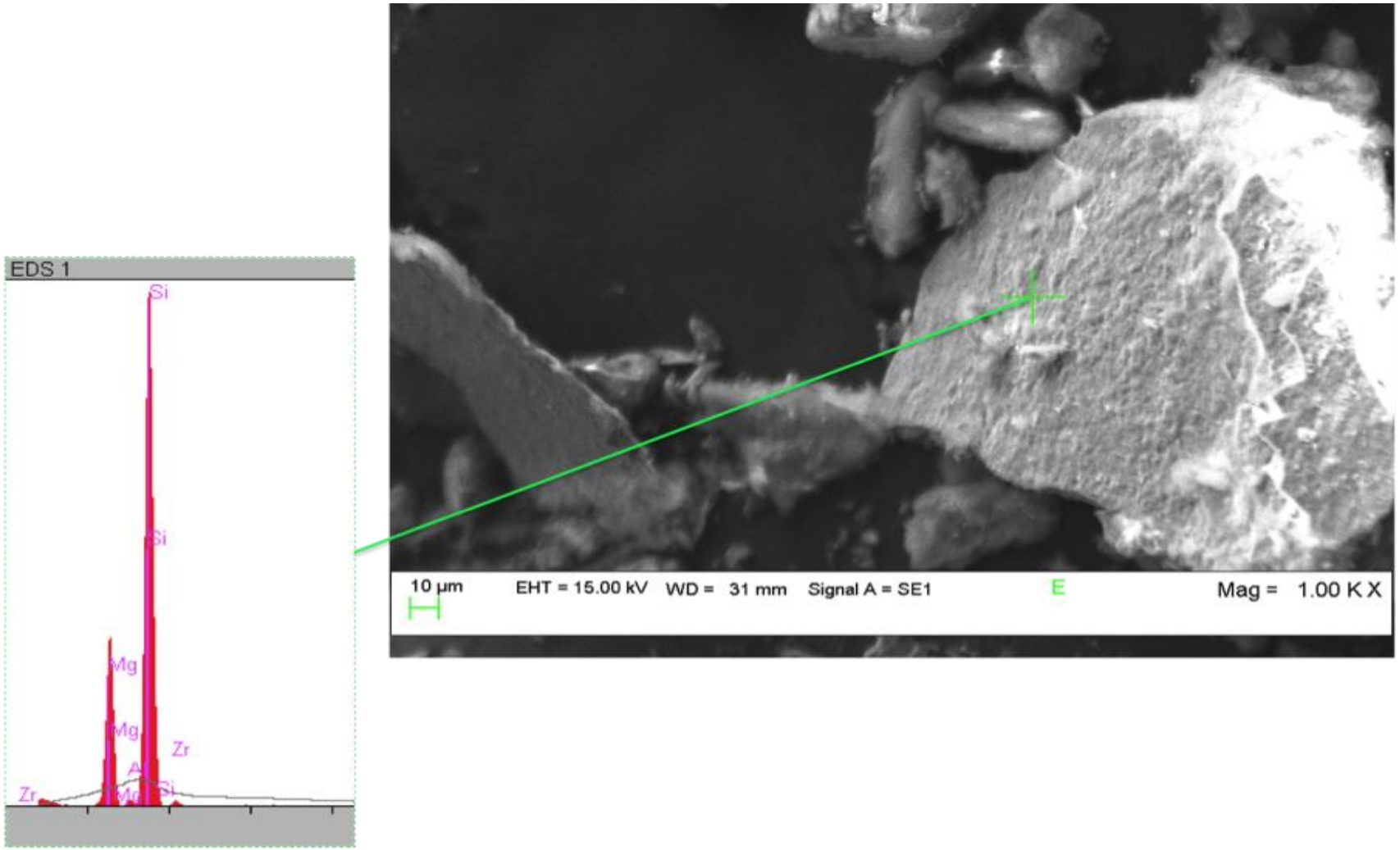

Figure 7.3.2: SEM Image of Sep-sp-1 with Corresponding EDS Results.

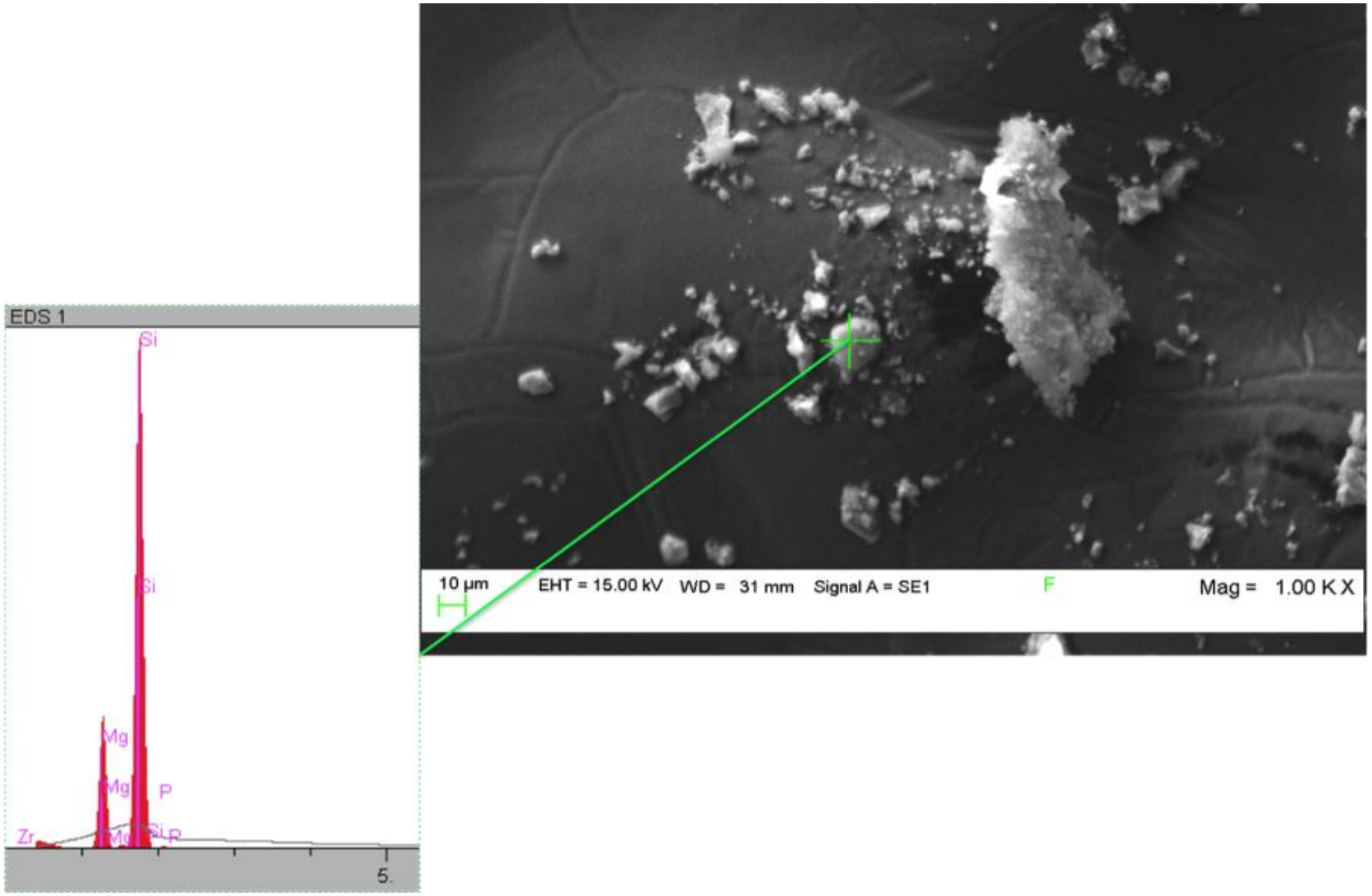

Figure 7.3.3: SEM Image of Mg-Silicate Gel/Sep-sp-1 Combination with Corresponding EDS Results.

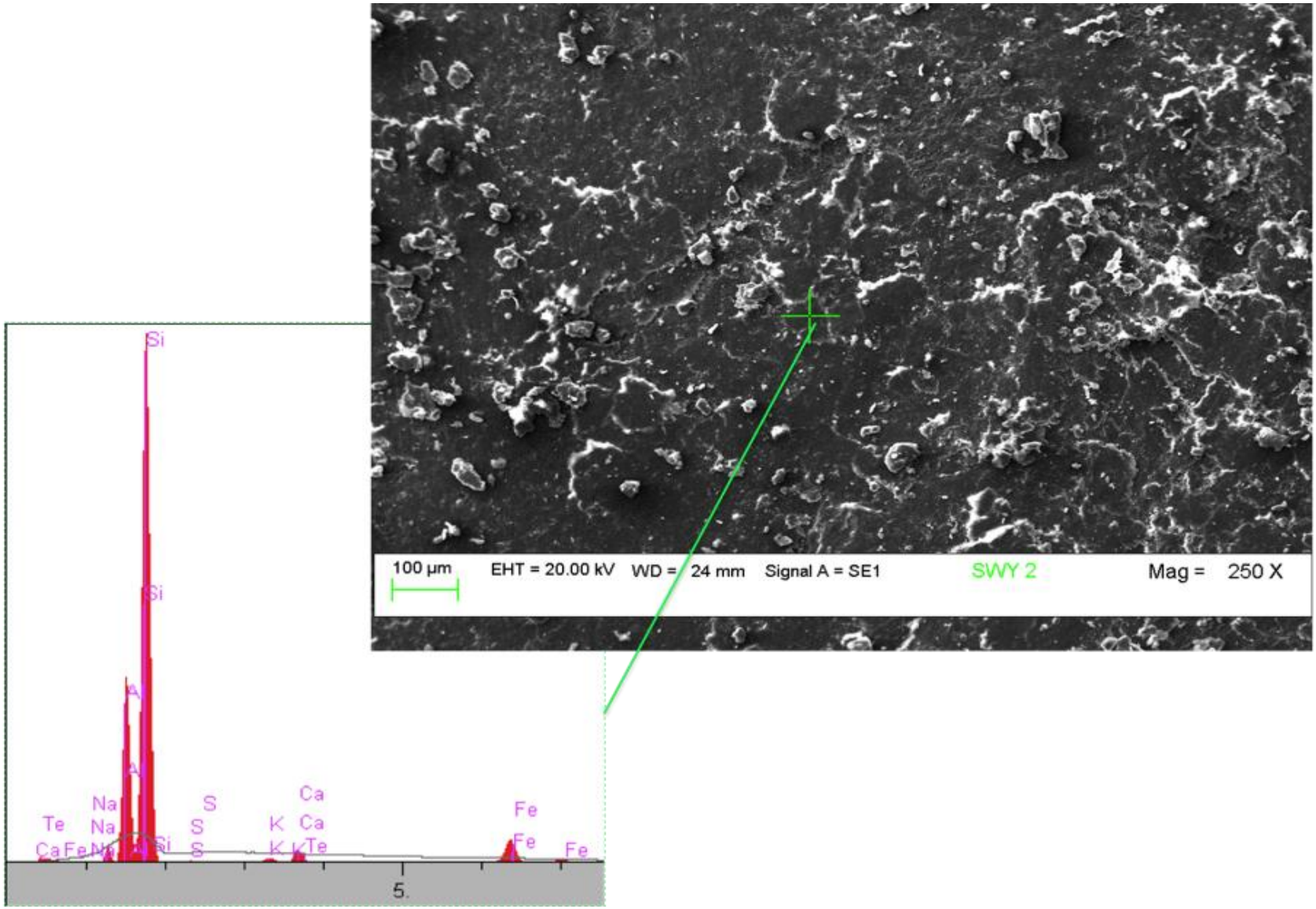

Figure 7.3.4: SEM Image of SWy-2 with Corresponding EDS Results.

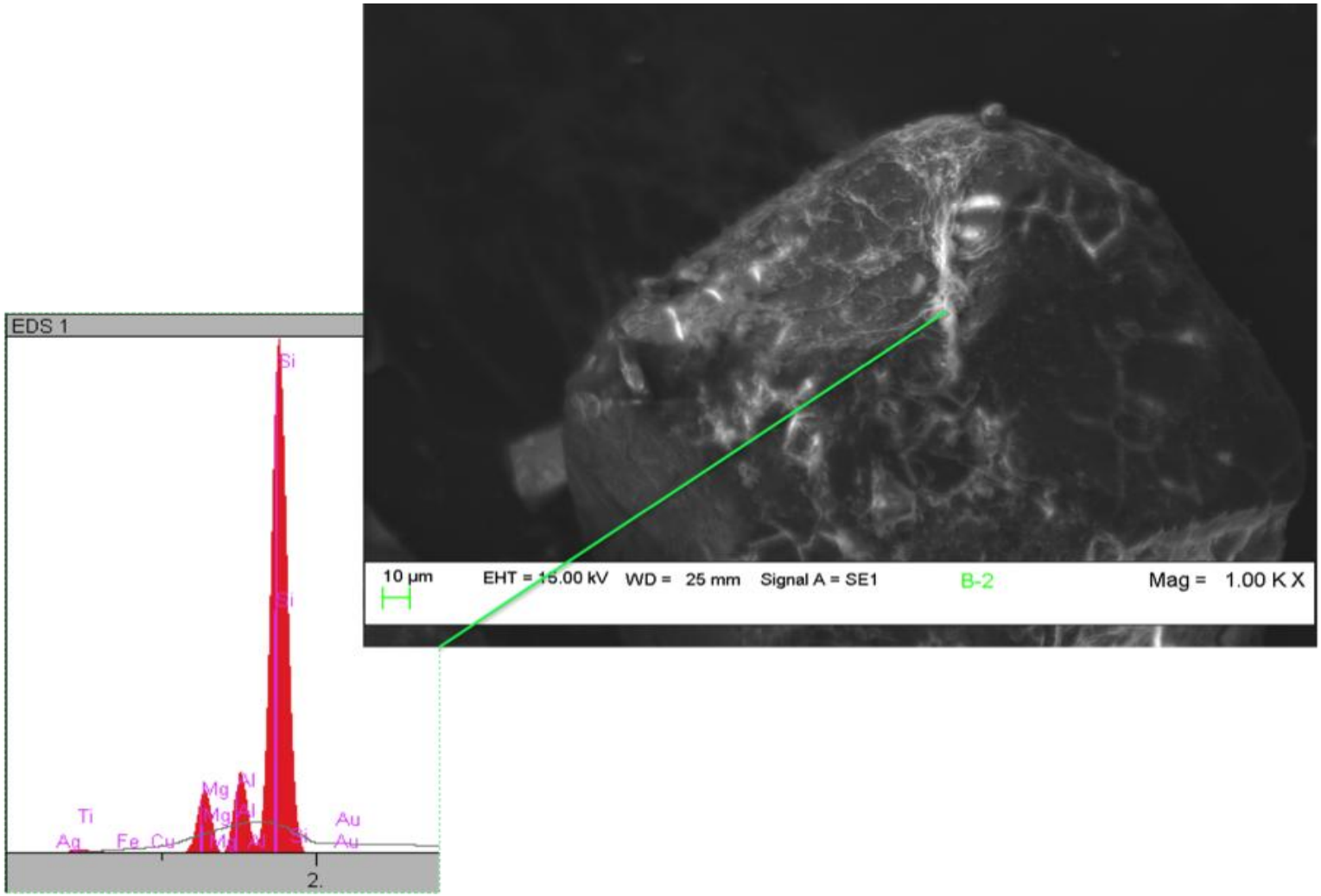

Figure 7.3.5: SEM Image of Mg-Silicate Gel/SWy-2 Combination with Corresponding EDS Results.

7.4 ICP-OES

ICP-OES analysis revealed that unheated new MgSiGel was composed of 5800 ppm (.5%) Mg and 8300 ppm (.8%) Si.

7.5 PHREEQC Modeling

Chemical composition of the Mg-Silicate gel in solution was used to complete modeling through the North Dakota State University Department of Geosciences WEB-PHREEQ Input Form for a Single Solution Using Simple Speciation and PHREEQC Database*. PHREEQC is used to simulate reactions and processes in laboratory experiments and natural waters.

Table 7.4.1: Description of the Solution.

pH	10.552
pe	0.000
Activity of Water	0.946
Ionic Strength	1.60
Mass of Water (kg)	1
Total alkalinity (eg/kg)	9.44×10^{-1}
Total Carbon (mol/kg)	0
Total CO_2 (mol/kg)	0
Temperature (C)	200
Electrical balance (eg)	3.88×10^{-15}
Percent error	0.00
Total H	1.12×10^{2}
Total O	56.4

Table 7.4.2: Saturation Indices for New MgSiGel.

Phase	Saturation Index	Log of Ion Activity Product (IAP)	Log of the equilibrium constant for the temperature of the water (KT)
Chalcedony	-0.75	-3.02	-2.27
Chrysotile	27.42	45.70	18.29
Sepiolite	12.52	25.38	12.86
Talc	30.85	39.69	8.83
Halite	-2.34	-0.51	1.83
Quartz	-0.66	-3.02	-2.36
SiO_2(a)	-1.22	-3.02	-1.80

* http://www.ndsu.nodak.edu/webphreeq/webphreeq-input.cgi

A description of the solution is provided in Table 7.4.1. Table 7.4.2 shows a few of the possible mineral phases present in the new MgSiGel after initial formation. Sepiolite (SI=12.52), Chrysotile ($Mg_3(Si_2O_5)(OH)_4$) (SI=27.42), and Talc ($Mg_3Si_4O_{10}(OH)_2$) (SI=30.85) are supersaturated while Chalcedony (SI=-0.75) and Quartz (SiO_2) (SI = -0.66) are slightly undersaturated. Table 7.4.3 shows all of the possible species in the solution, their concentration and activity. Mg concentrations were about 4.58×10^{-1} molar and there were two dissolved species present including $MgOH^+$ (4.57×10^{-1} molar) and Mg^{2+} (1.06×10^{-3} molar). Si concentrations were 5.97×10^{-2} molar and there were three species present; $H_3SiO_4^-$ (4.98×10^{-2} molar), $H_2SiO_4^{-2}$ (9.32×10^{-3} molar) and H_4SiO_4 (5.91×10^{-4} molar).

Table 7.4.3: Distribution of Species for New MgSiGel.

Species		Molarity	Activity
	OH^-	4.19×10^{-1}	1.69×10^{-1}
	H^+	4.44×10^{-11}	2.81×10^{-11}
	H_2O	5.55×10^{1}	9.46×10^{-1}
Cl		1.10 x 10	
	Cl^-	1.10 x 10	4.72×10^{-1}
H		2.57×10^{-25}	
	H_2	1.29×10^{-25}	1.86×10^{-25}
Mg		4.58×10^{-1}	
	$MgOH^+$	4.57×10^{-1}	3.94×10^{-1}
	Mg^{2+}	1.06×10^{-3}	1.53×10^{-4}
Na		1.13 x 10	
	Na^+	1.13 x 10	6.50×10^{-1}
	$NaOH$	1.01×10^{-4}	1.45×10^{-4}
O		5.77×10^{-8}	
	O_2	2.88×10^{-8}	4.17×10^{-8}
Si		5.97×10^{-2}	
	$H_3SiO_4^-$	4.98×10^{-2}	4.30×10^{-2}
	$H_2SiO_4^{-2}$	9.32×10^{-3}	5.19×10^{-3}
	H_4SiO_4	5.91×10^{-4}	8.55×10^{-4}

8 DISCUSSION PART II

XRF data revealed that the new Mg-Silicate gel was composed of 77.58 wt% SiO_2 and 20.04 wt % MgO. The MgO/SiO_2 ratio of new Mg-Silicate gel (0.41) is slightly lower than the Sepiolite Standard (Sep-sp-1) at 0.65. Comparison (Table 8.1 and Figure 8.1) to additional natural and synthetic sepiolite reveal that both our new Mg-silicate gel and previous Pre-Clay powder have slightly lower MgO/SiO_2 ratios than any natural or synthetic sepiolite. Although we did create a Mg-Silicate, this ratio indicates that the creation of sepiolite did not fully occur. Due to sample size, XRF was not preformed after hydrothermal crystallization of the new Mg-Silicate Gel, which may have affected this ratio. The MgO/SiO_2 ratio of SWy-2 (Table 7.1.1) is extremely low (0.07) and further testing would need to be done to examine the chemical make-up of both NewMgSiGel/Sep-Sp-1 Mix and NewMgSiGel/SWy-2 Mix.

Table 8.1: Chemical Analysis of NewMgSiGel Compared with Natural and Synthetic Sepiolite.*

	Natural Sepiolite, Mid-Atlantic Ridge (Hathaway and Sachs, 1965)	Natural Sepiolite, Little Cottonwood, Utah (Nagy and Bradley, 1955)	Synthetic Sepiolite, (Wollast et al., 1968)	Pre-Clay Powder	Sep-Sp-1	New MgSiGel
SiO_2	45.8	53.0	47.6	67.6	68.1	77.6
MgO	23.8	22.5	20.0	26.2	29.5	20.0
MgO/SiO_2	0.6	0.6	0.7	0.6	0.7	0.4

* Adapted from Wollast et al (1968)

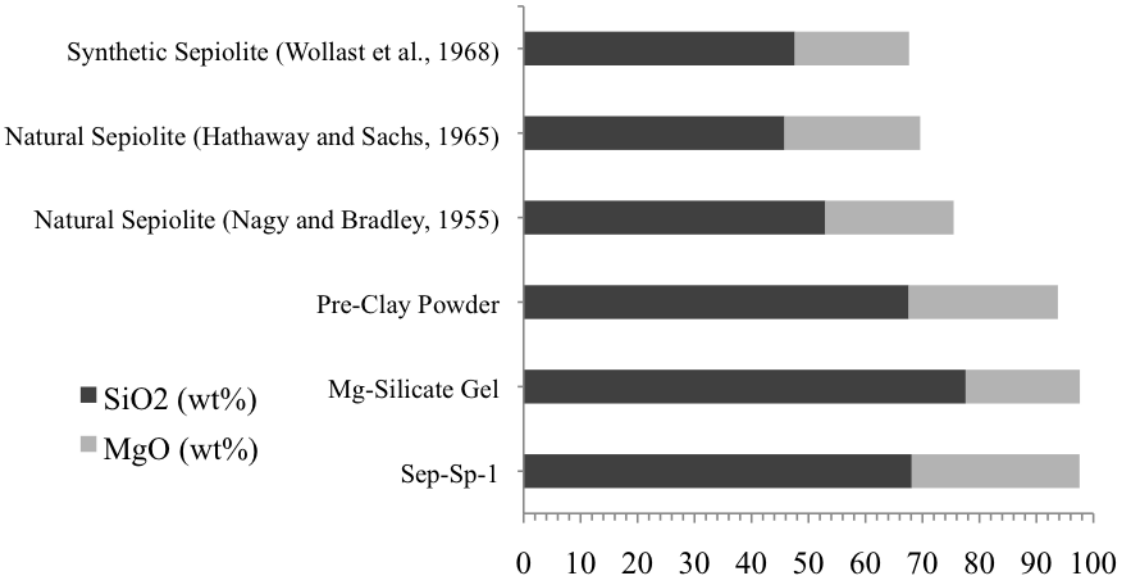

Figure 8.1: Major Elemental Composition of NewMgSiGel Compared with Natural and Synthetic Sepiolite.

PHREEQC modeling exposed that the New Mg-Silicate Gel was supersaturated with respect to Sepiolite, Chrysotile, and Talc phases. Although Talc has the largest SI value, it is it the least likely phase to occur due to instability of formation in the conditions provided (Bricker et al., 1973). XRD analysis of the New Mg-Silicate Gel revealed that none of these phases completely formed. The Mg-silicate created has more similarities to Chrysotile than to Sepiolite.

Before heating, the Mg-Silicate Gel produced an X-ray amorphous material with no distinct peaks. After heating the Mg-Silicate Gel, three peaks formed at ~4.5 Å, 2.5 Å, and 1.5 Å (Figure 7.2.1.3). Chrysotile has a 060 peak at 1.54 Å and 062 peak at 1.50 Å, which is the nearest matching 060 peak to the Mg-Silicate Gel (~1.52 – 1.53 Å). As time heated increased, all peaks shifted to the right and peak heights increased (Figures 7.2.1.3 and 7.2.1.5). This increase in intensity and sharpening of the peaks reflect an increase in crystallinity of the solid as a result of the conditions inside the Parr bomb (Bricker et al., 1973). Crystallinity refers to the degree of structural order and arrangement of atoms or molecules in a solid. Increases in the 060 peaks indicate increases in the order of the octahedral layer spacing of atoms. SEM imaging (Figure

7.3.1) of the Mg-Silicate Gel revealed angular mounds of Mg-Silicate unlike the easily identifiable fibrous morphology of sepiolite (Dixon and Weed, 1989).

After the Mg-Silicate gel was seeded with Sep-Sp-1 and subjected to hydrothermal conditions for 50 hours, the precipitate was similar to Sep-Sp-1 by oriented XRD (Figure 7.2.2.1) but a collapse of the 060 peak was observed from 1.549 Å to 1.52 Å (Figure 7.2.2.2). When varying the length of time heated (Figure 7.2.2.7) there were no key differences in oriented XRD from 10 – 55 degrees, but changes in the 011 peaks (Figure 7.2.2.8) and 060 peaks (Figure 7.2.2.11) occurred. Structural changes that occurred due to heating Sepiolite, decreased the intensity of the principle 011 XRD peak at 12 Å (Brigatti et al., 2006) but normally result in new reflections at 10 Å, which did not occur in this case. An initial loss of H_2O caused this decrease in height, as adsorbed and zeolitic H_2O are lost before coordinated H_2O. The higher thermal stability of sepiolite is due to its trioctahedral nature (Dixon and Weed, 1989). Contrasting the 011 peaks, the trioctahedral 060 peaks (Figure 7.2.2.12) expanded over time and became more crystalline.

Dixon and Weed (1989) discuss that although Sepiolite is formed in a wide spectrum of environments and this diversity might suggest a wide range of environmental conditions favored for formation, laboratory synthesis has encountered difficulties. Equilibrium studies indicate requirements for sepiolite stability, and while these can be met in nature they are not considered common. Many deposits were formed long ago and do not reflect the current environmental conditions. Although this experiment was modeled after Muzutani et al. (1991) successfully creation of sepiolite, this experiment did not fully form sepiolite. The formation under Muzitani's conditions was determined primarily by the hydrothermal stability of sepiolite itself (Caarrado et al. 2006), and the instability of these minerals in humid and wet environments indicates that they favor dry or semi-arid environments (Galan, 2006).

The final stage of the experiment repeated the hydrothermal synthesis of the New Mg-Silicate gel with the addition of SWy-2 instead of Sep-Sp-1. Oriented XRD of MgSiGel/SWy-2 Mix heated for 50 hours produced a product different than oriented SWy-2 with two broad humps at 4.51 Å and 2.56 Å (Figure 7.2.3.1), and a new peak at ~1.526 Å, contrasting with the original SWy-2 dioctahedral 060 peak (1.492 – 1.50 Å) (Figure 7.2.3.2). The MgSiGel/SWy-2 Mix was then heated for varying lengths of time (Figure 7.2.3.6) and results showed changes in both the 001 and 060 peaks. Much like the other hydrous minerals, SWy-2 will lose H_2O when heated in low humidity situations (Dixon and Weed, 1989). The minerals 001 peak shows this loss of water. The humidity inside the contained Parr Bomb system is extremely high, due to the water turning into vapor during heating, because of this evaporation, the 001 peak movement is sporadic but overall intensity decreases as time increases.

Brindley and Brown (1980) discuss how many studies have shown that sorption of water into the interlayer is determined by both size and charge of the saturated cation. Early studies of smectite showed the continual changes in 001 peaks due to water loss/gain, but it is now known that variations occur due to random interstratifications of hydrates. The basal spacing for smectites saturated with Mg^{+2} is 15 Å (Schultz, 1960), which is achieved in our 72-hour sample and then the spacing collapsed as time increases and the H_2O in the interlayer is removed. The sporadic movement of the 001 peak may also be due to the use of randomly oriented mounts instead of preferred oriented slides. Humidity changes of the local environment throughout sampling can affect the movement of the interlayer spacing.

As described by Dixon and Weed (1989) dioctahedral and trioctahedral smectites can be differentiated by examining 060 peaks in randomly oriented samples (Figure 7.2.3.8). Dioctahedral clays are common in soils and formed as a result of weathering, while trioctahedral clays are inherited from parent materials and rarely found in soils. The di-octahedral 060 peak, at 1.497 Å,

collapsed to 1.489 Å after 25 hours of heating, and then expanded to a more crystalline tri-octahedral peak at ~1.52 Å as time increased. This peak shift suggested that we synthesized trioctahedral domains in a smectite structure and physically altered the chemical make-up of the clay, by increasing the Mg content of the sample and substituting cations into the octahedral layer (Brigatti et al., 2006).

Glycolation of the MgSilicateGel/SWy-2 Mix (Figure 7.2.3.13) revealed an expansion of the basal 001 peak that is similar to Saponite (17 Å). This correlates to Saponite's 060 peak (1.52 Å) and the experimental product's final 060 peak (1.52 Å). Indicating that Saponite was formed by the neogenesis of the original detrital clay in high Mg-silica concentrations. Saponite generally forms in poorly drained wetland, highly evaporative locations and/or hydrothermal fracture zones, but is usually dependent upon a high Mg parent rock (such as Serpentinite) (Dixon and Weed, 1989).

This shows that absence of Al-rich detritus in Neogene paleolakes is most likely due to the neo-foramtion of Al-Mg-Silicates, such as Saponite, and pure Mg-silicates with no smectite structure present. By applying the geochemistry of these clays to paleoenvironmental reconstructions of the lacustrine basins we can conclude that region was hydrothermally active with poor drainage (implying high humidity levels) and highly concentrated evaporate brine levels.

8.1 Conclusions and Implications

By subjecting Sepiolite and Smectite to high Mg-Silica situations we have demonstrated that crystallinity changes will occur in the octahedral layers of the clays. As heating time increases Sepiolite octahedral layers become more crystalline while collapsing in size and Smectite layers become more crystalline while expanding into tri-octhedral domains. Principle peaks change as well due to heating times and water loss. Sepiolite's 011 peak decrease in intentisity as basal layers expand due to increases in heating time, while Smectite's 001 peak decreases in both intensity and layer size. The instability of Sep-Sp-1 in humid environments indicates the favorability of dry semi-arid environments for formation. When the Mg-Silicate gel was seeded with SWy-2 a tri-octahedral Mg-smectite (Saponite) was formed indicating that Al-rich smectites do indeed aid in the creation of Mg-silicates. Therefore based off of this experiment Al-rich smectitces, saturated in Mg-silicate waters, will form Al-Mg-silicate clay minerals. Neogene paleoenvironmental reconstruction of the lacustine basins implies a hydrothermally active region with poor drainage and high evaporite levels.

8.2 Future Work

To improve the research completed in this study, more extensive XRF and ICP, as well as Transmission Electron Microscopy (TEM) data should be taken. For the pilot study, it would be important to determine where the Mg in the system went and how the seawater affects SWy-2 alone without the Mg-Silicate Gel. This would better determine how to proceed with the experiment without starting over. For the main experiment (Part II) a full suite of ICP-MS data needs to be collected to accurately assess what elements are moving in the clay system, informing the researcher when the system stabilized. TEM images would allow for examination of the octahedral layers of the products, and help determine exactly where the Mg is substituting into the clay. Ad-

ditional XRF data could also be collected to determine elemental analysis. Samples should be run for additional times to track peak changes until equilibrium, and the amounts of Mg-Silicate gel present should be altered to better understand how the gel is affecting the system.

REFERENCES

Abtahi, A. 1985. Synthesis of sepiolite at room temperature from silica and magnesium chloride solution. *Clay Minerals*, 20, p. 521 – 523.

Banfield, J.F., Jones, B.F., and Veblen, D.R. 1991. An AEM-TEM study of weathering and diagenesis, Abert Lake, Oregon: I, weathering reactions in the volcanics. *Geochimica et Cosmochimica Acta*, **55**, p. 2795 – 2810.

Bergaya, F., and Lagaly, G. 2006. General Introduction: Clays, Clay Minerals and Clay Science. *Handbook of Clay Science*, Elsevier Ltd: **1**, p. 1-18.

Billets, S. 2006. XRF Technologies for Measuring Trace Elements in Soil and Sediment: *EPA Innovative Technology Verification Report.*

Bozzola, J.J. and Russell, L.D. 1998. Electron Microscopy: Principles and Techniques for Biolo gists. *Jones and Bartlett Publishers.* 2 Ed.

Bragg, W.L. 1913. The diffraction of short electromagnetic waves by a crystal. *Proceeding of the Cambridge Philosophical Society,* **17**, p. 43-57.

Bricker, O.P., Nesbitt, H.W. and Gunter, W.D. 1973. The Stability of Talc. *American Mineralogist,* **58,** p. 64 – 72.

Brigatti, M.F., Galan, E. and Theng, B.K.G. 2006. Structures and Mineralogy of Clay Minerals. *Handbook of Clay Science* Elsevier Ltd: **1**, p. 19-86.

Brindley, G.W. and Brown, G. (ed.) 1980. Crystal Structures of Clay Minerals and Their X-ray Identifica tion. *Mineralogical Society,* **5**

Calvo, J.P., Blanc-Valleron M.M., Rodrigues-Arandia, J.P., Rouchy, J.M., and Sanz, M.E. 1999. Authigenic clay minerals in continental evaporite environments. 129-151. Special Publication **27**, International Association of Sedimentologists.

Carrado, K.A., Decarreau, A., Petit, S., Bergayga, F. and Lagaly, G. 2006. Synthetic Clay Miner als and Purification of Natural Clays. *Handbook of Clay Science,* Elsevier Ltd: **1**, p. 115-140.

Chamley, H. 1989. *Clay Sedimentology*. Springer-Verlag. Berlin.

Christidis, G. E. 2009. Application of Electon Microscopy to the study of smectites and zeolites. *Revista de la sociedad Espanola de mineralogia* p. 9-10.

Deocampo, D.M. 2004. Authigenic clays in East Africa: Regional trends and paleolimnology at the PlioPleistocene boundary, Olduvai Gorge, Tanzania. *Journal of Paleolimnology*, **31,** (19).

Deocampo, D.M. 2005. Evaporative evolution of surface waters and the role of aqueous CO_2 in magnesium silicate precipitation: Lake Eyasi and Ngoronogro Crater, northern Tanzania. *South African Journal of Geology,* **108**, p. 493-504.

Deocampo, D.M. 2010. The Geochemistry of Continental Carbonates. Alonso-Zarza and Tanner (Eds.) Carbonates in Continental Settings: Geochemistry, Diagenesis, and Applications, *Developments in Sedimentology* **62,** p. 1-59.

Deocampo, D.M. and Ashley, G.M. 1999. Siliceous islands in a carbonate sea: Modern and Pleistocene records of spring-fed watlands in Ngoronogoro Crater and Oldupai Gorge, Tanzania. *Journal of Sedimentary Reasearch*, **69,** p. 974-97.

Deocampo, D.M., Cuadros, J., Wing-Dudek, T., Olives, J., and Amouric, M. 2009. Saline lake diagenesis as revealed by coupled mineralogy and geochemistry of multiple ultrafine clay phases: Pliocene Olduvai Gorge, Tanzania. *American Journal of Science*. **309**, doi: 10.2475/09.2009.03.

Dixon, J.B. and Weed (ed.), S.B. 1989. Mineral in Soil Environments. *Soil Science Society of America, Inc. (2nd)*

Galan, E. 2006. Genesis of Clay Minerals. *Handbook of Clay Science,* Elsevier Ltd: **1**, p. 1129-1162.

Garrels, R.M. and Mackenzie, F.T. 1967. Origin of the chemical composition of springs and lakes. Equilibrium concepts in natural water systems, *American Chemical Society Advances in Chemistry Series,* **67,** p. 222-242.

Golden, D.C., Dixon, J.B., Shadfan, H. and Kippenberger, L.A. 1985. Palygorskite and sepiolite alteration to smectite under alkaline conditions. *Clays and Clay Minerals* 33, p. 44-50.

Hardie, L.A. and Eugster, H.P. 1970. The evolution of closed-basin brines. *Special Publication of the Mineralogical Society of America,* **3.** p. 273-290.

Hast, N. 1956. A reaction between silica and some magnesium compounds at room temperature and at +37°C. *Arkiv for Kemi,* 9 p. 343 – 360.

Hathaway, J.C. and Sachs, P.L. 1965. Sepiolite and clinoptilolite from the mid-Atlantic Ridge. *Amer. Mineral.,* **50**. P.852 – 867.

Hay, R.L., Hughes, R.E., Kyser, T.K., Glass, H.D., and Liu, J. 1995. Magnesium-Rich Clays of the Meerschaum Mines in the Amboseli Basin, Tanzania and Kenya. *Clays and Clay Minerals,* **12** (4). p. 455 – 466.

Hay, R.L. and Stoessell, R.K. 1984. Sepiolite in the Amboseli Basin of Kenya: A new interpretation. *Developments in Sedimentology*, vol. 37, p. 125-136.

International Center for Diffraction Data (ICDD). How to Analyze Minerals – Fundamentals. Web. March 2014. http://www.icdd.com/resources/tutorials/pdf/HowtoAnalyzeMineral Fundamentals.pdf

Jenkins, R. and Snyder, R.L. 1996. Introduction to X-Ray Powder Diffractometry. *Wiley-Interscience Publisher.*

Johnson, T.C. 1996. Sedimentary processes and signals of past climate change in the large lakes of the East African Rift Valley. C. Johnson and E.O. Odada (Eds), The Limnology, Climatology and Paleoclimatology of the East African Lakes. *Gordon and Breach Science Publishers, Amsterdam, The Neterlands*. p. 367-412.

Jones, B.F. 1986. Clay mineral diagenesis in lacustrine sediments. *Mumpton (Ed.), Studies in Diagenesis*, U.S. Geological Survey Bulletin 1578, p. 291-300.

Jones, B.F. and Deocampo, D.M. 2003. Geochemistry of Saline Lakes. 393-424. *Surface and Ground Water, Weathering, and Soils* (J.I. Drever, editor), Treatise on Geochemistry, **5**.

Jones, B.F., Eugster, H.P. and Rettig, S.L. 1977. Hydrochemistry of the Lake Magadi basin, Kenya. *Geochimica et Cosmochimica Acta*, **41,** p. 53-72.

Keller, W.D. 1963. Diagenesis in Clay Minerals-A Review. *Clays and Clay Minerals*.

Kester, D.R., Duedall, I.W., Connors, D.N. and Pytkowicz, R.M. 1967. Preparation of Artificial Seawater. *Limnology and Oceanography,* **12**. p. 176 –179.

Larsen, D. 2008. Revisiting silicate authigenesisi in the Pliocene-Pleistocene Lake Tecopa beds, southeastern California: Depositional and hydrological controls. *Geosphere,* **4,** p. 612 – 639.

LaTour, T. E. 1989. Analysis of rocks using X-ray fluorescence spectrometry. *Rigaku Journal,* **6.** p. 3-9.

Mizutani, T., Fukushima, Y., Okada, A., and Kamigaito, O. 1991. Hydrothermal Synthesis of Sepiolite. *Clay Minerals,* **26** (3), p. 441 – 445.

Moore, D.M. and Reynolds, R.C. Jr. 1997. *X-Ray Diffraction and the Identification and Analysis of Clay Minerals.* Oxford University Press, Inc: New York.

Murray, H.H. 2007. Applied Clay Mineralogy: Occurrences, Processing and Application of Kaolins, Bentonites, Palygorskite-sepiolite, and common clays. *Developments in Clay Science* Elsevier Ltd, **2**,

Nagy, B. and Bradley, W.F. 1955 The structural scheme of sepiolite. *Amer. Mineral.,* **40**. P.885 – 892.

Otsuka, R., Sakamoto, T., and Hara, Y. 1974. Phase transformation of sepiolite under hydrother mal conditions. *Journal of the Clay Science Society of Japan*, 14, p. 8-19.

Schoonheydt, R.A. and Johnston, C.T. 2006. Surface and Interface Chemistry of Clay Minerals. *Handbook of Clay Science.* Elsevier Ltd: **1**, p. 87-114.

Schultz, L.G. 1960. Quantitative X-ray Determinations for Some Aluminous Minerals in Rocks. *Clays Clay Minerals.* **7**, p. 216 – 224.

Segal, L., Creely, J.J., Martin, A.E., and Conrad, C.M. 1959. An empirical method for estimating the degree of crystallinity of native cellulose using the X-ray diffractometer. *Text. Res. J.* 29 **(10)**, p. 786 – 794.

Siffert, B. and Wey, R. 1962. Syntheses d'une sepiolite a temperature ordinaire. *Comptes Rendus del'Academie des Sciences*, 254, p. 1460 – 1464.

Sposito, G. and Prost, R. 1982. Structure of water absorbed on smectite. *Chemical Reviews* **82**. P. 553-573.

Wollast, R., Mackenzie, F.T., and Bricker, O.P. 1968. Experimental Precipitation and Genesis of Sepiolite at Earth-Surface Conditions. *The American Mineralogist*, **53**. p. 1645 – 1661.